

Changed Ocean Optical Properties: How Shallower Sunlight Absorption impacts Earth's Surface
Energy Budget

Marilyne Poirier

A Thesis
in
The Department
of
Building, Civil and Environmental Engineering (BCEE)

Presented in Partial Fulfillment of the Requirements
for the Degree of Master of Applied Science (Civil Engineering) at
Concordia University
Montréal, Québec, Canada

April 2021

© Marilyne Poirier, 2021

CONCORDIA UNIVERSITY
School of Graduate Studies

This is to certify that the thesis prepared

By: Marilyne Poirier
Entitled: Changed Ocean Optical Properties: How Shallower Sunlight
Absorption impacts Earth's Surface Energy Budget.

and submitted in partial fulfillment of the requirements for the degree of

Master of Applied Science (Thesis: Civil Engineering)

complies with the regulations of the University and meets the accepted standards with respect to originality and quality.

Signed by the final Examining Committee:

_____	Chair
<i>Dr. Ali Nazemi</i>	
_____	Examiner
<i>Dr. Ali Nazemi</i>	
_____	Examiner
<i>Dr. Zhi Chen</i>	
_____	Supervisor
<i>Dr. Catherine Mulligan</i>	

Approved by _____

Graduate Program Director: Dr. Michelle Nokken

_____ 2021

Dean of Faculty: Dr. Mourad Debbabi

Abstract

Title: Changed Ocean Optical Properties: How Shallower Sunlight Absorption impacts Earth's Surface Energy Budget.

Marilyne Poirier

This study investigates the variations in the last decades of underwater sunlight attenuation coefficient (K_d) and its forcing (W/m^2) on the Earth's surface heat budget. It first compares the trends of essential climate variables K_d and sea surface temperature (SST) to gauge their connection. To estimate an equivalent global forcing, it also finds the variation of radiant heating rate (RHR) profiles under the ocean surface. The trends over a different period (14 to 30 years) for K_d , SST and diurnal SST (DSST) were extracted using the statistical Seasonal Mann-Kendal test, from remote sensing datasets available respectively on ESA OC-CCI, NOAA and REMSS public FTP servers. The results were geographically compared on $360^\circ \times 180^\circ$ gridded maps. They were used to estimate global linear regressions of their correlation coefficients. A positive correlation of 0.38 between K_d and SST was found. This result highlights the relevance to investigate the weight of the fate of irradiance decay on the surface heat budget. Using results of K_d trends over the 18-year period, changed incoming solar radiation (I_0) decay in the upper 50 meters, and associated changed RHR profiles, it was possible to map the critical depth (Z_{crit}) at which the (1998) and (2017) RHR curves crossed path. A slightly better negative correlation of -0.42 was found between SST and Z_{crit} . The latter was used to calculate and map the theoretical forcing on the air-sea interface attributed to ocean color changes. Averaged over the Earth's surface, the forcing is $0.33 W/m^2$. This order of magnitude compares to the $3.1 W/m^2$ attributed to greenhouse gases (GHG) forcing. It suggests that the optically responsive aquatic components accumulated into the oceans may significantly drive the surface energy transfer by retaining the solar irradiance closer to the surface. It is recommended to further the study by including K_d in an OAGCM to account for the feedback of the four main fluxes (shortwave, longwave, latent, and sensible heat) composing the budget. The weighting of the forcing attributed to K_d in the budget will improve the significance of the result. Further investigation toward the management of Shortwave (SW), the black carbon (BC) and the ocean color are also recommended. Solutions against anthropogenic warming are proposed, such as the mixing enhancement of stratified waters.

Acknowledgments

This research was conducted thanks to Concordia Institute for Water, Energy, and Sustainable Systems under director Dr. Catherine Mulligan. She allowed the time and space I needed for such a project and trusted my autonomy, for which I am very thankful. Financially supported and encouraged by the NSERC-CREATE program to study abroad, I fostered relationships with external researchers in the University of Melbourne. They not only helped me navigate through the fuzzy environment and literal waves of Australia, but mostly impacted the methodology of the research. I owe a lot of gratitude toward Professor Alexander Babanin who most generously welcomed me and whose work inspired me. Back home, I had the chance to get introduced to the Thèsez-vous community in which I developed an efficient working ethics. I must acknowledge my two fellow researchers extraordinaire Mathilde Bourgeois and Jeanne Joaquim without whom I would have missed the power of friendship, psychological and emotional support in the workplace. My best friends Veronique Martin and Marilou Caron for their indefectible love, and finally Francois Poirier ing., my father who ultimately conceptualized the whole premise with me.

Table of Contents

List of Figures	viii
List of Tables	x
List of Abbreviations	xi
CHAPTER 1 Introduction.....	1
CHAPTER 2 Literature Review	4
Theoretical Framework	4
Global Circulation Model.....	4
Radiative Forcing	5
Earth’s Global Energy Budget Closure	6
Ocean Heat Content.....	7
Sea Surface Temperature.....	8
Gaps and Breakthroughs in literature.....	9
Instruments, sampling, and accuracy.....	9
Two Examples: Water Vapor (1) and Methane (2)	13
Coupling	14
Reanalysis.....	15
Closure constraint	16
Sub-grid drivers	18
Outcomes	19
Upper Layer Heat Distribution.....	22
Mixing	22
Barrier Layer / Stratification.....	23
DSST, the Diurnal Signal of Sea Surface Temperature	24
Light Absorption and Transmission	27
K_{d490} : The Solar Beam Attenuation Coefficient for Downwelling Irradiance (m^{-1}) ..	28
Pertinence of Depth (Z_{crit}) for the Heat Budget.....	30
Kd Parametrization in recent studies	32

Thesis Question	34
Hypothesis: Anthropogenically driven K_d significantly changes the ocean surface layers' heating rate profile, forcing the air-sea heat fluxes.	34
Contribution.....	34
CHAPTER 3 Methodology.....	36
Criteria for dataset selection.....	37
SST	37
DSST	37
K_d	38
I_0	39
Trend extraction procedure	40
Correlation Coefficient.....	43
Forcing on Air-Sea Heat Flux	43
CHAPTER 4 Results.....	47
SST Trend	47
DSST Trend.....	48
K_d 490 Trend	49
Results Summary.....	50
Correlation.....	53
CHAPTER 5 Discussion.....	54
Anthropogenic K_d trend	54
Black Carbon	56
Radiant Heating Rates (RHR).....	59
Correlation	59
Offsets.....	59
Relationship through timeseries	60
RHR Shifts at depth Z_{crit}	65
Forcing	68

Contribution to the Closure Problem.....	69
DSST trend and the thesis question.....	71
Daytime cold bias	72
Link between DSST, wave height and winds.....	73
Limitation and recommendations.....	76
Data Sampling	76
Data Treatment	77
Data Parametrization	78
Methodology.....	79
Mitigations and Applications	80
Reach back an equilibrium through cold water flow.....	80
CHAPTER 6 Conclusions.....	81
References.....	83

List of Figures

FIGURE 1 - GLOBAL RADIATIVE (SWR, LWR) AND TURBULENT (LATENT AND SENSIBLE) ENERGY BUDGET, ASSOCIATED WITH NATURAL AND ANTHROPOGENIC DRIVERS OF CLIMATE CHANGE. (STOCKER ET AL. 2013).....	1
FIGURE 2 - THE TOTAL ANTHROPOGENIC RADIATIVE FORCING EVALUATED AT 2.29 Wm^{-2} AS OF 2011. TODAY'S VALUE HAS INCREASED, REACHING 3.1 W/m^2 (AS OF 2019). (STOCKER ET AL. 2013)	6
FIGURE 3 - GLOBAL HEAT CONTENT (0-2000 METERS) LAYER HAS AN INCREASING TREND ("GLOBAL OCEAN HEAT AND SALT CONTENT" NOAA 2019).....	8
FIGURE 4 – WARMING (COOLING) TREND OF SEA SURFACE TEMPERATURE FROM 1985-2009. AVHRR PATHFINDER VERSION 5.2 L3-COLLATED (L3C) SEA SURFACE TEMPERATURE. [GHRSSST] NOTE THE OMISSION OF COASTAL REGIONS. THE COARSE-LIKE VISUALISATION MAKES EASY THE DETECTION OF GLOBAL AND ZONAL TRENDS.....	9
FIGURE 5 - NOMENCLATURE FOR DIFFERENT SST MEASUREMENTS. DIURNAL SIGNAL IS PRESENT IN UPPER MILOMETERS BUT ARE NOT CONSIDERED IN MODELS GHRSSST. REFERENCE?	11
FIGURE 6 - CHART OF ACCURACY NEEDS FOR THE DETECTION OF CHANGES IN DIFFERENT CLIMATIC APPLICATIONS [W/m^2]. THE CHART ALSO INDICATES THE SPATIAL AND TEMPORAL PRECISION EXPECTED TO REACH THE PRESCRIBED ACCURACY (YU ET AL. 2013).	12
FIGURE 7 - NET SURFACE HEAT FLUXES IMBALANCE FOR DIFFERENT PRODUCTS OVER THE 17 YEARS [1993-2009] (ORA-IP) (BALMASEDA ET AL. 2015)	16
FIGURE 8 - NET ENERGY EXCHANGE FROM THE ATMOSPHERE TO THE SURFACE AFTER OBJECTIVELY INTRODUCING ALL RELEVANT CONTINENTAL-SCALE ENERGY AND WATER CYCLE CONSTRAINTS (L'ÉCUYER ET AL. 2015B).....	18
FIGURE 9 - CONSENSUS FOR GLOBAL ANNUAL MEAN ENERGY BALANCE PARTITIONING OF FOUR MAJOR REANALYSIS PRODUCTS USING CLOSURE CONSTRAINT METHODS (FLUXES IN W/m^2). NET IMBALANCE ESTIMATES RANGE FROM 0.5-0.9 W/m^2 (WILD ET AL. 2017).	20
FIGURE 10 - SCHEMATIC REPRESENTATION OF DSST INTO THE MIXED LAYER. ILLUSTRATION BY ERIC S. TAYLOR, WHOI, AS CITED IN (BOGDANOFF ET AL. 2017)	25
FIGURE 11 - ELECTRO MAGNETIC ENERGY DISTRIBUTION OF A BLACKBODY, MOSTLY IN THE VISIBLE RANGE. LOG SCALE. IMAGE COURTESY OF THE COMET PROGRAM AND THE HIGH-ALTITUDE OBSERVATORY AT NCAR.	27
FIGURE 12 - CASE 1 AND CASE 2 WATERS RELATIVELY ATTRIBUTED TO TRIPARTITE DIAGRAM OF SELECTED CONSTITUENTS' CONTRIBUTION TO THE TOTAL ATTENUATION (SATHYENDRANATH ET AL. 2017).....	32
FIGURE 13- 3D MAPPED MEAN INCOMING IRRADIANCE I_0 [W/m^2] ON THE EARTH SURFACE (NASA-GEWEX SURFACE RADIATION BUDGET (SRB), RELEASE 3.0 DATASET).....	39
FIGURE 14 - EXAMPLE OF TREND CALCULATION FOR ONE BIN. EACH INDIVIDUAL PIXEL OF THE MAPPED INPUT HAS A RESULTING RED SLOPE, DETERMINED FROM ABOVE ALGORITHM. THE FINAL RESULT IS A MAP OF EACH CALCULATED TREND (SLOPE). THE RED CIRCLE HIGHLIGHTS AN EXAMPLE OF A BIAS IN THE K_b INPUT DATASET FOLLOWING THE 2016 SATELLITE MISSION SHIFT, WHICH IS DISCUSSED FURTHER IN LIMITS.	42
FIGURE 15 - SST TREND [% / YR] FROM 1987 TO 2017.....	47

FIGURE 16 - DSST TREND [% / YR] FROM 2002 TO 2011	48
FIGURE 17 - ATTENUATION COEFFICIENT K_D TREND FROM 1998 TO 2016.....	49
FIGURE 18 – UPPER PANEL: IRRADIANCE DECAY PROFILES I_1 (BLUE, 1998 AVERAGE) AND I_2 (RED, 2017 AVERAGE) ALONG THE DEPTH Z , FOR AN AVERAGE INCOMING IRRADIANCE (I_0) AND AVERAGED ATTENUATION COEFFICIENTS K_{D1} AND K_{D2} . LOWER PANEL: RADIANT HEATING RATE PROFILES RHR_1 (BLUE) AND RHR_2 ALONG THE DEPTH Z FOR I_1 AND I_2 , AND K_{D1} AND K_{D2} RESPECTIVELY. THE OVERALL FORCING IS THE AREA (ORANGE) DELIMITED BY RHR_1 , RHR_2 , $Z=0$ AND $Z=Z_{CRIT}$ AND IS ALSO EQUIVALENT TO UPPER PANEL I_1 AND I_2 DIFFERENCE.	51
FIGURE 19 - CRITICAL DEPTH Z_{CRIT} ASSOCIATED WITH THE RHR_1 AND RHR_2 CURVES CROSSING.	52
FIGURE 20 - YEARLY FORCING (W/M^2) ON AIR-SEA HEAT FLUX ASSOCIATED WITH K_D TREND AND INCOMING IRRADIANCE I_0	52
FIGURE 21 - COMPARISON OF LIGHT PENETRATION THROUGH OPEN VS COASTAL WATERS IN VISIBLE WAVEBAND. IMAGE COURTESY: KYLE CAROTHERS, NOAA-OE	55
FIGURE 22 - SCHEMATIC OVERVIEW OF BC SOURCES AND PROCESSES. SHOWS THE COMMUNITY EFFORTS TO CONSIDER ITS EFFECT ON RADIATIVE FORCING ONCE IN ATMOSPHERE AND DEPOSITED ON SNOW. DOES NOT SHOW THE ROLE BC HAS ONCE DEPOSITED INTO WATER (BOND ET AL. 2013).	57
FIGURE 23 - DIFFERENCES BETWEEN DIFFERENT CLIMATE MODELS WHEN ASSESSING THE SURFACE TEMPERATURE CHANGES DUE TO BC FORCING. NOTE THAT THE FORCING OCCURS MOSTLY IN HIGHER LATITUDES (BOND ET AL. 2013).	57
FIGURE 24 – A) NOAA MONTHLY ENSO INDEX TIME SERIES PROGRESSION IS SIMILAR TO CHL-A B) OC-CCI CHLOROPHYLL CONCENTRATION TIME SERIES FOR THE SAME PERIOD, INDICATING A POSITIVE TREND (GROOM ET AL. 2019).....	61
FIGURE 25 - COMPARISON OF THE THREE SIMULATIONS RUNS FOR SST 2015 TIMESERIES IN THE BAY OF BENGAL REGION (MALICK ET AL. 2019).	62
FIGURE 26 - DIFFERENCE BETWEEN Kd_{490} AND THE CONSTANT VALUE OF 23 M, USED IN THE CONTROL RUN (CR), FOR THE YEAR 2015 IN THE BAY OF BENGAL REGION. NEGATIVE DIFFERENCES INDICATE SHALLOWER PENETRATION OF SHORTWAVE RADIATION IN THE ER WHILE THE PENETRATION IS DEEPER IF DIFFERENCES ARE POSITIVE (MALICK ET AL. 2019).....	63
FIGURE 27 – SDD AND SST GLOBAL AVERAGED TIME SERIES. THEIR OVERALL REGRESSION IS EVOLVING IN THE SAME DIRECTION (HE ET AL. 2017).	64
FIGURE 28 – (A) SDD TREND, (B) CHLOROPHYLL TREND AND (C) SST TREND, FROM 1998 TO 2010, BY BIOGEOGRAPHIC PROVINCE (HE ET AL. 2017)	65
FIGURE 29 - DISTRIBUTION OF A THEORICAL SDD ANNUAL MEAN (HE ET AL. 2017). VIRTUALLY THE SAME RESULT WHEN COMPARED TO OUR MAPPED Z_{CRIT} OF FIGURE 19.	66
FIGURE 30 - DIFFERENCE OF RHR AND TEMPERATURE FOR THE INCLUSION OF COLOR DETRITAL MATTER INTO MODEL RUNS A) RHR FOR Z OF 0 TO 10 M B) RHR FOR Z OF 20 TO 30 M AND C), D) TEMPERATURE DIFFERENCES FOR UPPER AND LOWER LAYERS (KIM ET AL. 2016).	67
FIGURE 31 - NET FLUX DIFFERENCE WHEN CONSIDERING THE SST DIURNAL SIGNAL FOR 10-YR. CONTOUR LINE IS AT $0 W/M^2$. “THE TOTAL GLOBAL-AVERAGE DIFFERENCE IS $1.21 W M^{-2}$. “ (CLAYSON AND BOGDANOFF 2013).....	68
FIGURE 32 - EVOLUTION OF THE FLUXES COMPOSING THE EARTH HEAT BUDGET OVER TIME (PIERCE ETAL. 2006).	70

FIGURE 33 – DIFFERENCE BETWEEN DSST AVERAGE DATASET BEFORE (LEFT, 2002 TO 2011) AND AFTER (RIGHT, 2012 TO 2016) THE AMSRE MISSION SHIFT TO AMSR2.	72
FIGURE 34 - COMPARISON ON A NEGATIVE SCALE ONLY BETWEEN THE TWO AVERAGED DSST MISSIONS AMSRE (2002 TO 2011) AND AMSR2 (2012 TO 2016)	73
FIGURE 35 – UPPER PANEL: MAPPED TREND OF 90TH PERCENTILE WIND SPEED AND WAVE HEIGHT FROM 1991 TO 2008 (YOUNG ET AL. 2011A). LOWER PANEL: MAPPED RESULTING TREND OF 90 TH PERCENTILE DSST FROM 2002 TO 2011.	74

List of Tables

TABLE 1 - OBSERVED COMPONENTS OF THE GLOBALLY AND ANNUALLY AVERAGED ENERGY BUDGET AND THEIR UNCERTAINTIES BEFORE AND AFTER OPTIMIZATION (Wm^{-2}). LAST COLUMN SHOWS READJUSTMENT OF FLUXES SATISFYING THE CONSTRAINED SURFACE NET FLUX TO MATCH TOA FORCING (L'ECUYER ET AL. 2015b).....	17
TABLE 2 - DRIVERS OF THE UPPER HEAT DISTRIBUTION (MALICK ET AL.2019).....	22
TABLE 3 - SURFACE HEAT FLUXES' CHANGE ASSOCIATED WITH AN SST INCREASE OF 1 °C SIMULATING A DW. (TOGA COARE IOP) (WEBSTER ET AL. 1997)	26
TABLE 4 - SUMMARY OF INPUT DATASET	36
TABLE 5 - SUMMARY OF GLOBAL MEAN VALUES OF TREND FOR THE FIVE MAIN VARIABLES.....	50
TABLE 6 - CORRELATION COEFFICIENTS BETWEEN FIVE 10° X 10° MAP SIZE DATASETS.....	53

List of Abbreviations

Abbreviation	Definition
AOD	Atmospheric Optical Depth
AOP	Apparent Optical Property
BC	Black Carbon
BL	Barrier Layer
CDM	Colored Detrital Material
CDOM	Colored Dissolved Organic Matter
DOM	Dissolved organic Matter
DSST	Diurnal signal of Sea Surface Temperature
DW	Diurnal Warming
ENSO	El-Nino Southern Oscillation
ESA	European Space Agency
GCM	Global Circulation Model
I_0	Surface Downwelling Irradiance
IOP	Inherent Optical Property
IPCC	Intergovernmental Panel on Climate Change
IR	Infra Red spectrum
K_d	Attenuation Coefficient for Downwelling Irradiance
LHQ	Latent Heat Flux
LW	Longwave
MLD	Mixed Layer Depth
NAP	Non-Algal Particle
NWP	Numerical Weather Prediction
OAGCM	Ocean-Atmosphere Global Circulation Model
OHC	Ocean Heat Content
OI SST	Optimally Interpolated Sea Surface Temperature
ORA	Ocean Re-Analysis
R	Correlation Coefficient
RF	Radiative Forcing
RHR	Radiant Heating Rate
RTE	Radiative Transfer Equation
SDD	Secchi Disk Depth
SHQ	Sensible Heat Flux
SK	Seasonal Mann-Kendall test
SST	Sea Surface Temperature
SW	Shortwave
TOA	Top of Atmosphere

CHAPTER 1 Introduction

The Intergovernmental Panel on Climate Change (IPCC) and the World Climate Research Programme (WCRP) work to predict the impact of anthropogenic emissions on our climate. Their conclusion is strong and unequivocal: oceans and atmosphere are warming, reaching respectively 0.18°C and 1°C above pre-industrial levels (Masson-Delmotte et al. 2018). The budget (Figure 1) is historically very “atmospheric-oriented”. The accurate identification of the many drivers at the surface would yield to sustainable solutions against global warming. The use of climate models for the detection and attribution of ocean warming is recent and very few studies prior 2005 examined in detail the vertical structure of the solar extinction and absorption (Pierce et al. 2006). Yet, three times out of four, the solar radiation that strikes the planet hits water. The contribution of the oceans’ surface to the global warming is assessed here.

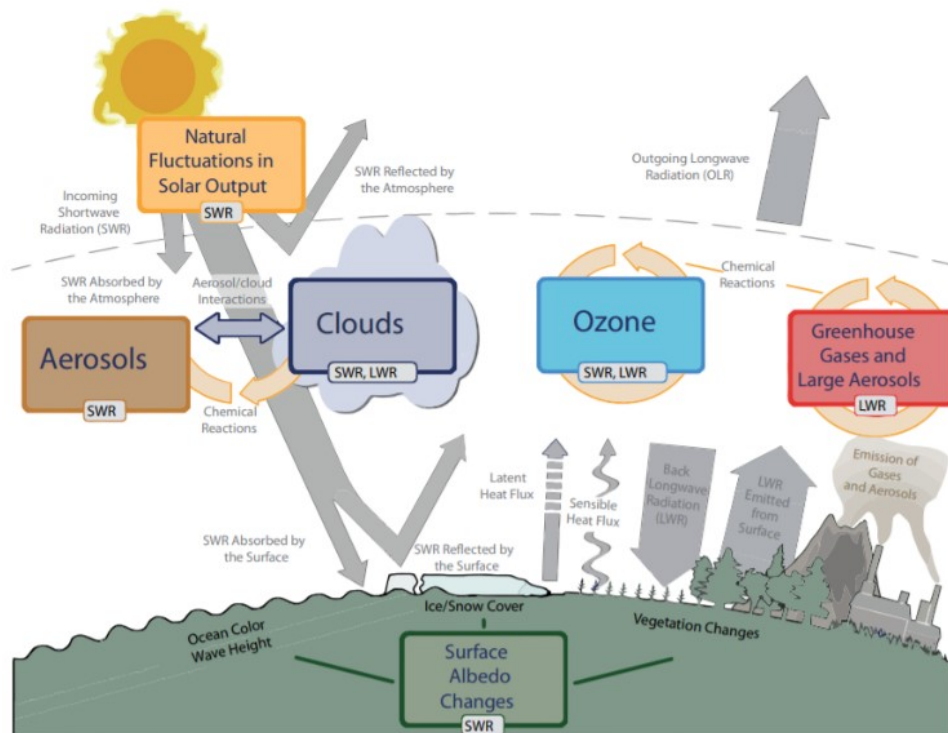


Figure 1 - Global radiative (SWR, LWR) and turbulent (Latent and sensible) energy budget, associated with natural and anthropogenic drivers of climate change. (Stocker et al. 2013)

Large scale circulation patterns driving both weather and climate are governed by energy imbalances between the atmosphere, ocean, and cryosphere. Well known biases of the energy partitioning are being documented (L'Ecuyer et al. 2015b). A proper consensus between models over the distribution of the 4 main heat fluxes as described in Figure 1 is hard to reach. Despite high-quality bulk parameter measurements, there is a frustrating divide between our understanding of the forces governing the surface fluxes and our failure to accurately quantify them. The gap is consensually termed as the *Closure Problem* of the ocean heat budget. The *Closure Problem* consists of a recurrent discrepancies between the global mean net heat flux existing products, ranging from 20 to 40 Wm^{-2} depending on the study (Josey al 1999). In other words, radiation fluxes (shortwave visible light from the sun and infrared back radiation from the GHG) would exceed turbulent fluxes (latent and sensible heat leaving the surface) by as much as 40 W/m^2 on a yearly and spatially average, disproportionately unbalancing the budget. That “embarrassing situation” (Godfrey 2006) and “enormous discrepancy” (Ohmura 2014) must be explained. A new look on this issue is undertaken here, particularly regarding the contribution of the solar extinction sub-grid processes on the imbalance.

In the hope of tackling the *Closure Problem*, this study reports the variability of visible light absorption modes in upper layers and addresses the different heat fluxes caused by the increasing pollution. The exact imbalance at the air-sea interface requires a level of accuracy not yet available from any direct measurements. The overall bias caused by the models' omission of the ocean color sub-grid driver will be estimated using trends. The theoretical forcing (in W/m^2) it produces on the surface will be estimated independently of the 4 main fluxes composing the heat budget. However, its implementation into a proper model would be necessary in a future study to acknowledge their interdependency.

The objectives are: 1) to qualify and quantify the dependency between sea surface temperature (SST) and its color (K_d) via analysis of the correlation between their respective trends, 2) to identify on a map the zones where irradiance (I_0) decay and radiant heating rate (RHR) profiles in oceans' upper layers have the most impact when changed, and 3) to quantify the associated forcing on the air-sea interface. Another objective is 4) to raise awareness on the

necessity to implement an appropriate shortwave (SW) attenuation coefficient (K_d) sub-grid into the models.

The Chapter 2 first reviews how the current climate simulations and surface energy budget are generated through General Circulation Models (GCM). The flaws and breakthroughs associated with their reanalysis will indicate where and what to look for in our climate datasets. The review of ocean layers' heat distribution will revive notions of physical oceanography to embed in the reader's mind the recurrent use of the fate of the incoming visible solar radiation (SW) under the surface. Notions of beam solar attenuation with depth will allow to decorticate the thesis question, explain the variables at stake and perform appropriate calculations. The methodology for the data sampling, statistical trend extraction and correlation will be explained in Chapter 3, as well as steps to calculate the theoretical forcing. The Chapter 4 will examine the results in the form of mapped trends, table of correlation and mapped forcing. An important section of the discussion in Chapter 5 will be dedicated to the comparison of the results with those of similar and complementary studies. The natural and anthropogenic causes of changed ocean color are discussed. The results are interpreted in relation to the *Closure Problem*, considering encountered limits and suggestions to minimize their effect. The final recommendations for future works are made in the conclusion of the Chapter 6.

Theoretical Framework

Global Circulation Model

The seasonal to interannual oscillation of the climate are typically simulated in General Circulation Models (GCMs), which are three-dimensional equations of fluid movements and radiative transfer, integrated over space and time (Stocker et al. 2013). GCMs are solved using the COARE bulk flux algorithm, mostly integrating satellite remote sensing datasets and Numerical Weather Prediction (NWP) outputs to generate predictions (Jin and Weller 2008). They involve surface pressure, wind speed, water temperature and salinity, radiation fluxes, cloud cover, wave height, etc. (Soloviev 2013). These meteorological variables have been documented for several decades¹ with various quality standards. Today's GCMs products² are typically mapped on 25 to 100 km grids.

The Fundamental Law of Energy Conservation applies for Earth's surface heat balance and is the foundation of this thesis. At the air-sea interface (Figure 1), the net heat flux (Q_{net}) is the sum of radiative shortwave (SW), longwave (LW) and turbulent latent (LHQ), and sensible (SHQ) fluxes ((1)(2)(3)). SW is commonly recognized as the visible light emitted and received from the sun, while LW is the Infrared energy that is re-emitted by the Earth's components once they were heated by absorbed SW. The incoming SW radiation is a direct top of atmosphere (TOA) measure (dashed line of Figure 1). The outgoing LW radiation is a function of surface temperature and water emissivity following the Stefan-Boltzmann Law (Bergman et al. 2011). The turbulent latent and sensible heat (LHQ and SHQ) manifest respectively through vaporization and conduction between the Earth's surface and the atmosphere. In the climate community, a typical resolution of the modeled energy conservation equation (Jin and Weller 2008) is made using the Monin-Obukhov similarity approach³.

¹(Albrecht, 1940), the first paper on the energy balance at the Earth's surface, as cited in (Foken, 2006). The 150 years of achievements surrounding the thermodynamics research involving earth's budget are reviewed in (Ohmura, 2014).

² (Stocker et al, 2013) valid the bulk formula correctness among coupled models.

³ The Monin-Oboukhov similarity theory was developed for the atmospheric boundary layer but does not properly describe the upper ocean boundary layer. (Bogdanoff et al., 2017),(Soloviev, 2013)

$$SW - LW - LHQ - SHQ = Q_{net} \quad (1)$$

$$LHQ = \rho L_e C_e U (q_s - q_a) = \rho L C U \Delta q \quad (2)$$

$$SHQ = \rho c_p C_h U (T_s - T_a) = C_p C_h U \Delta T \quad (3)$$

With density of air (ρ), latent heat of evaporation (L_e), specific heat capacity of air (C_p), turbulent exchange coefficients for latent heat (C_e), turbulent exchange coefficients for sensible heat (C_h), wind speed (U), sea surface temperature (T_s) near-surface air temperature (T_a), specific humidity (q_a and q_s), the surface meteorological variables (Yu et al. 2007).

Radiative Forcing

At TOA (Top of the Atmosphere, dashed line in Figure 1), remote sensing measurements of SW and LW radiations are consistent among studies. Their determination has been “allowed with unprecedented accuracy” through satellite missions⁴ (Wild et al. 2017); (Loeb et al. 2009). Their space-born passive measurements allow the detection of Q_{net} (the discrepancy between incoming and outgoing energy). Although the net TOA Q_{net} measurement of 6.5 W/m^2 exceeds the expected calculated imbalance value⁵ of 0.85 W/m^2 , good estimates of the calibration uncertainties now allow adequate adjustment within range.

For this imbalance, a strong consensus in the literature blames the buildup of the atmospheric concentration of CO_2 since 1750. the so-called *Radiative Forcing*, estimated at 3.1 W/m^2 relative to pre-industrial era (Butler 2019) (Figure 2), is a direct empirical index of the greenhouse gas (GHG) global abundance. The *Forcing* matches the reduction of the outgoing longwave fluxes, held captive by the GHG (Bergman et al. 2011). The associated surface warming leads to serious investigations regarding other drivers than the GHG (see Figure 2). It reveals the role of sub-grid processes at the surface⁶ (ex: albedo changes, wave heights, ocean color),

⁴ “Direct measurements of TOA fluxes did not begin until the advent of Earth-observing satellites and only became comprehensive and detailed in the 1980s” (Raschke et al., 2012)

⁵ Based on observed ocean heat content data and model simulations

⁶ The history of the atmosphere and ocean’s observation is hovered in (Stocker et al, 2013)

underrepresented as of now in the models. Turbulent fluxes estimated at the surface rely on in-situ measurement and are hard to obtain (Wild et al. 2017).

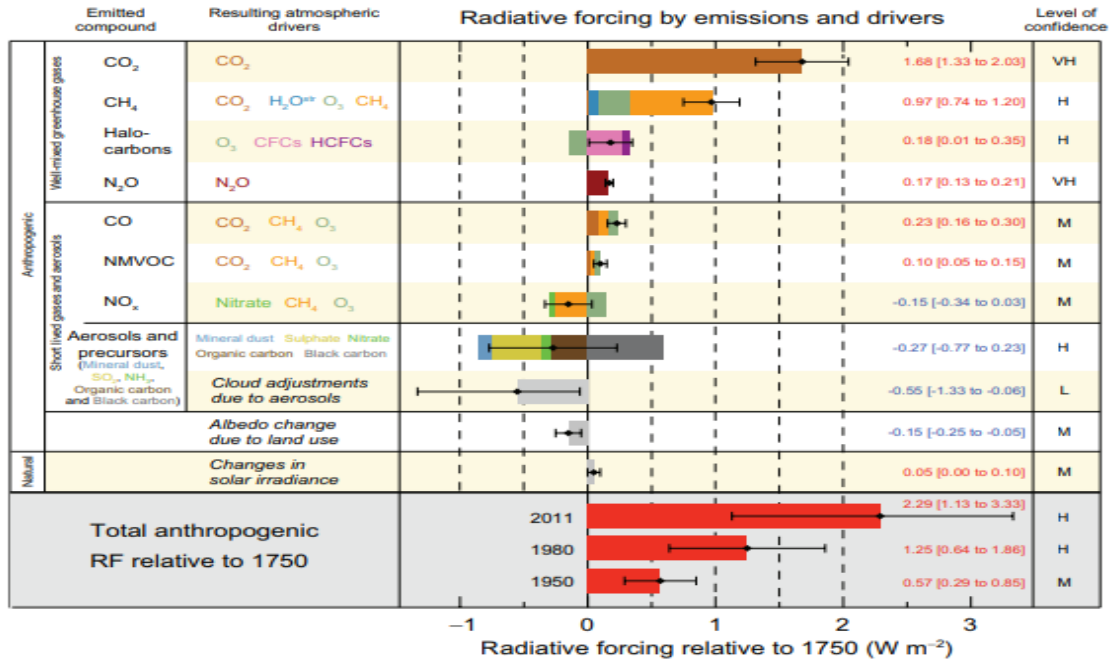


Figure 2 - The total anthropogenic radiative forcing evaluated at 2.29 Wm⁻² as of 2011. Today's value has increased, reaching 3.1 W/m² (as of 2019). (Stocker et al. 2013)

Earth's Global Energy Budget Closure

Surface net flux is expected to match the TOA net flux value to within 0.1 W/m², the heat capacity of the atmosphere being very small (L'Ecuyer et al. 2015). A perfect closure of the heat budget is not expected. However, the magnitude of the imbalance entering the ocean is disproportionate. These serious biases represent about 10% of the incoming solar radiation and are unexpected considering ocean heat content estimates (Trenberth et al. 2014).

Today's vast observational system is not without errors. Meteorological variable acquisition was initially made for NWP under the auspices of the national weather services. The evolution of applications and observing practices for climate data monitoring demands to reprocess

the raw observational records, altering their mean values (Stocker et al. 2013). The idea of measuring turbulent fluxes directly with the Eddy covariance method (Foken 2006) came early, circa 1955, but has not been used until the 1980s. Later in the early 2000, a series of papers led by Josey et al., treating the surface heat budget recognized the *Closure Problem* as a priority (Josey et al. 1999) and established a guideline for the evaluation of air-sea fluxes datasets (Josey and Smith 2006).

Ocean Heat Content

The excess warmth and atmospheric moisture caused by GHG and water vapor enhance the thermal IR re-emission toward the surface. This radiation is absorbed back into the skin layer and transferred into the first meters of water through mixing (L'Ecuyer et al. 2015a). Equation (4) below defines the OHC (Ocean Heat Content⁷), increased by 25×10^{22} Joules as of 2019 (NOAA 2019) (see Figure 3). The associated heating rate between 1971 and 2019 is equivalent to 0.27 W/m^2 applied over the entire earth's surface. The warming rate of the ocean is a function of depth and is non-linear. The present thesis relies on the surface warming signal, which sometimes enhances a thermal stratification of the upper ocean, exacerbates the temperature differentials with the atmosphere and influences air-sea fluxes (Jin and Weller 2008).

$$OHC = \rho C_p \int_0^z (T_c - T_p) dz \quad (4)$$

With climatology temperature (T_c), profile temperature (T_p), depth (z) and volumetric heat capacity of water (ρC_p).

⁷“The OHC is attained from the difference of the measured potential temperature profile and the potential temperature climatology. This difference is integrated over a particular reference depth (for instance, 700 m) and is multiplied by a constant ocean density reference and heat capacity.” (Abraham et al., 2013)

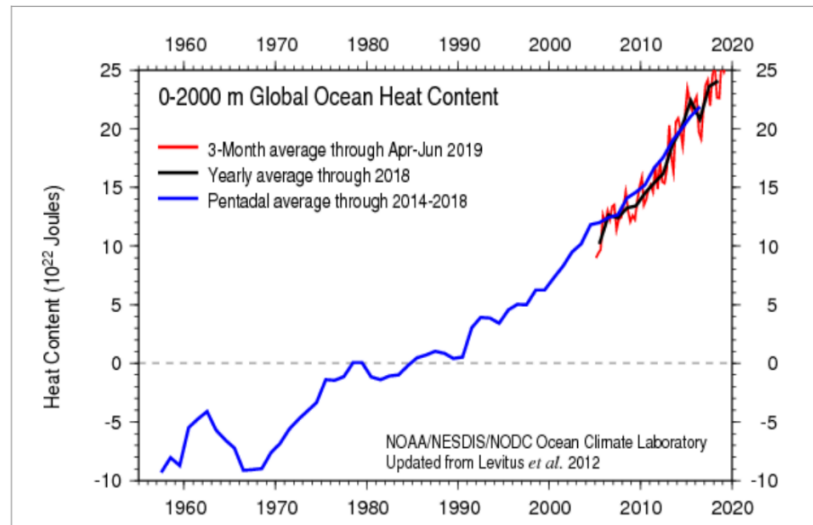


Figure 3 - Global Heat Content (0-2000 meters) layer has an increasing trend (“Global Ocean Heat and Salt Content” NOAA 2019)

Sea Surface Temperature

Multidecadal SST often has a positive trend. The observed warming is concentrated in the northern hemisphere (see Figure 4). Recent studies highlight the role of the SST anomaly on the atmospheric warming. For example, GCM biases are improved by 10-15 % when atmospheric temperature and precipitation responses enhanced by local SST warming are considered (Balaguru et al. 2011). Soloviev (2013) provides insight into the effect of stratified SST gradient model validation by parametrizing the SST across the cool skin. Gentemann and Hilburn (2015) and Zhang et al. (2016) found that inclusion of a diurnal warming signal of SST in models could benefit estimates of surface energy and moisture budget. In their objectively analyzed air-sea heat fluxes for the global ice-free oceans, Yu et al. (2007) suggest an atmospheric response to oceanic *forcing* through the patterns of high/low variances of SST. These are examples of SST variations forcing the overlaying atmosphere.

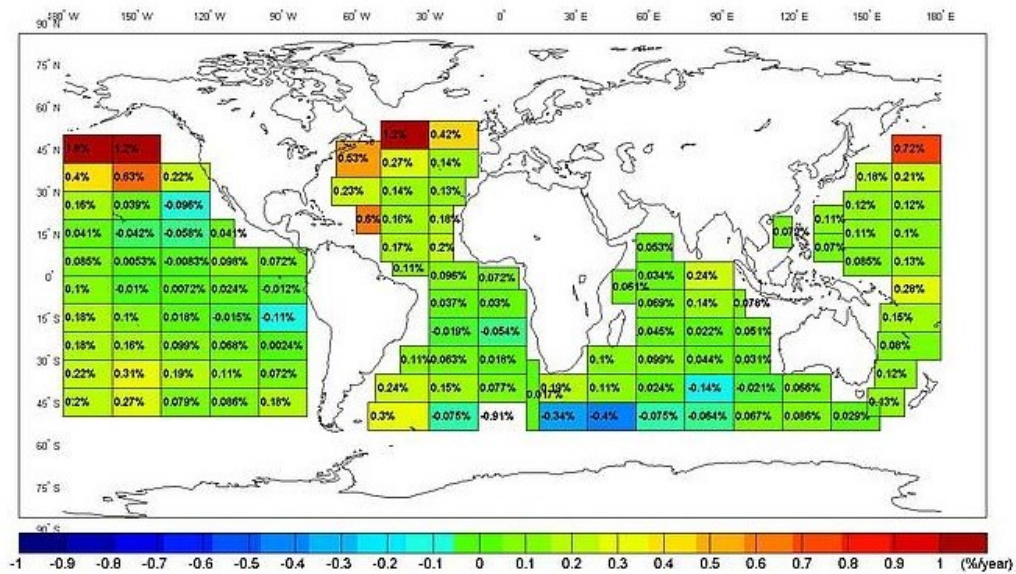


Figure 4 – Warming (cooling) trend of Sea Surface Temperature from 1985-2009. AVHRR Pathfinder Version 5.2 L3-Collated (L3C) sea surface temperature. [GHRSSST]⁸ Note the omission of coastal regions. The coarse-like visualisation makes easy the detection of global and zonal trends.

Gaps and Breakthroughs in literature

This section reveals how structural deficiencies in the observing system inevitably hindered our understanding of physical oceanography.

Instruments, sampling, and accuracy

Although the difficulty in measuring surface temperature has been greatly reduced in space and time with the contribution of remote sensing observation, satellite datasets still rely on in situ confirmation for calibration (Yu et al. 2007). Much of the deep ocean is also still poorly monitored (Abraham et al. 2013). Voluminous southern oceans are not as represented as their volume-less Northern counterparts. Pierce et al. (2006) explore how sampling affects the detection and

⁸ These data were provided by GHRSSST and the US National Oceanographic Data Center. This project was supported in part by a grant from the NOAA Climate Data Record (CDR) Program for satellites.

attribution of OHC. When global climate began to be considered, an outdated agreement was that nothing deserving attention could be found in the upper layers of the ocean (Godfrey 2006). The first models using high-tech probes to recreate the earth's heat budget relied strictly on sparse in-situ datasets (Josey et al. 1999). Also, the near-surface air temperature was almost impossible to retrieve accurately due to disturbance of instruments itself on the environment (Brunke et al. 2011). Fortunately, the increasing number of sampling radiation station now helps to improve bulk flux algorithms locally (Yu et al. 2013); (Wild et al. 2013). However, they remain inhomogeneous in space and time, particularly over the oceans (Palmer 2014). The skin temperature (upper few micrometers) differs from layers below, being sensitive to climate conditions (winds, isolation, precipitation, etc.). The difference can reach 4 to 5 K (Fairall et al., 1996) as cited in (Soloviev 2013). The “real” temperature value is still being approximated using the COARE correction of the bulk temperature measured at 0.5 m (or more) below the surface (“Global Ocean Heat and Salt Content” NOAA 2019).

In the literature, SST is not a standard reading. The “Group for High resolution Sea Surface Temperature” (GHR SST) established a common nomenclature to unify future works, illustrated in Figure 5. Infrared, microwave and in situ sensors reach different “surface” depths respectively (Kawai and Wada 2007). Accounting for those differences improves NWP and climate model performance (Zhang et al. 2020). Kawai and Wada (2007) identified the problem generated by this communication gap as an important error in satellite derived SST.

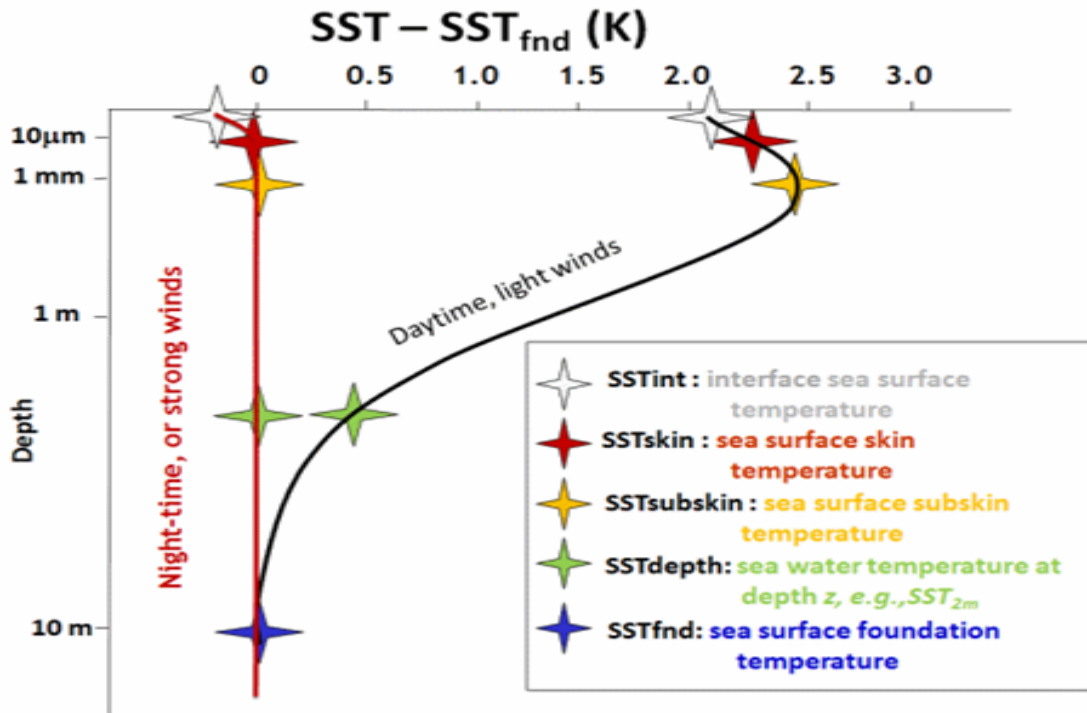


Figure 5 - Nomenclature⁹ for different SST measurements. Diurnal signal is present in upper milometers but are not considered in models GHRSSST. Reference?

In the 2012 WHOI air-sea fluxes workshop, (Yu et al. 2013) recommend to improve the accountability of the underrepresented ocean signals that may hold keys to climate change monitoring. The current level of uncertainty (reaching 30 W/m²) when observing the fluxes governing the rate of change of heat content does not meet its prescribed accuracy requirements (Yu et al. 2013). Figure 6 reveals, for example, how the annual ocean heat flux variability requires a 10 W/m² accuracy, the detection of the *forcing* requires a high accuracy of 0.1 W/m², while physical-biological interaction accuracy needs are acknowledged as unknown.

⁹ SST_{int}: “True” hypothetic temperature at the very interface
 SST_{skin}: Temperature of first micrometers, measured from IR sensors
 SST_{subskin}: Temperature of first millimetre, measured from microwave sensors
 SST_{depth}: Temperature used in bulk formulae, measured with in-situ sensors
 SST_{fnd}: Temperature at the bottom limit of mixed layer, free from diurnal signal.

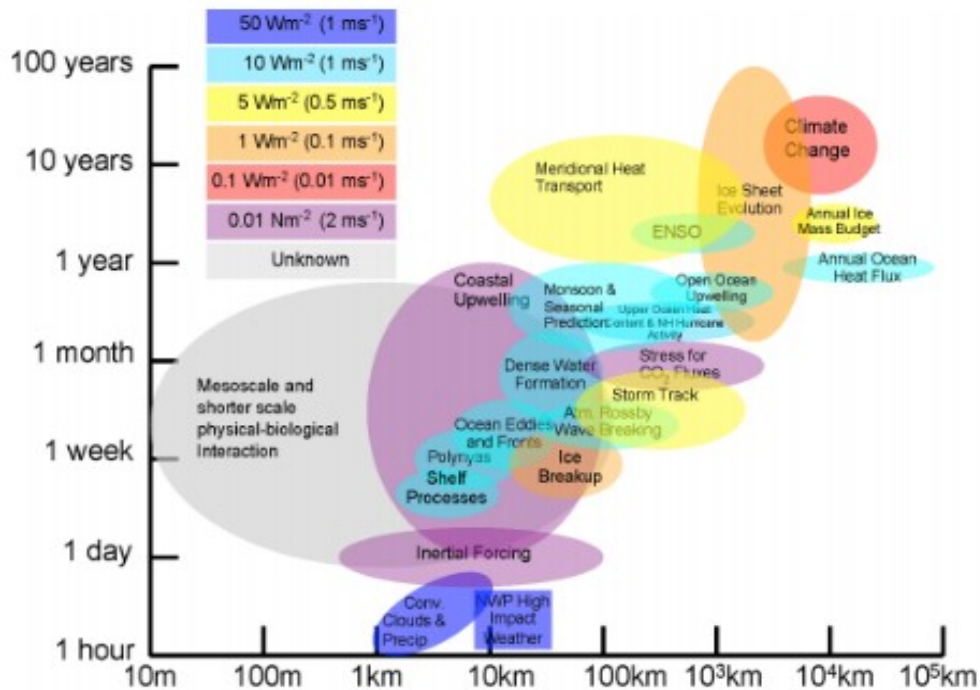


Figure 6 - Chart of accuracy needs for the detection of changes in different climatic applications [W/m^2]. The chart also indicates the spatial and temporal precision expected to reach the prescribed accuracy (Yu et al. 2013).

The needs for the resolution of NWP simulation differ greatly in space and time from those for climate model resolution. The prescribed accuracy for “Annual Ocean Heat Fluxes” estimates is higher than “NWP High Impact Weather” (10 and 50 W/m^2 respectively, as seen in Figure 6). The NWP typical need for a stable gridded SST dataset with *complete* coverage accordingly forces the production of a large-scale interpolation to fill the voids in the grid. These OI “Optimal Interpolation” SST products conveniently use finite elements to fill uncovered areas for a higher resolution (Stocker et al. 2013). They are usually averages of 7 days in situ data taken from ships and buoys at 1 m depth (Clayson and Bogdanoff 2013). This interpolation creates “blended” products, with “smoothed” extreme events, preventing the detection of sub-grid “disturbance” (Clayson and Bogdanoff 2013); (Reynolds and Smith 1994); (Reynolds et al. 2007). This example of corrected SST product is suitable for NWP but becomes problematic for global climatic trend

extraction, because a Reynolds' product¹⁰ is not “a true” daily SST average (Clayson and Bogdanoff 2013). Operational divergence in climatic models hence has emerged through parametrized boundary conditions and background climatology¹¹ choices (Stocker et al. 2013).

The explanation of the *Closure Problem of Earth's heat budget* is important because it clearly flags the lack of agreement regarding the role of oceans on the forcing. Apart from the improvement of its variables, there is room in climate sciences for better physical interpretations (Simionato et al. 2003). Prior to 2002, the ocean's role was surprisingly found as insignificant in influencing the overlaying changing atmosphere (Wills 2016). However, due to the recent available higher resolution satellite measurements, evidence of direct atmospheric response to SST anomalies was discovered. Challenging the granted assumption of interactions between variables sometimes needs re-interpretation of the physics governing them. The next two examples highlight this necessity.

Two Examples: Water Vapor (1) and Methane (2)

- 1- The water vapor in the upper atmosphere was poorly represented for many years in models (Stocker et al. 2013). In the IPCC third Assessment Report (AR3), the atmospheric absorption of radiations by the water vapor was vastly underestimated. It took more than a decade between the acknowledgment of the problem and its proper publication in AR5 (Ohmura 2014). Even in AR4 the absorption rate correction was met with resistance and was not changed. It was very surprising to find that the most important constituent of the atmosphere was still unsolved (Ohmura 2014). The belief that water vapor was not so important was incorrect but strong. Even so that according to personal communication in 1995, “the editor of the Bull. Am. Met. Soc. allegedly insisted that the absorption was unacceptably large and the authors were forced to cut the absorption for the manuscript to be accepted” (Ohmura 2014). This example makes

¹⁰ Reynold's OI SST is a spatially smoothed 7-day average combination of AVHRR, microwave and IR instruments, NWP outputs and in situ buoys observations of SST (<http://oaflex.whoi.edu>)

¹¹ A climate variable averaged over a given period of time to obtain a consistent pattern of its expected value. Example: Reynolds' climatology (Reynolds & Smith, 1998)

us realize how external human bias can lead to incorrect assumptions. Absorption of solar radiation could be seriously underestimated for one or more climatic component, spreading a significant error for many decades. Similarly, the fixed averaged coefficient used in models to characterize the light absorption into the oceans could be a mishandling¹².

- 2- The second example recognizes the omission of shortwave effect in the calculation of methane radiative forcing to be responsible for 15% underestimation of its global value (Collins et al. 2018). This legitimately raises questions about our incomplete knowledge of solar radiation absorption management.

Coupling

The combination of GCM and OHC into Ocean-Atmosphere Global Circulation Models is very recent and likely to evolve. The growing interest for coupled OAGCM could be attributed to the improvement of remote sensing technologies (Soloviev 2013). They were deemed useful only after the 1993 program TOGA COARE (Webster et al. 1997), who were the first instigators of coupling the atmospheric boundary conditions with the ocean's varying components. Before that, the considerable uncertainties conveyed by surface fluxes acquisition hampered the coupling (Wild et al. 2017). The computational costs also traditionally limited the coupling to fixed averaged values, but today's powerful computer allow real-time feedback between both systems. CERA-20C is an example of recent atmosphere–ocean coupled climate reanalysis (Buizza et al. 2018) as cited in (Meucci et al. 2020).

¹² GODAE use 1977 empirical turbidity dataset in models, which most likely increased since then.(Valdivieso et al., 2015)

Reanalysis

Updating adequate boundary conditions in OAGCM is the task performed into reanalysis¹³. They are multi-models' reconstructions, assimilating improved observations or newly available versions of products. For example, L'Ecuyer et al. (2015a) "CONCEPT-HEAT" compared several estimates for the climate models participating in the 4th and the 5th assessments of IPCC. Rather than using modeled states of the atmosphere, they use real-time parametrization of climate variables from NWP as inputs. Thus, they consider "best available estimates of the physical state of the atmosphere" (Wild et al. 2017). Direct observations of nonradiative fluxes are sparse. Reanalyses are therefore considered valuable for their parametrization. This thesis will question the actual climatic inputs' parametrization.

To illustrate the contribution of assimilation¹⁴ methods of SST increments in the upper layers, The Balmaseda et al. (2015) ORA-IP reunites and compares ocean observation products. They identified deficiencies in the observing system from robust inputs in climate monitoring. Figure 7 shows the contradicting net downward energy imbalances from different Ocean Reanalysis products (ORA), on a 17-year span, before and after applying assimilation techniques. Some product net downward heat fluxes reached up to two orders of magnitude higher than the prescribed 0.5 W/m^2 . Balmaseda et al. (2015) inter-comparison of ORAs highlight the role of a parametrization methods which reduces these net imbalances. They provided a mean "ENSEMBLE" product, still positive and one order of magnitude higher than consistent OHC. This approach is an example of improvement of the model inputs.

¹³ WCRP provides a guideline regarding the conduction of associated techniques (Raschke et al., 2012)

¹⁴ Assimilation techniques includes Optimal Interpolation (OI) (Reynolds & Smith, 1994).

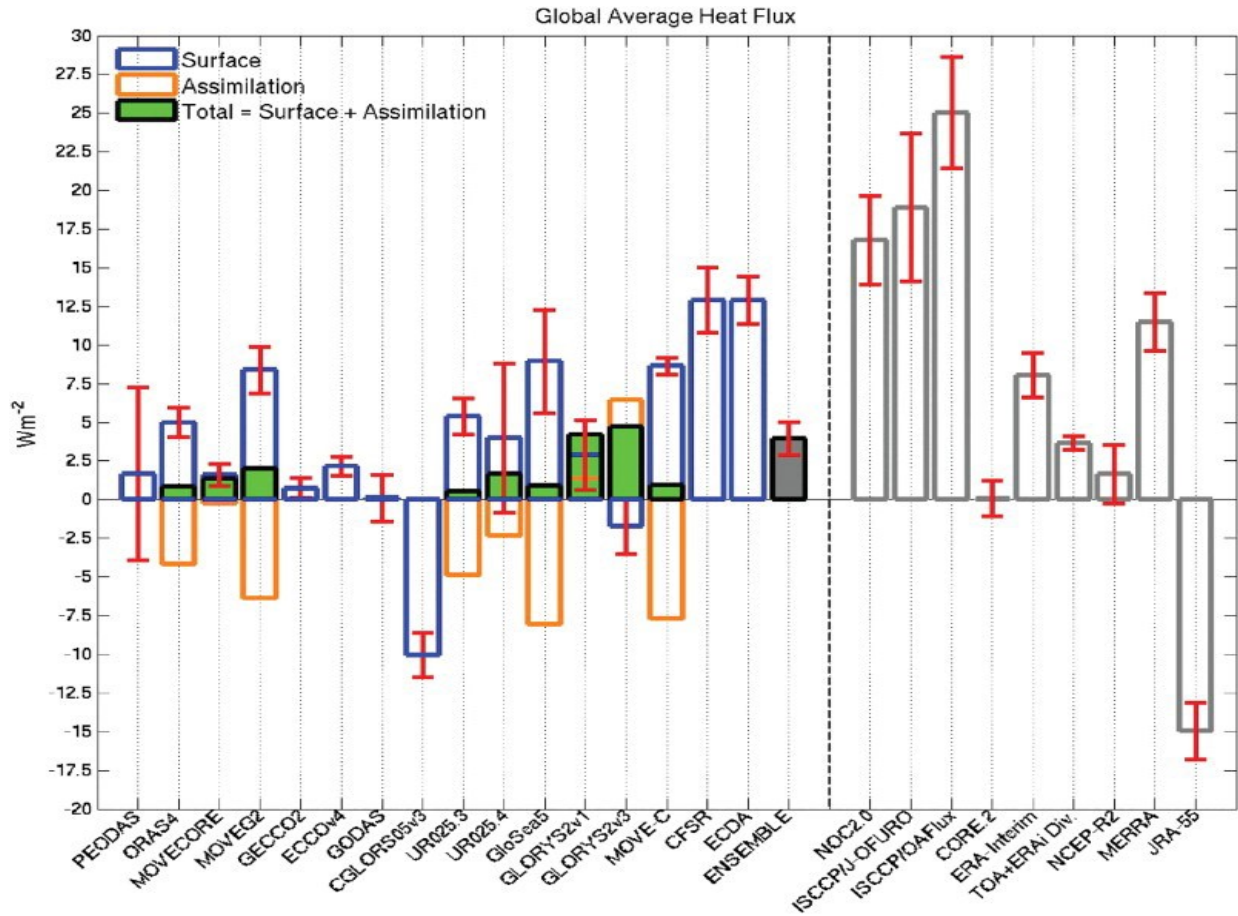


Figure 7 - Net Surface Heat Fluxes imbalance for different products over the 17 years [1993-2009] (ORA-IP) (Balmaseda et al. 2015)

Closure constraint

The deliberate closure of energy and mass budget is another approach to evaluate the model's performance. It imposes their fluxes to vary within their error ranges while simultaneously satisfy all energy and water cycle balance constraints (Wild et al. 2017); (L'Ecuyer et al. 2015b); (Siedler et al. 2013); (Josey and Smith 2006). It is an independent way to validate latent heat flux, among others (Ohmura 2014). Their variations should be very close to the evaporation estimations (Stocker et al. 2013). Linking both energy and water mass budgets reveals new physically consistent energy estimates and metrics for fluxes adjustment (L'Ecuyer et al. 2015b) (Table 1). This allows the original net surface heat flux of -16 W/m^2 to decrease to expected values consistent with TOA's *Radiative Forcing and OHC* of 0.45 W/m^2 .

Table 1 - Observed components of the globally and annually averaged energy budget and their uncertainties before and after optimization (Wm^{-2}). Last column shows readjustment of fluxes satisfying the constrained Surface NET flux to match TOA forcing (L'Ecuyer et al. 2015b).

Full Name	Abbreviation	Original	Constrained
Incoming solar	F	340.2 ± 0.1	340.2 ± 0.1
Outgoing shortwave	OSR	102 ± 4	102 ± 2
Outgoing longwave	OLR	238 ± 3	238 ± 2
Downwelling LW at surface	DLR	344 ± 6	341 ± 5
Downwelling SW at surface	DSR	189 ± 6	186 ± 5
Surface emitted	ULW	398 ± 5	399 ± 4
Surface reflected	USW	22 ± 2	22 ± 2
Sensible heat	SH	23 ± 5	25 ± 4
Atmospheric latent heat (precipitation)	P	78 ± 7	81 ± 4
Surface latent heat (evaporation)	LE	75 ± 7	81 ± 4
Atmospheric convergence	C	-0.6 ± 4	0 ± 1
Surface runoff (derived)	Q	3	0
Atmospheric water storage (derived)	dW	-4	0
Surface water storage (derived)	dS	3	0
Surface NET (derived)	NET	-16	0.45
Atmospheric NET (derived)	NETA	14	0

The resulting regional fluxes analysis is illustrated in Figure 8. Note how the fourth panel indicates regional surface fluxes that would require stronger compensating losses (e.g. via latent heat and precipitation). The spatial detection of overall flux direction is made possible. For example, The Gulf of Mexico and Caribbean Sea heating likely compensates the weak North Atlantic cooling (L'Ecuyer et al. 2015b).

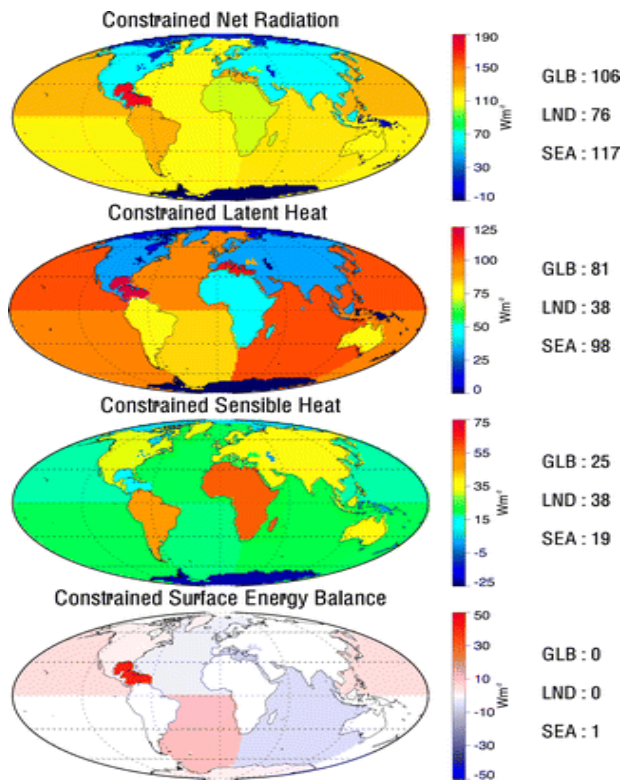


Figure 8 - Net energy exchange from the atmosphere to the surface after objectively introducing all relevant continental-scale energy and water cycle constraints (L'Ecuyer et al. 2015b).

Sub-grid drivers

Attributing observed change to external forcing at a regional scale

Sub-grid processes (Figure 1 e.g. wave height, ocean color, land-use changes) are progressively being added to the relevant OAGCMs. Their relative contribution to the *forcing* was previously averaged, or not considered at all, but they play a central role in establishing larger-scale atmosphere and ocean circulation pattern. Ultimately, they drive both weather and climate. As noted by Foken (2008), dataset's quality and accuracy can no longer be arguments for energy balance misclosure. Refined micro-scale processes are expected to eventually improve the fluxes' production and help close the budget (Kawai and Wada 2007); (L'Ecuyer et al. 2015b); (Rapizo et al. 2015); (Gentemann et al. 2003); (Simionato et al. 2003). For example, Babanin et al. (2012) that specialize in wave height's influence on air-sea interactions, also advocate for the detection

of mesoscale drivers. With their example of tropical cyclones generating large mixing events, they highlight the role of deeper layers activity in the ocean-wave models and SSTs. Would such deep mixing possibly “dampen” SST warming signals?

Outcomes

Figure 9 finally shows a comparison of global heat imbalances. As a result of many working group efforts, residuals are reduced to acceptable values within their respective expected accuracies. However, surface shortwave absorption and upward longwave emission are still unsure due to insufficient albedo and SST accuracy, neither is the attribution of surface fluxes into sensible or latent heat (partitioning) (Wild et al. 2017). Figure 9 shows the actual consensus using the closure constraint method. Without the artificial constraint, however, various occurrences of flux datasets still indicate an imbalance of net downward radiation exceeding corresponding turbulent heat fluxes by 13–24 W/ m² (L’Ecuyer et al. 2015b), the remnant *Closure Problem*.

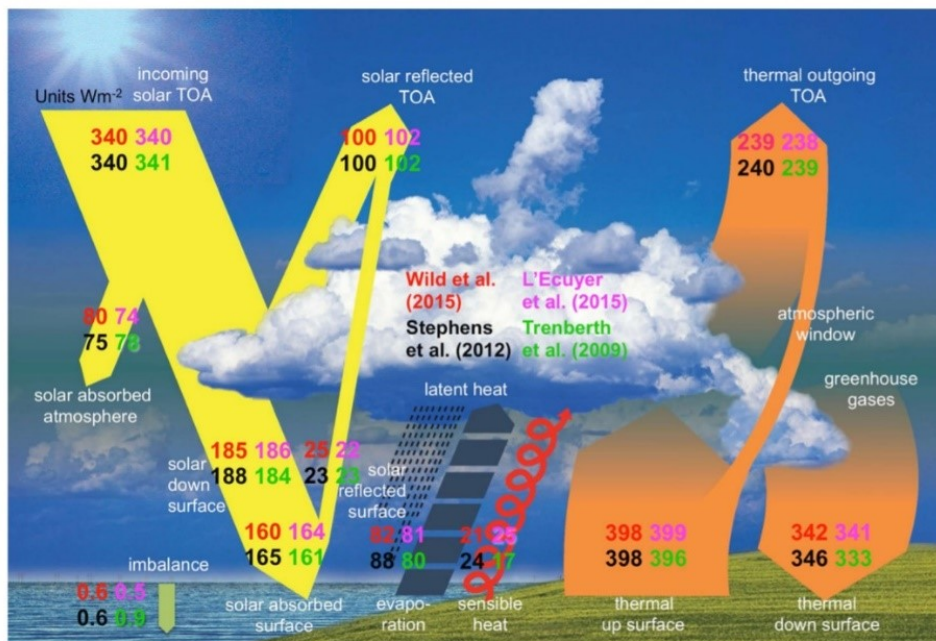


Figure 9 - Consensus for global annual mean energy balance partitioning of four major reanalysis products using closure constraint methods (fluxes in W/m^2). Net imbalance estimates range from 0.5-0.9 W/m^2 (Wild et al. 2017).

The common ground of the above cited articles regarding air-sea interaction is the recommended improvement of flux products. Despite the actual consensus, our knowledge of how the heat breaks down into radiative and turbulent fluxes is still incomplete. The fluxes parametrization and localization are the real challenges for the accurate modeling of the heat budget. The difference between original and constrained fluxes of Table 1 is remnant of unknown physics. The climate model's performance seems to stagnate and the need for additional physics is highly uttered. For Kiehl and Trenberth (1997), the largest source of uncertainty is "by far" in the absorbed SW radiation. Therefore, an assessment of the fate of the solar SW radiation is the next logical step.

Building on observational analysis, it is necessary to raise awareness on the sub-grid potential driver of upper layer shortwave radiation (SW) absorption rate. We think the key resides in the many documented bias regarding SST estimation, the oceans being responsible for most of the atmospheric thermal buffering (Abraham et al. 2013). Understanding interrelations occurring inside the surface layers of oceans may improve qualitative explanations of its heat uptake. Motivated by the potential evidence of its influence on the heat budget, the changing radiant heating rate (RHR) below the surface could be used to report unverified relationships. From remote sensing statistical observation, the ocean color changes seem non-negligible (Feldman 2020). Anthropogenic wastes spilled in oceans¹⁵ could alter its temperature. The spectral absorption of sun radiations into oceans depends greatly on their chemistry (Morel and Antoine 1994) and the overlaying Atmospheric Optical Depth (Levitus et al. 2005). In what proportions could pollution lead to non-negligible SST warming? Does this warming affect significantly the surface heat fluxes with the atmosphere? Answering these questions could help solve the *closure problem*.

¹⁵ “Material fluxes to the coastal zone are largely unidirectional, from the land to the sea, and these fluxes of sediments, biologically active materials and sometimes toxic compounds are rapidly increasing” (Simionato et al. 2003)

Upper Layer Heat Distribution

The upper layers of the oceans are thermally driven by many climatic variables. Table 2 of Mallick et al.(2019) is an example of relevant parameters driving the internal upper layer heat distribution to be included in a coupled OAGCM.

Table 2 - Drivers of the upper Heat Distribution (Mallick et al.2019)

Sl. No.	Forcing Parameter		Reference Height (m)	Spatial Resolution (in degrees)	Temporal Resolution
1	Meteorological	Specific humidity	2.0	Global (0.75° X 0.75°)	6-Hourly
2		Air Temperature	2.0		
3		Zonal wind	10.0		
4		Meridional wind	10.0		
5	Flux	Net solar radiation	Near Surface		3-Hourly
6		Net thermal radiation	Near Surface		
7		Total precipitation	Near Surface		

Mixing

The vertical distribution of the energy entering the surface is made through wind and wave induced mixing (well mixed above 6 m/s wind conditions (Zhang et al. 2020), the conduction of heat in depth being virtually null. Cool SST also sometimes forces the mixing even in the absence of winds by destabilizing the water column (convection) (Soloviev 2013).

Turbulent fluxes analysis hence also depends on the detection of wind variation. Young et al. (2011b)'s winds and wave height trend products show clear temporal and regional patterns, using 90th percentile and seasonal trend detection¹⁶ (Young et al. 2011a). The wind and wave height trend analysis recently contributed to refining air-sea coupled models through estimation of refined vertical sublayers (Stocker et al. 2013).

¹⁶ As a rule of thumb, the winter mixed layer is deeper than the summer, winds being stronger in the winter and weaker in the summer. (Soloviev, 2013)

Barrier Layer / Stratification

Another mode of heat distribution occurs when the mixed layer depth becomes shallower than the isothermal layer depth. Respectively being homogenous in density and temperature, the gap forming in between, known as the barrier layer (BL), inhibit the vertical mixing, trapping the heat at the surface. In the presence of freshwater sources of the Amazon-Orinoco River runoff, Balaguru et al. (2011) assessed the surface ocean response to such a BL forcing. By recognizing the salinity bias due to river plumes, they parametrize the corresponding BL and model¹⁷ the atmosphere and surface temperature responses to changed water and heat budget. They examined the SST bias caused by the BL, improving them by 10 to 15%. They realized that as few studies have focused on air-sea interaction, fewer have focused on feedbacks associated with freshwater (BL) changes. Their heat budget analysis reveals that increased latent and sensible heat loss to the atmosphere damps the SST increases in the region of BL increase.

The mixing exerts a control on the climate of the coupled system by dissipation of thermal energy to storm growth (Balaguru et al. 2011); (Babanin et al. 2012); (Mallick et al. 2019). Androulidakis et al. (2016) treated hurricanes forcing on ocean structure, and vice-versa. In their assessment of the evolution of three successive hurricanes, they found that the initial presence of a BL thermally fed the first hurricane. After its passage, the resulting dissipated BL and cooled, deeply mixed layer prohibited the thermal energy provided to the following two storms, limiting their intensity. This example of a river-induced BL and hurricanes intensification also highlights the effect of an auto-regulated SST. The heat buildup associated with BL enhancement is a requirement for big El Nino¹⁸ as well as important mixing events induced by hurricanes activity (Soloviev 2013); (Balaguru et al. 2011). It must be acknowledged that such dissipation of an SST warming make difficult the recognition of the signal otherwise apparent. Young et al. (2011b) wave height and mixing trends must be considered during the detection of SST warming trends and heat budget estimates.

¹⁷ NCAR SeaWIFS chlorophyll climatology was used for their SW radiation penetration estimates.

¹⁸ “The barrier layer favors the maintenance and displacement of the western Pacific warm pool into the central Pacific by isolating the mixed layer from entrainment cooling at depth and by confining the momentum of westerly wind events to a shallow mixed layer.” (Soloviev, 2013)

This thesis will challenge the weight given to turbidity into surface energy fluxes estimates. The ocean color is closely related to alluvion loaded freshwater runoffs. Like the BL, it is suspected to increase the stratification¹⁹ of the water column, trapping additional solar radiation near the surface, provoking an SST increase (Balaguru et al. 2011). “Induced stratification from surface heating reduces the depth of the turbulent boundary layer” (Bernie et al. 2007) as cited in (Weihs and Bourassa 2014), potentially forcing²⁰ the heat exchange with the atmosphere. Water is opaque to IR incoming radiation, regardless of its composition. In the visible band, however, water composition alters the stratification mode in upper layer (Kueh and Lin 2015); (Palmer 2014) trapping heat nearer to the surface when highly turbid.

DSST, the Diurnal Signal of Sea Surface Temperature

Under calm winds and clear skies conditions, the diurnal warming (DW) and cooling of the upper meters show a strong sinusoidal pattern throughout the day, generally peaking at 2 pm (Figure 10) (Gentemann et al. 2008). Typically ranging from 0.5°C to 3 °C, the SST difference between daytime and nighttime (DSST) can reach values up to 5-8 °C (Zhang et al. 2016). This magnitude is seasonal. High wind and stress induced vertical mixing remove the diurnal signal (Bernie et al. 2007); (Sathyendranath 2000).

¹⁹ Water layers properties gradient (temperature (thermocline), salinity (halocline), density (pycnocline), turbidity (lutocline) that act as barriers to mixing.

²⁰ A forcing is positive when the energy flux is leaving the ocean to the atmosphere. Negative otherwise

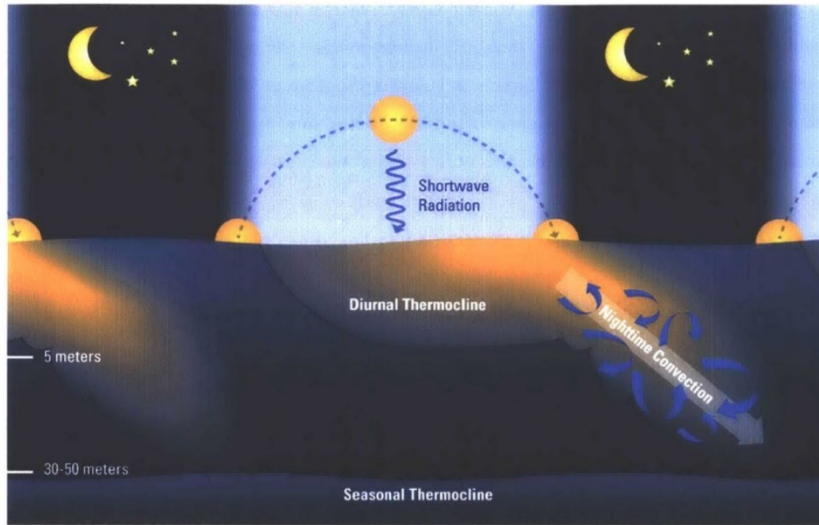


Figure 10 - Schematic representation of DSST into the mixed layer. Illustration by Eric S. Taylor, WHOI, as cited in (Bogdanoff et al. 2017)

DW is not yet included in current climate models, but its importance for the resolution of air-sea interaction is being increasingly recognized (Kawai and Wada 2007); (Bernie et al. 2007); (Weihs and Bourassa 2014); (Zhang et al. 2020). For example, Bogdanoff et al. (2017) shows that an underestimated DW would induce errors in the heat fluxes to the atmosphere of 50 to 60 W/m^2 during low wind conditions.

The inclusion of the diurnal SST (DSST) signal into climate models could potentially solve a part of the Closure Problem by increasing the weigh of outgoing fluxes out of the ocean (Bogdanoff et al. 2017); (Kawai and Wada 2007); (Weihs and Bourassa 2014); (Zhang et al. 2019); (Schiller and Godfrey 2005). These authors' approaches to integrate the signal are similar, using one-dimensional ocean heating model ("POSH") to simulate de diurnal warming (Weihs and Bourassa 2014). However, Soloviev (2013) warns about a weakness regarding the traditional Monin-Oboukhov similarity approach used in coupled models, which is not straightforward for DSST sublayers : due to kinematic mixing coefficient of water being 30 times smaller than air, the heat propagation in layers of ocean is much slower than in the atmospheric boundary layer, making the Oboukhov scale irrelevant. The room for improvement regarding DSST sub-layer directs our research.

Among studies, the various estimates of the four heat fluxes composing the Earth’s heat budget, corrected after the addition of a DSST sublayer, are coherent. Table 3 shows an example of the correction brought to the radiative and the turbulent fluxes leaving the surface when DW is considered. Note how these components correspond to three of the four key fluxes composing the heat budget presented in (1). Later in 2007 Bernie et al. (2007) assessment of the response of the Madden-Julian oscillation to a rectified SST showed that the inclusion of DSST led to an increase of 0.2°C to 0.3°C. This impact on climate is predicted in Bernie et al. (2007) Part II. Schiller and Godfrey (2005) showed that diurnally forced changes of latent heat fluxes (10–20 W/m²) are more important than sensible (<3 W/m²) and longwave radiation (<1 W/m²). Those heat fluxes’ differences improve agreement with observations and potentially alter the feedback mechanisms on climate change timescale (Gentemann et al. 2008); (Gentemann and Hilburn 2015); (Zhang et al. 2019); (Zhang et al. 2016)); (Soloviev 2013). Also, through their multi-year spanned work, Kawai and Wada (2007) broadly explored the parametrization of the tropical warm pool diurnal warming DW events, while Webster et al. (1997), Clayson and Bogdanoff (2013) and (2017), major contributors to Earth’s heat budget Reanalysis, investigated the importance of using skin layer in calculation of air-sea interactions. All these studies mention the need for improvement of SST variation quantification methods.

Table 3 - Surface heat fluxes’ change associated with an SST increase of 1 °C simulating a DW. (TOGA COARE IOP) (Webster et al. 1997)

Component	Flux Change	
	(Wm⁻²)	(%)
Upwelling Longwave	6.3	1.3
Sensible Heat	2.4	23.3
Latent Heat	18.7	16.2

Light Absorption and Transmission

The temperature of the upper ocean depends primarily on the volume absorption of penetrating solar radiation resulting in a local increase of heat content²¹ (Soloviev 2013); (Morel and Antoine 1994). The sun acts as an approximate blackbody and emits an electromagnetic energy field mostly distributed in the UV, visible and IR spectrums (Figure 11). Due to opacity of atmospheric gases in the near-IR region, not much energy reaching the surface subsists beyond 2.5 μm (Morel and Antoine 1994). The propagation mode of the sun's energy into the ocean's depth is subjected to the physical composition of the water body. The energy is either reflected, absorbed, scattered, or transmitted. The absorption coefficient is an Inherent Optical Property (IOP) of pure water and its constituents. It is not constrained to the direction or the intensity of downwelling flux but is rather intrinsic to every material. The relative abundance of constituents inside the water body defines its total absorptivity, as they are simply stacked (5).

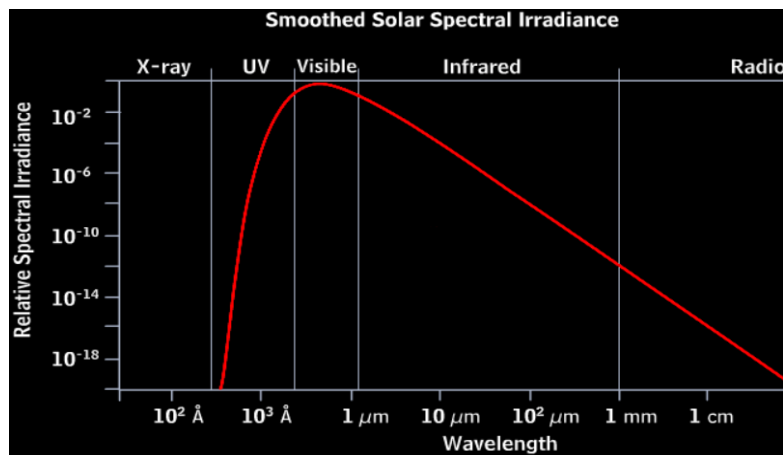


Figure 11 - Electro magnetic energy distribution of a blackbody, mostly in the visible range. Log scale. Image courtesy of the COMET program and the High-Altitude Observatory at NCAR.

²¹ "The top 2-3 m of the ocean has the same heat capacity as the entire atmosphere above. Of the penetrating solar radiation, 50% is absorbed within the first 0.5 m of the ocean." (Soloviev, 2013)

$$a_{\text{tot}}(\lambda) = a_w(\lambda) + a_{\text{phyt}}(\lambda) + a_{\text{CDOM}}(\lambda) + a_{\text{NAP}}(\lambda) \quad (5)$$

Where

α_w is the spectrally dependent absorption coefficient of light by pure water,

α_{phyt} for phytoplankton,

α_{CDOM} for Colored Dissolved Organic Matter,

α_{NAP} for non algal particles (NAP). (Kim et al. 2016)

K_{d490}: The Solar Beam Attenuation Coefficient for Downwelling Irradiance (m⁻¹)

The attenuation coefficient K_d , an Apparent Optical Property (AOP), defines the observed removal rate (m⁻¹) of beam energy with depth due to absorption (Soloviev 2013) and is the variable used in this study to answer the thesis question.

The Radiative Transfer Equation (RTE) ties together the AOPs and IOPs and describes the fate of the irradiance after it reaches sea surface (Ohlmann et al. 2000). Converting one into another and retrieving observed diffuse K_d requires measurements of remote sensing reflectance R_{rs} .

In coupled models, K_d is sometimes used to predict the vertical profile of the radiant heating rate (RHR). The volume absorption of downwelling irradiance due to pigment concentration is responsible for a local heat increase (Morel and Antoine 1994). Exponential function in equation (6) model the decay of energy along the depth from the surface (Kim et al. 2016).

$$I_d(z, \lambda) = I_d(0, \lambda) \exp \left[- \int_0^z k_d(z', \lambda) dz' \right] \quad (6)$$

where $I_d(z, \lambda)$ [W/m^2] is the downward irradiance at a given depth z and wavelength λ , $I_d(0, \lambda)$ [W/m^2] is the irradiance entering the surface, and $K_d(\lambda)$ [m^{-1}] is the light attenuation coefficient.

K_d varies spectrally²² as shown in equation (6). The literature made very common the subdivision of visible sunlight into two spectral band; the Infrared (IR) and the blue-green “rest” (Gentemann and Hilburn 2015). The ratio between this visible irradiance to total irradiance reaching surface is approximately 0.43 (Chang and Dickey 2004). In the IR band, pure water attenuation coefficient dominates the absorption of the water body, regardless of its constituents. Earlier studies hence observed that in upper centimeters, changes of pigment concentration was of little interest in the heat budget (Ohlmann et al. 2000); (Soloviev 2013); (Morel and Antoine 1994), building around the assumption that the resulting heating is un-important. Pure water absorption ranges multiple tenfold higher in IR wavelengths (above 700 nm). Hence the need for a 2-band assessment (Bukata et al. 1995).

In current generation models, it is the chlorophyll amount (an IOP) that leads the parametrization of AOP K_d (Bogdanoff et al. 2017). The parametrization is made using Jerlov’s Water Types (Jerlov 1976) and Morel’s case I and case II water (Morel and Antoine 1994) best-fit analysis. They are optical statistical classification of water bodies representing varying oceanic and coastal turbidity, which provides different empirical relationships like equation (7), accounting for chlorophyll (chl) concentration and light absorption α_{dg} by colored detrital matter (CDM) (Kim et al. 2016):

$$k_d(\text{bg}) = 0.0232 + 0.0513\text{chl}^{0.668} + 0.710a_{dg}(443)^{1.13} \quad (7)$$

²² Note that the inherent absorptivity of these individual constituents have their peak more or less around the waveband 490, hence the common use in nomenclature of variable K_{d490} for the attenuation detection and monitoring (Lee et al., 2005).

The heat fluxes caused by an increased chlorophyll pigmentation suggest that an appropriate optical parameterization scheme is not negligible for the heat budget model. The Jerlov classification was an efficient tool for the early generation GCMs, incorporating very broad estimates of the ocean's attenuation coefficient (Kueh and Lin 2015); (Soloviev 2013). However, estimates of heating rate profile in response to pigment concentration is often underestimated in the upper layers and overestimated deeper (Kawai and Wada 2007); (Ohmura 2014); (Kim et al. 2016). For example, Chang and Dickey (2004) found that an increase of a tenfold in chlorophyll concentration will increase attenuation in the visible band of more than 0.15 m^{-1} within the upper 10m, which is equivalent to 30 w/m^2 based on a 200 W/m^2 irradiance (Ohlmann et al. 2000). Gentemann and Hilburn (2015) evoke the feedback of a growing phytoplankton population enhancing the light attenuation. They address the sensitivity of SST to Diurnal Warming signal, showing that chlorophyll-a can increase diurnal warming stratification. Also, Soloviev (2013) discusses the altered profile of SW radiation absorption by episodic or seasonal changes of phytoplankton growth and biological productivity, significantly affecting turbidity. These examples highlight the pertinence of light attenuation monitoring for the surface heat budget.

Pertinence of Depth (Z_{crit}) for the Heat Budget

“Shortwave heating in the ocean is determined by the abundance of materials in the water and heat content and temperatures are lower in an ocean model with yellow materials than one without”. These are the key points outlined in the Kim and Gnanadesikan (2018) study on upper layers' attenuation by CDM. The study builds around a base-case simulation of ocean heating. Their experiment recreates a living ocean with changes in light attenuation resulting from both the addition of CDM and induced changes in phytoplankton concentration. They predict K_d by a biogeochemical model (chlorophyll oriented).

Their results indicated that the colored organic materials creating a shallower attenuation depth, preferentially heated the water closer to the surface, while light propagation to deeper waters is reduced. Radiative heating is increased for the top 10 m and reduced in the 20-30 m depth layer. The depth at which this inversion of heating rate occurs is called Z_{crit} throughout the thesis and is a key concept for the discussion.

Hence, Kim and Gnanadesikan (2018) mention reduced OHC in the upper 700m as the integrated impact of these temperature changes. However, suggesting that an increased CDM acts as “a buffer for global warming” is misleading. they seem to undermine the gain from the warmed surface layer that forces the atmosphere with enhanced turbulent fluxes (LHQ and SHQ). Their interpretation that an overall ocean cooling behaves as a buffer for atmospheric warming is puzzling, as the acknowledged warmer upper layer forcing could represent, on the opposite, an additional source to the increased atmospheric temperature. When considering the Closure Problem, the mysterious excess heat could even be attributed to this warmer upper layer. Yet, they acknowledge this possibility throughout their analysis, indicating how the additional ocean heat loss due to shallower solar radiation absorption destabilized the water column. The contradiction found in their interpretation may be explained by their arguable vision of a forcing atmosphere on the oceans, instead of a mutual driving. As they articulate: “In recent decades, the warming atmosphere has warmed the ocean.” (Kim and Gnanadesikan 2018). This sentence is misleading as it suggests the passiveness of the ocean in the heat exchange, overlooking its driving power. Also, they acknowledge the misfit of their model with last decade empirical observations of temperature, that are opposite in signs. Nevertheless, we agree with their recommendation that raises the question on the impact of land use changes increasing river runoff discharges in the Arctic Ocean. It legitimizes our objective to identify the impact of increased anthropogenic pollution in ocean heating rates.

K_d Parametrization in recent studies

The fact that K_d parametrization is set to vary only with chlorophyll concentration has its downsides. Simply correlating the contribution to absorption of a single constituent ignores the cumulative signature of the totality of components (Bukata et al. 1995). As pointed in Sathyendranath et al. (2017)'s Figure 12, the adequate categorization of water bodies becomes complicated for coastal waters where many input occur. Especially considering the anthropogenic actions spatially and temporally driving K_d . Hence, "Case I optically insignificant" water could have become optically overwhelming "case II" without being considered as such into models. This lack of real-time feedback could cover a shift occurring in the proportion of ocean having case II characteristics rather than case I. This suggestion relies on the age of referenced empirical relationships dating from 1976 (Jerlov 1976) to 1986 (Kirk 1986) and the most plausible augmentation since then.

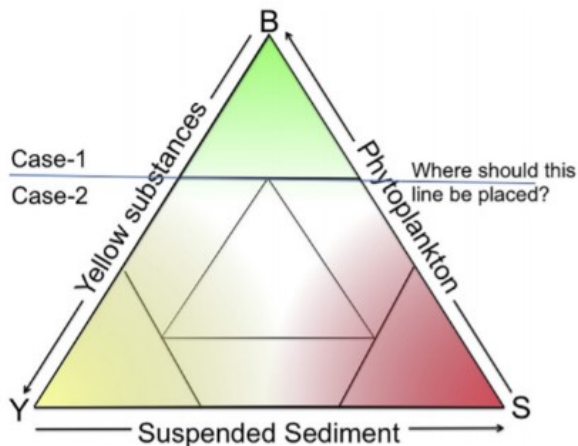


Figure 12 - Case 1 and Case 2 waters relatively attributed to tripartite diagram of selected constituents' contribution to the total attenuation (Sathyendranath et al. 2017)

Literature typically considers sun radiation to be absorbed within a Mixed Layer Depth (MLD), or fix a global K_d for the entire ocean (Shell et al. 2003); (Balaguru et al. 2011); (Mallick et al. 2019). For example, Bernie et al. (2007)'s three-band exponential absorption is built following a globally constant chlorophyll concentration of 0.05 mg m^{-3} , regardless of location or time. In their analysis regarding Surface Heat fluxes response to Barrier Layer, Balaguru et al.

(2011) use outdated dataset ; a fixed averaged chlorophyll concentration corresponding to type 1 (clear) Jerlov's Water Type for attenuation profile. In their conclusion, they suspect this constant turbidity to be responsible for the weak SST response in large BL increases, as it does not reproduce the exact effect of Amazon river discharge. Bukata et al. (1995) also admits generalizing water properties with an "equivalent homogeneous water body".

Unlike currently used algorithms, Lee et al. (2005) developed in 2005 a semi-analytic algorithm to retrieve K_d from remote sensing reflectance (R_{rs}) and absorption (α) and backscattering (β) ratios. His results show an evident improvement of K_d datasets accuracy. Unlike the conventional categorization of the water body into cases, the semi-analytic method does not require such a separation into subsets of data. Lee et al. (2005) has the approach preferred by ESA OC-CCI to produce their diffuse attenuation coefficient K_{d490} from remote sensing reflectance, the same dataset chosen for the purpose of this thesis.

Studies of coastal ocean processes on heating rate are rare (Chang and Dickey 2004) but their pertinence is increasingly acknowledged. For example, a recent pilot numerical experiment of the thermal structure at the NINO3.4 region revealed the cold bias associated with a poorly parameterized K_d in the visible waveband and its impact on the upper 100m temperature (Kim et al. 2018). Ohlmann et al. (2000) found upper-ocean CDOM concentrations to be responsible for SW absorption fluctuations reaching 40 W/m^2 . In 2004, Chang and Dickey (2004) were among the first to use remote sensing measurements in radiative transfer simulation to investigate the heating in coastal waters. They indicate that CDOM has a significant impact on solar transmission. Heating of the Arctic waters increased by 30% in the top 10m due to changed optical properties. The absorption by CDOM increased the ice melting rates in this region (Pegau 2002) as cited in Chang and Dickey (2004). They emphasize the effect of stratification trapping heat near the coastal water surface, reaching 4.7°C and 5°C differences according to their literature. Lastly but not least, Mallick et al.(2019) study modeled the altered upper ocean thermal structure in the Bay of Bengal. Local phytoplankton growth following nutrient input enhances the surface warming and stratification.

Thesis Question

Hypothesis: Anthropogenically driven K_d significantly changes the ocean surface layers' heating rate profile, forcing the air-sea heat fluxes.

If optically responsive aquatic components have accumulated into the oceans, would their visible energy absorption significantly drive the surface energy transfer? Anthropogenic changes in Ocean Color affects its upper layer heat distribution mode. To report the influence on climate, SST and K_d time series are assessed. Their spatial and temporal evolution are collocated and compared. The relationship is highlighted through the detection of a matching trend between both variables, as well as the empirical determination of the associated forcing. Energy conservation equations are used and depicted.

To verify this prediction of a mutual influence, a third climatic variable is included in the comparison: DSST. The diurnal sinusoidal signal of SST is expected to have higher amplitude in areas with increased turbidity. This should take the form as a positive (negative) DSST trend for areas of positive (negative) K_d trend.

Contribution

L'Ecuyer et al. (2015a) insist on understanding the inconsistencies and unsolved issues of the budget to track the accumulating energy. Improving the estimates of the independent physical variables composing the turbulent fluxes is the OAFlux key strategy (Yu et al. 2007). Our analysis could support this need of a better SST retrieval. If significant, the answer to the question could promote an increased attention around ocean color management. The ramifications of mitigations in the field are numerous, ranging from better monitoring to actual Ocean cleaning campaign. Improved predictive models leads to strategies to tackle climate change issues, ensuing well known beneficial consequences for society. The expected outcome of the analysis has social and scientific importance, as it represents an “opportunity for the development of better observational tools to understand the variability of solar extinction” (Bogdanoff et al. 2017).

The question could also lead to a managerial shift in climate program budgets. For example, the American government budgets for NASA's programs are very weather-forecast oriented. Major budget reductions were requested from 2017 to 2019 for the National Environmental Satellite, Data and Information Services, passing from \$2,187,445 thousands in 2018 to \$1,640,021 thousands in 2019 (compared to a smaller reduction for the National Weather Services and others.) (U.S. Department of Commerce 2019). An improved understanding of the oceans' influence on the Earth's *Radiative Forcing* could encourage re-investments into appropriate remote sensing missions.

The inclusion of DSST in the analysis could help identify schemes regarding the variability of SST and K_d , allowing to account for their undetermined relationship. It may finally map the way ahead for future research on air-sea interactions and global warming.

CHAPTER 3 Methodology

The approach employed is quantitative, as the analysis was made from statistical regression of empirical remote sensing measurements. The 3 variables (SST, Kd, DSST) were collected from public FTP servers in NetCDF or Binary files and are open and read using MATLAB. Trends were extracted from timeseries Datasets using the seasonal Mann-Kendall test (Young et al. 2011a). Resulting yearly trends were mapped on a 1° x 1° grid (1° is 1 meridian), averaging surrounding values when the original dataset had a finer grid. This facilitates the intercomparison of the spatiotemporal evolution of the 3 variables. Table 4 reunites all imported variables and associated documentation.

Table 4 - Summary of input dataset

Parameter	Abr.	Dataset	Satellite	Period	Algorithm	Reference
Sea Surface Temperature	SST	OAFflux	AVHRR TMI AMSR DMSP	1987- 2017 30 yrs.	COARE bulk flux 3.0 (Fairall et al. 2003).	WHOI OAFflux project (http://oafux.whoi.edu) funded by the NOAA Climate Observations and Monitoring (COM) program.
Diurnal Sea Surface Temperature	DSST	AMSRE AMSR2	REMSS- Aqua	2002- 2017 16 yrs	AEs Ocean (Wentz, 2000)	Remote Sensing Systems (REMSS) sponsored by the NASA Stand Alone Mission of Opportunity (SALMON) program. www.remss.com/missions/amr .
Attenuation coefficient (490 nm)	Kd	OC-CCI	MERIS SeaWIFS MODIS- Aqua VIIRS	1998- 2017 20 yrs	Lee et al. (2005)	Ocean Colour Climate Change Initiative dataset, Version occi-v3.0, European Space Agency, http://www.esa-oceancolour-cci.org/
Surface Solar Radiation	I ₀	ERBE srb	NOAA 9 NOAA 10 ERBS	1998 1 yr	Li et al. (1993).	NASA-GEWEX Surface Radiation Budget (SRB), release 3.0 dataset

The trend extraction method was chosen for its resource's high accessibility and its low-cost use. The conduction of the research itself does not present any apparent ethical issue.

Criteria for dataset selection

SST

The SST trend was calculated on a monthly average basis and secures a handy climatology. The validity of MATLAB statistical algorithm will be verified through this resulting map by comparing the result with existing climatology (Figure 4). WHOI produces the Objectively Analyzed air-sea Fluxes (OAFlux) SST dataset. It is initially a Reynold's daily OI SST 0.25-degree grid, monthly averaged into a 1-degree grid. Reynold's OI SST is a spatially smoothed 7-day SST average. It is a combination of AVHRR, microwave and IR instruments, NWP outputs and in situ buoys observations of SST²³. The original L4 product is a blended combination, spanning over 57 years (From 1960 to 2017). The OAFlux product used for the trend extraction ranges from 1987 to 2017 to match the beginning of remote sensing observations. This SST product represents a foundation SST (SST_{fnd} in Figure 5) at a depth of ~1 meter (temperatures just below the diurnal layer). WHOI FTP server was the chosen provider because blended turbulent fluxes and vector winds datasets were also publicly available, if needed in analyses.

DSST

The detection of a surface diurnal signal requires the use of a subskin (1 mm depth, Figure 5) daily SST product from a single source (unblended) measurement. AMSRE and AMSR2 are two consecutive REMSS satellite-based microwave radiometer. They were chosen because their convenient SST sampling nominal observation time (equatorial crossing time of 1:30 PM Ascending and 1:30 AM Descending conveniently matching temperature peaks), collected at a spatial resolution of 25km (0.25-degree grid). Also, as opposed to IR measurements, MW measurements are not obstructed by cloud cover. IR instruments measure a SST_{skin} depth of about 20 micrometers while MW instruments measure the temperature of ~1 mm thick SST_{subskin}. The caveat to this MW dataset is the small temporal coverage (2002 to 2017) with a gap between 2011 and 2012 during a satellite mission shift between AMSRE and AMSR2. Also, their lower spatial

²³ Please acknowledge the global ocean heat flux and evaporation products were provided by the WHOI OAFlux project (<http://oaflex.whoi.edu>) funded by the NOAA Climate Observations and Monitoring (COM) program.

resolution of 25km, compared to 1-4 km resolution for IR instruments, scales inversely with the amplitude of the measured diurnal heating for coastal regions (Gentemann et al. 2008). This compromises the SST accuracy for coastal areas, which is critical for this study.

K_d

The diffuse attenuation coefficient of downwelling irradiance K_d at a wavelength of 490 nm is suggested to predict the heating rate of oceans surface (Morel and Antoine 1994); (Bukata et al. 1995); (Schiller and Godfrey 2005). MERIS, MODIS, VIIRS and SeaWiFS satellites datasets were merged per-pixel and used to retrieve the global K_{d490} over the period of 1998 to 2017 (V3.0). The daily level-3 K_{d490} were downloaded from the NASA ocean color FTP server website²⁴, which has global coverage and a spatial resolution of ~ 4 km/pixel (1/24-degree grid). K_{d490} was computed from the IOP (absorptivity and backscattering) and reflectance by the quasi-analytical algorithm (QAA) developed by (Lee et al. 2005). This thesis concerns quantifying the energy excess trapped near the surface and the implication for the air-sea forcing. Although this estimate should include a more complete spectral analysis, it was considered enough to use this only wavelength (490 nm) as an approximation for the rest of the depth and wavelength dependent attenuation coefficients, similar to the common methodology.

²⁴ Ocean Colour Climate Change Initiative dataset, Version occci-v3.0, European Space Agency, available online at <http://www.esa-oceancolour-cci.org/>

I_0

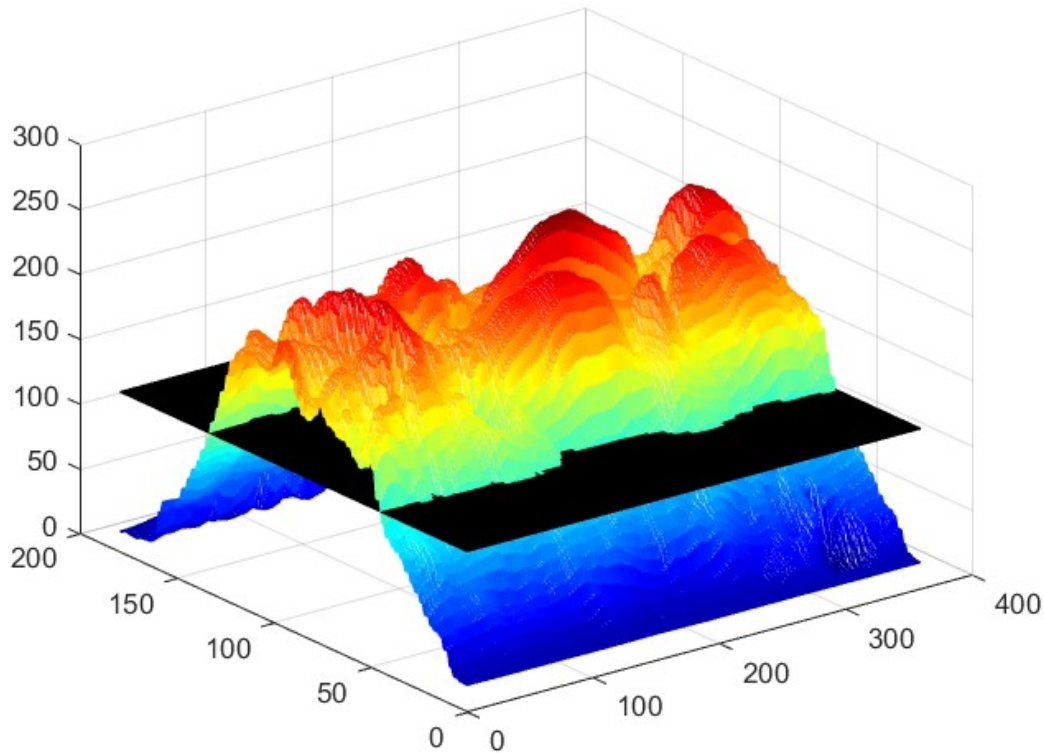


Figure 13- 3D Mapped mean incoming irradiance I_0 [W/m^2] on the Earth surface (NASA-GEWEX Surface Radiation Budget (SRB), release 3.0 dataset).

The surface solar radiation I_0 is the energy in W/m^2 that reaches the Earth's surface once it traveled through the atmosphere. It is dependent on the atmosphere optical depth as well as the latitude, hence the curve bell allure of the Figure 13 along the latitude axis. Figure 13 shows the 1998 NASA-GEWEX dataset that combines 3 satellite measurements (NOAA 9, NOAA 10, ERBS) (Raschke et al. 2012). The x and z axes represent the Earth's coordinates, while the y axis is the incoming Irradiance in W/m^2 . The black surface represents the average I_0 of $122 W/m^2$. This mapped I_0 was used in the calculation of the forcing, weighting the contribution of K_d trend, depending on the irradiance intensity.

Trend extraction procedure

This section describes the mathematical relationships and steps that were translated and ran into MATLAB codes. These statistics were inspired by Young et al. (2011a). The Seasonal Mann-Kendall (SK) test (Gilbert 1987) is derived from a simple linear regression model of the form:

$$y(t) = at + b \quad (8)$$

With the set of slopes:

$$a_{ij} = (y_j - y_i)/(t_j - t_i)$$

where:

$(t_j - t_i)$ is the time difference between two observations i and j ; $1 \leq i \leq j \leq n$

When the full dataset is seasonal, subdivided into 12 months in our case.

Sen's slope:

$$a_{ijk} = (y_{ij} - y_{ik})/(t_{ij} - t_{ik})$$

The SK test is a non-parametric (no normal distribution) test of randomness against trend where the null hypothesis h_0 states that the variables are independent and randomly distributed (no trend). Rejecting the null hypothesis (h_1) implies a trend is present.

To determine statistical significance of the trend:

The sign of all $n(n-1)/2$ possible differences is summed into S_i for each month i .

$$S_i = \sum_{k=1}^{m_i-1} \sum_{j=k+1}^{m_i} \text{sgn}(y_{ij} - y_{ik}) \quad (9)$$

where

$$\text{sgn}(x) = \begin{cases} +1 & \text{if } x > 0 \\ 0 & \text{if } x = 0 \\ -1 & \text{if } x < 0 \end{cases} .$$

The Variances of S_i are computed:

$$V(S_i) = n(n-1)(2n+5)/18$$

Under the assumption of H_0 , the distribution of S is symmetric and normal

$$S' = \sum_{i=1}^{12} S_i \quad (10)$$

$$V_{S'}^2 = \sum_{i=1}^{12} V_{S_i}^2 + \sum_{\substack{i=1 \\ i \neq l}}^{12} \sum_{l=1}^{12} \text{cov}(S_i, S_l) \quad (11)$$

Finally, the statistic $Z = [S' - \text{sgn}(S')] / (V(S_i)')^{1/2}$ is tested against the value $Z_{\alpha/2}$

if $|Z| < Z_{\alpha/2}$; H_0 is accepted

$(1-\alpha)$ is the standard level of confidence, with $\alpha = 0,05$

Rejection of H_0 , implies a statistically significant trend, with a positive value of Z indicating an increasing trend and a negative value a decreasing trend and the median value of all a_{ijk} seasonal Sen's slopes an estimate of the trend magnitude (Young et al. 2011a).

The dotted result of a single pixel of monthly K_d for a period of 23 years is shown in Figure 14. This time-series illustrates the seasonal variation pattern of attenuation values for a single point. The slope of the red line is the trend obtained from the described above operations. Each value of

the mapped results is a similar slope. Note how a satellite mission shift induced a sudden drop of K_d mean value shortly after 2016. It will be discussed later why the chosen period assessment excludes those last three years of data (red circle of Figure 14).

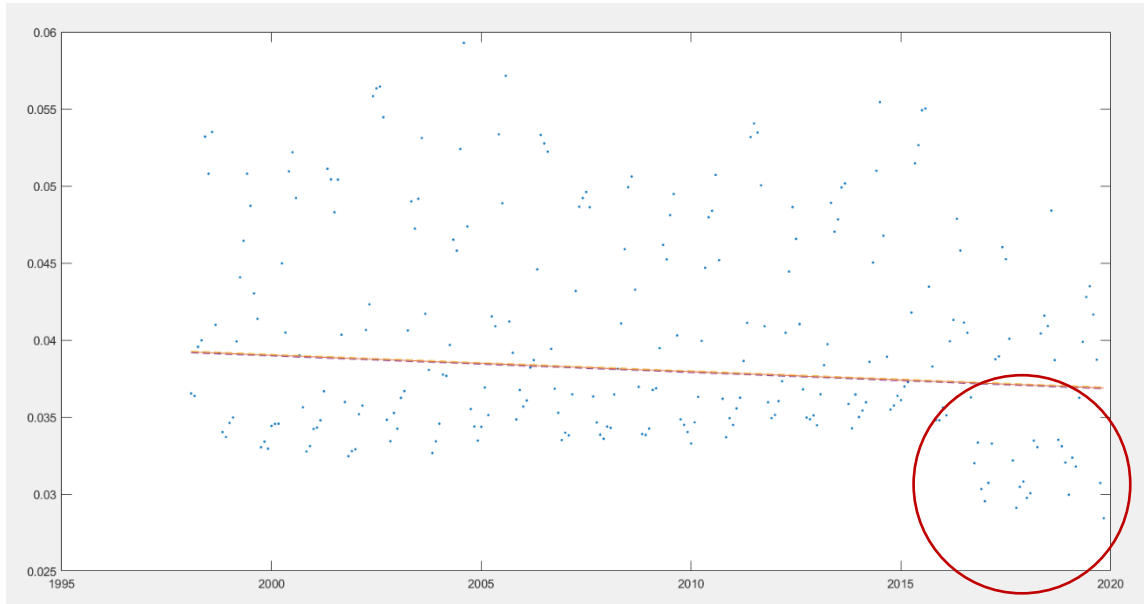


Figure 14 - Example of trend calculation for one bin. Each individual pixel of the mapped input has a resulting red slope, determined from above algorithm. The final result is a map of each calculated trend (slope). The red circle highlights an example of a bias in the K_d input dataset following the 2016 satellite mission shift, which is discussed further in limits.

Correlation Coefficient

All variables are compared bin by bin with each other using the Curve Fitting Tool in MATLAB to verify if their values are correlated. Similar to Zhang et al. (2019) who mapped the SST dataset into $10^\circ \times 10^\circ$ bins size, each of the variables is concatenated into a coarser grid of 18×36 bins. They are spatially compared, excluding the “Nan” values in the process. A good correlation will be an indicator that the compared variables are evolving spatially and temporally in the same direction. This will lead to further interpretations. The main objective is to verify how SST is dependent on K_d .

Forcing on Air-Sea Heat Flux

This thesis aims to quantify the role of changing surface heat redistribution on climate, considering the ocean’s ability to store and transport large quantities of heat. The upper few meters heat storage capacity is equivalent to the entire volume of the Earth’s atmosphere (Palmer 2014).

The first law of thermodynamics is the starting point for the solution of this heat transfer problem (Bergman et al. 2011). The heat storage term of the conservation of energy may be expressed as equation (12) (Morel and Antoine 1994):

$$dT(z,t)/dt = E_{abs}(z,t)/\rho C_p \quad (12)$$

With:

- Radiant Heating Rate (RHR) ($^\circ\text{Cs}^{-1}$): $dT(z,t)/dt$
- Energy absorbed per unit of volume (Wm^{-3}): E_{abs}
- Depth (positive downward) (m): z
- Temperature (K): T
- Density ($\sim 1025 \text{ kg m}^{-3}$): ρ
- Thermal capacity of water ($\sim 4.17 \text{ kJ(K)}^{-1}\text{kg}^{-1}$): C_p

The energy absorbed may also be expressed as

$$E_{\text{abs}} = \alpha \dot{E} = K_d I(z) \quad (13)$$

With: Absorption coefficient (m^{-1}): α
 Scalar irradiance (Wm^{-2}): \dot{E}
 Beam solar attenuation coefficient (m^{-1}): K_d

Assumptions:

- Vertically homogeneous water body (K_d constant with depth. Actually, it varies with depth).
- All radiometric quantities (I , K_d , α) are wavelength dependent. λ has been fixed at 490. (Morel and Antoine 1994)
- α is approximated with K_d (Mobley 1994) as cited in (“Ocean Optics,” n.d.)

The profile of the Irradiance decay function with depth is expressed as:

$$I(z) = I_0 \exp(-K_d * z) \quad (14)$$

With: I_0 the incoming Irradiance²⁵ reaching the surface $z=0$

The equation (14) is the same as the previous equation (6). In equation (14), the first e-folding depth of incident light is called the attenuation depth and is the reciprocal of K_d . The theoretical maximum attenuation depth of 43m is the reciprocal of the smallest possible attenuation associated with pure water, which is $1/0.0232 \text{ m}^{-1}$ (Kim et al. 2016).

²⁵ The surface solar radiation is derived from the National Aeronautics and Space Administration (NASA)/Global Energy and Water Cycle Experiment (GEWEX) Surface Radiation Budget (SRB), release 3.0 dataset (ERBESrb-Li_EdXXX).

The K_d trend is used to find changing irradiances and heating rates profiles along the depth in the upper 50 meters. Both irradiances decay I_{01} and I_{02} where mapped for K_{d1} and K_{d2} , where K_{d1} is the annual mean of K_d values for the whole initial year of 1998 and K_{d2} is the sum of K_{d1} with K_d trend for the timespan of 18 years as such:

$$K_{d2}=K_{d1}+K_{dtrend} \quad (15)$$

Two RHR profiles [K/day] are derived from each Irradiance profiles associated with initial and final year values (1998 and 2017) (Chang and Dickey 2004):

$$RHR_1=[K_{d1}*I_1(z)] / \rho C_p \quad (16)$$

$$RHR_2=[K_{d2}*I_2(z)] / \rho C_p$$

The depth Z critical (Z_{crit}) where RHR_1 and RHR_2 curves cross satisfies the following equality:

$$[K_{d1} * I_1(Z_{crit})] / \rho C_p = [K_{d2} * I_2(Z_{crit})] / \rho C_p \quad (17)$$

Equation (17) then simplifies to the logarithmic relationship when Z_{crit} is isolated. Z_{crit} is dependent only of K_{d1} and K_{d2} :

$$Z_{crit} = -\ln (K_{d1}/K_{d2}) / (K_{d1} - K_{d2}) \quad (18)$$

A changing heating rate profile induces a forcing of the upper layer and out of the surface. The exacerbated thermal flux “trapped” nearer to the surface is equivalent to the area between the two RHR profiles, integrated between the surface and the crossing depth (Z critical). It is the same flux that otherwise would have been transmitted in depth (the area between the curves below Z critical). It is the difference between the integral of the two curves. It also corresponds to the difference between the two irradiance decay profiles at depth Z_{crit} : I_1-I_2 . Note that a small Z_{crit} mostly indicates that there was a big difference between K_{d1} and K_{d2} . Hence, it is expected to correlate inversely with the other variables.

$$\begin{aligned}\text{Forcing} &= (I_1 - I_2) = \sum_0^z (RHR1 - RHR2) * \rho C_p && (19) \\ &= \int_0^z (dT1/dt - dT2/dt) * \rho C_p\end{aligned}$$

CHAPTER 4 Results

SST Trend

Figure 15 maps the mean monthly SST trend of ocean at 1m depth from 1987 to 2017 based on the OAFlux dataset (% per annum with 1998 as baseyear). It is used as a base climatology to be compared with a similar existent climatology (Figure 4) for method and result validation. It indicates the general location of heat accumulation that has occurred over the last 30 years.

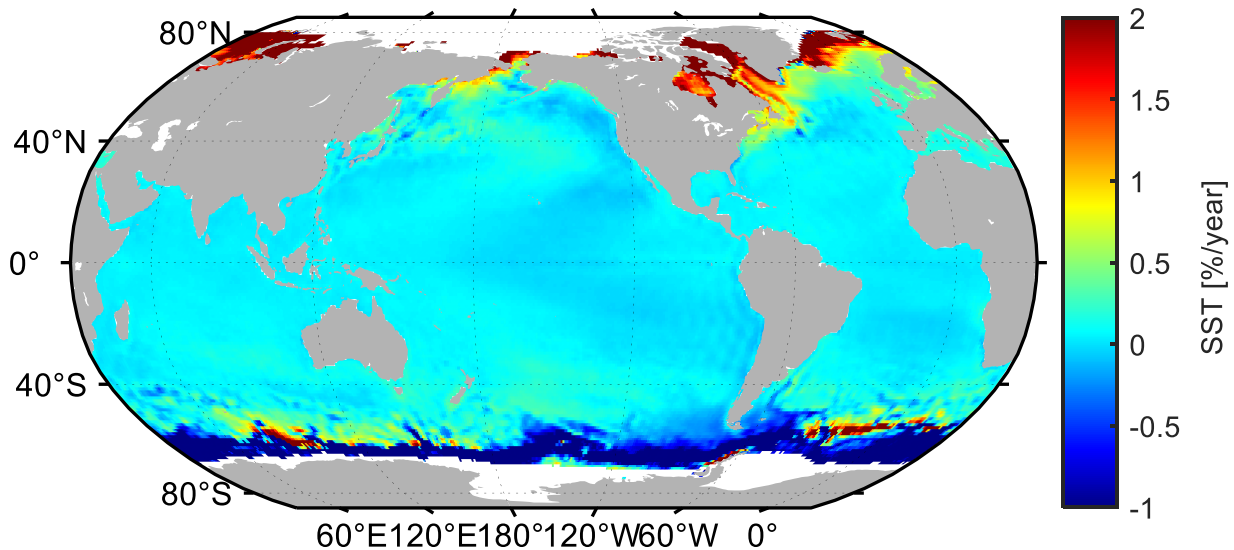


Figure 15 - SST trend [% / yr] from 1987 to 2017

Each of the 180 x 360 pixels map (hence 64 800 bins), statistically computes 360 months worth of averaged SST from 1987 to 2017. The global mean SST increases of 0,086%/yr from 1987 to 2017 for the entire surface. Noteworthy positive trends are apparent in the Bering Sea in North Pacific, in the Arctic, in the Baffin and Hudson Bay in North Atlantic and along the regions of the Patagonian Shelf in western South Atlantic. There are also significant positive trends in inland and coastal waters. The distribution of SST trend and those of GHRSSST's Figure 4 are similar.

DSST Trend

DSST is the difference between the daily daytime and nighttime SST (Bernie et al. 2007). Figure 16 maps the evolution of this difference over a 9-year period, from 2002 to 2011 during an AMSRE satellite mission. It locates places where the diurnal SST amplitude has changed during this period. DSST was assessed in the hope of revealing an additional information regarding the relationship between SST and K_d .

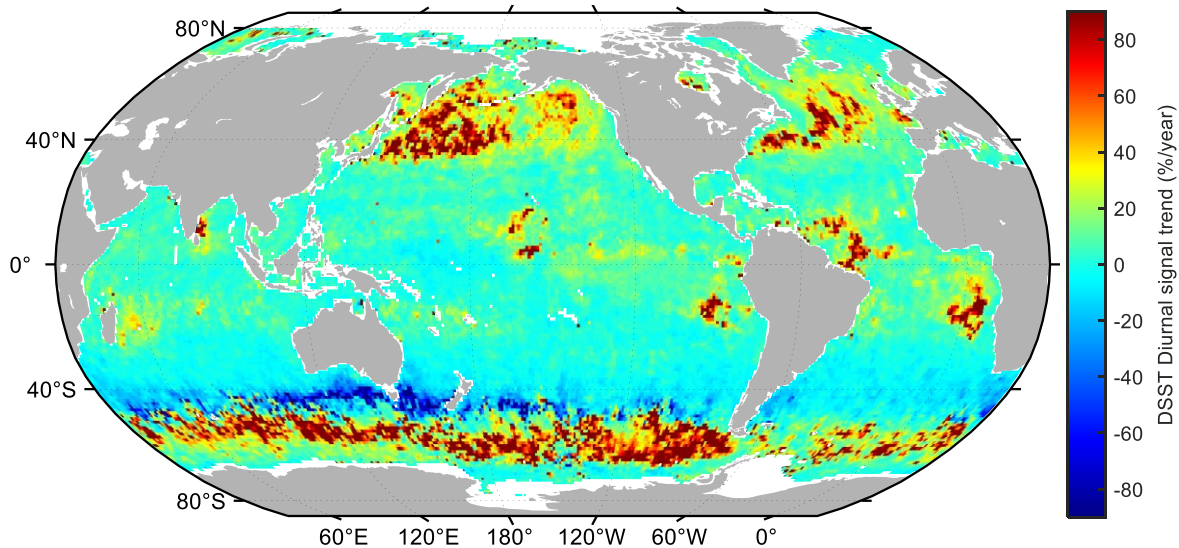


Figure 16 - DSST trend [% / yr] from 2002 to 2011

The original 720 x 1440 gridded map statistically computing 108 monthly averaged DSST has been rescaled to a 180 x 360 gridded map. The global mean DSST increased 5 % from 2002 to 2011 for the entire surface. Noteworthy positive trends are apparent in the entire North Pacific, North Atlantic, Indian Oceans and along the Antarctic. There are also significant positive trends in inland and coastal waters. There is a negative trend band that crosses the whole southern oceans, between 30° and 50° latitudes, as well as a decrease DSST in the “tropical warm pool”.

Kd490 Trend

The K_d trend in the 490 nm wavelength is mapped in Figure 17 for a 18-year period, from 1998 to 2016.

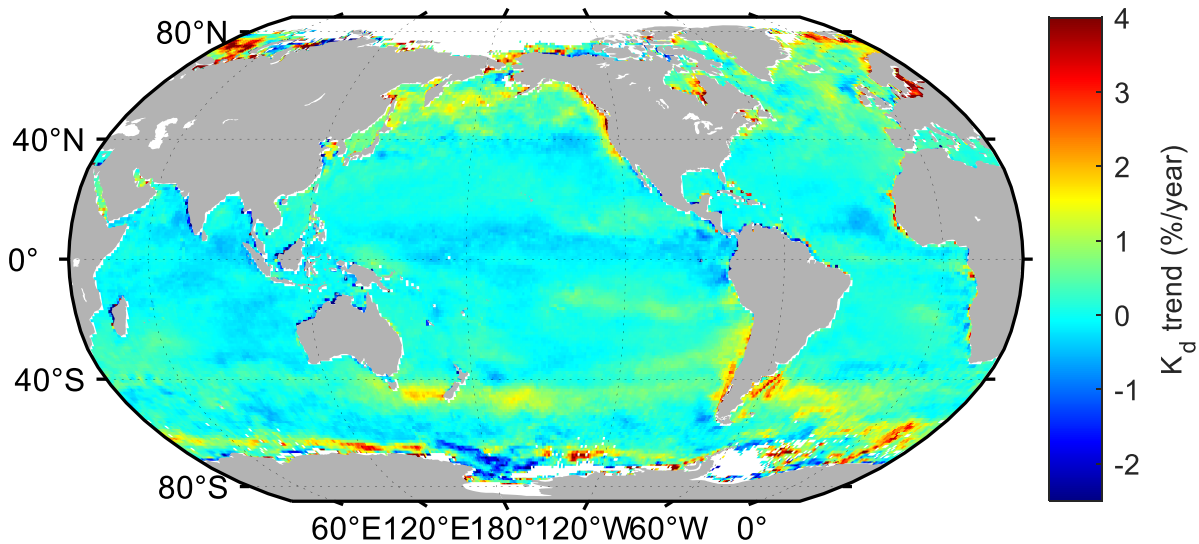


Figure 17 - Attenuation coefficient K_d trend from 1998 to 2016

Each 64 800 bin of the 180 x 360-degree gridded map statistically computes 216 monthly averaged K_d from 1998 to 2016. The mean K_d increased of 1% globally from 1998 to 2016 for the entire surface. Similar noteworthy positive trends shown in the SST trend graph are apparent: In the Bering Sea of North Pacific, in the Arctic, in the Baffin and Hudson Bay of North Atlantic and along the regions of the Patagonian Shelf of western South Atlantic. There are also significant positive trends in inland and coastal waters. There is a negative blue zone near the Antarctic region which could be attributed, for example, to dilution following ice melt.

Results Summary

Table 5 reunites the principal conditions describing the globally averaged initial and final state of SST, K_d and DSST over time. It also indicates the mean extracted absolute and relative trend of the 3 variables. It includes the final globally averaged values of K_d (Figure 17), Z_{crit} (Figure 19) and the forcing (Figure 20). The overall forcing of 0.33 W/m^2 is an annual average over the entire Earth surface considering the ratio ocean/land of 0.75. The value for the whole 18-yr analysis period and for the entire surface is 5.9 W/m^2 .

Table 5 - Summary of Global mean values of trend for the five main variables

Variable	SST [°C]	K_d [m^{-1}]	DSST [°C]	Z_{crit} [m]	F [Wm^{-2}]
Global Mean Initial Value	15.206	0.062	0.185	-	-
Global Mean Trend	0.013	0.001	0.009	-	-
Global Trend in % of initial value	0.086	1.055	5.095	-	-
Global Mean Final Value		0.076		14.809	0.330

Figure 18 shows the resulting irradiances and radiant heating rate decay curves for two different globally averaged input K_{d1} and K_{d2} . Each color represents the situation of the time. The blue curves are associated with a globally averaged K_d of the base year 1998, while the red curves are obtained using the most recent K_d for the year 2017. These curves illustrate the fate of the mean incoming solar radiation of 122 W/m^2 reaching the surface (as represented in Figure 13 by the black surface and in equations (15), (16), (17), (18), and (19)) when they are subjected to different attenuations. Note that both mean forcing estimates in upper and lower panel are very similar, despite the different approach to calculate it. Figure 18 shows the result along the depth for averaged inputs. However, when considered individually, each bin of the map possesses its own forcing calculated from unique K_d , I_0 , Z_{crit} , I_1 , I_2 , RHR_1 and RHR_2 . Figure 20 maps the resulting forcing.

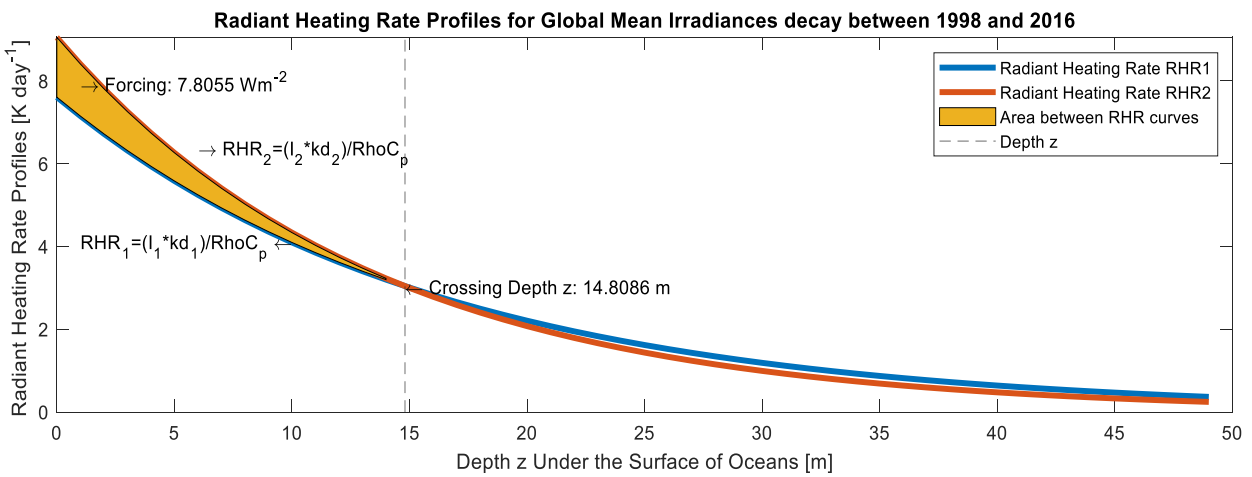
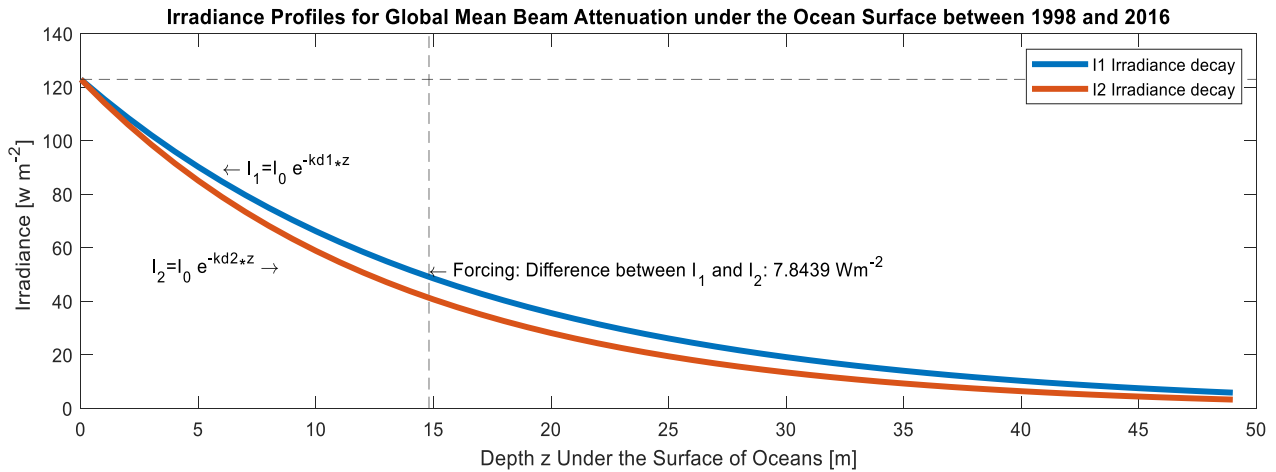


Figure 18 – Upper panel: Irradiance decay profiles I_1 (blue, 1998 average) and I_2 (red, 2017 average) along the depth z , for an average incoming irradiance (I_0) and averaged attenuation coefficients K_{d1} and K_{d2} . Lower panel: Radiant heating rate profiles RHR_1 (blue) and RHR_2 along the depth z for I_1 and I_2 , and K_{d1} and K_{d2} respectively. The overall forcing is the area (orange) delimited by RHR_1 , RHR_2 , $z=0$ and $z=Z_{crit}$ and is also equivalent to upper panel I_1 and I_2 difference.

The detection of the critical depth Z_{crit} is an indicator of the intensity of the radiant heating rate changes that occurred over time. It also indicates the distance from the surface where this change occurred. In Figure 19, the red zones of deep Z_{crit} are an indicator of the similitude between the two RHR curves their low steepness made it long until they finally cross. On the opposite, the blue zones of shallow Z_{crit} indicate an important change.

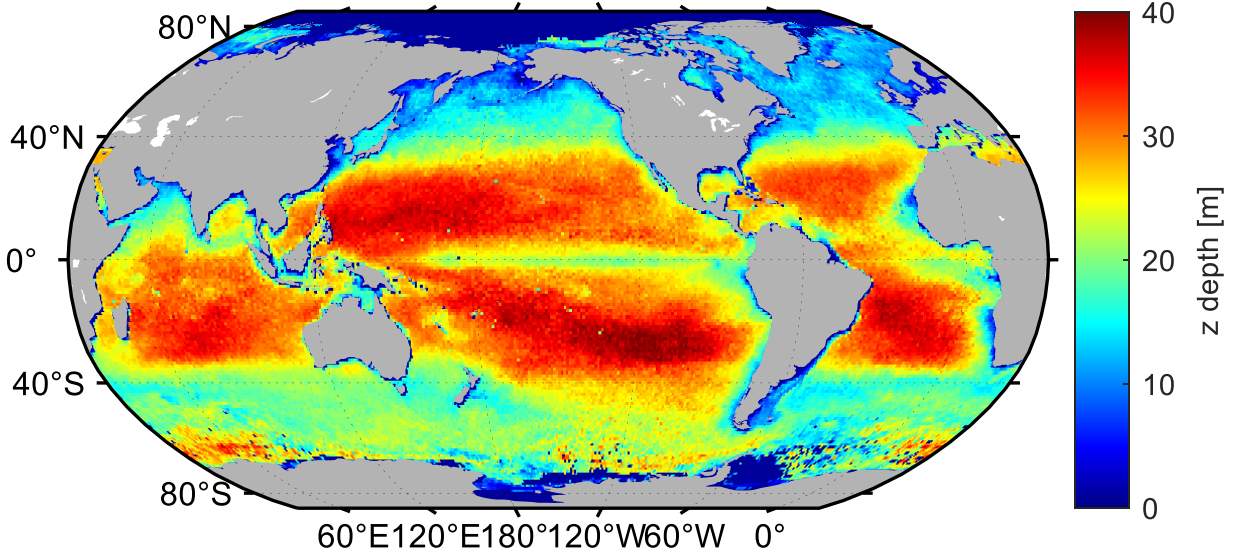


Figure 19 - Critical depth Z_{crit} associated with the RHR_1 and RHR_2 curves crossing.

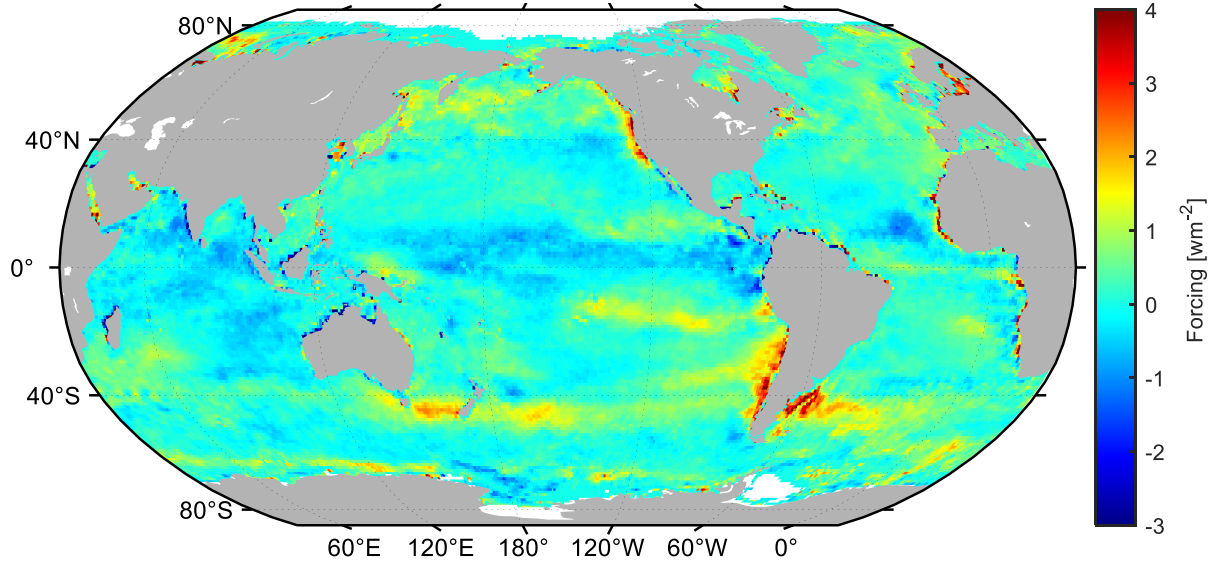


Figure 20 - Yearly forcing (W/m^2) on air-sea heat flux associated with K_a trend and incoming irradiance I_0 .

Correlation

Table 6 - Correlation Coefficients between five 10° x 10° map size datasets

Variable	SST [°C]	DSST [°C]	Kd [m ⁻¹]	z [m]	F [Wm ⁻²]
SST	1.00				
DSST	0.04	1.00			
Kd	0.38	0.07	1.00		
z (-)	-0.42	-0.12	-0.29	1.00	
F	0.06	0.06	0.15	-0.11	1.00

What emerges from the correlation table is the overall weakness of correlation between paired variables. All falling under the threshold of $R=0.5$ for a fair connection, the absolute values range from 0.04 to 0.42. Some pairs were expected to have a good correlation but finally are surprisingly low, considering the dependency existing in the way they were extracted. For example, the weak $R = -0.29$ describing the opposed behavior of depth z according to the attenuation trend Kd was expected to be stronger since z is calculated using initial attenuation values and attenuation trend values of Kd . On the other hand, it is satisfying to observe the strongest links between SST / z and SST / Kd of -0.42 and 0.38, respectively. The first connection translates to an upward shift of SST whenever depth z becomes smaller, as predicted by the theoretical framework. The second correlation of 0.38 between the two main variables of the thesis for which a connection was expected, is weak but does exist.

CHAPTER 5 Discussion

Anthropogenic K_d trend

The positive K_d trend seen in Figure 17 is a consequence of natural and anthropogenic changes of the input of optically responsive aquatic components. The next section lists by examples some phenomenon that would explain these significant changes on a planetary scale.

Bukata et al. (1995) lists the natural sources of organic and inorganic suspended components (sestons) ranging from plankton, detritus, volcanic ash particles and in situ chemical reactions to terrigenous suspended particles originating from river discharge, shore erosion and atmospheric transport followed by dry deposition.

The presence of terrigenous suspended materials into tributaries has potentially increased as a consequence of anthropogenically driven erosion. In wave height studies, the increased erosion effect is well known. Morim et al. (2019) estimates at 5-15% in robust changes in annual mean significant wave height. They report that 50% of the world's coastlines are at risk from wave climate change. During a Bureau of Meteorology conference which I attended during my internship in Melbourne, my abroad supervisor Prof. Alexander Babanin also linked this phenomenon to the ice melting rate²⁶. He gave the Alaskan shores as an example of accelerated erosion, where ice sheet covers previously protected the fragile earth beneath it. Now that it is being uncovered, the shores erode even more easily, conveying large amounts of terrigenous matter into coastal waters. This has the effect of altering (increasing) the readings of K_d .

The deforestation caused by agricultural land gain is another example of important land use change. It simultaneously increases the runoff sediments' loads and also injects nutrients associated with fertilizing activities. Simionato et al. (2003) reports a doubled nitrogen, phosphorus, and total organic carbon in global river discharges during the past two centuries.

²⁶ The observed rate of melting ice of 380 km³ yr⁻¹ is an indicator of irregular and unexpected heat redistribution in the cryogenic cycle [4]

Amazon and Orinoco rivers, together forming the biggest river system in term of discharge (0.2 Sv), alter the coastal freshwater balance.

The chemistry of water is clearly affected by human, intentionally at times: The Iron Fertilization pilot experiment conducted in 2012 by a British Columbia fishing company is an example of a controversial geoengineering event (Strong et al. 2009). With the goal of restoring the salmon population growth via a plankton bloom, they purposely poured 120 tonnes of iron fertilizers in 300 km² of coastal water. The mimic of a volcanic eruption was also potentially removing carbon dioxide from the atmosphere. We argue that they failed to consider an enhanced irradiance surface absorption in their experiment altogether. The mechanisms of ocean sequestration of CO₂ to mitigate the climate are not yet well understood (Simionato et al. 2003). To help visualize, the heating rate associated with a shallower absorption of SW radiation within a turbid coastal water is well depicted in Figure 21. Note how the highest values of the forcing mapped in Figure 20 corresponds mainly to coastal waters and big river plumes.

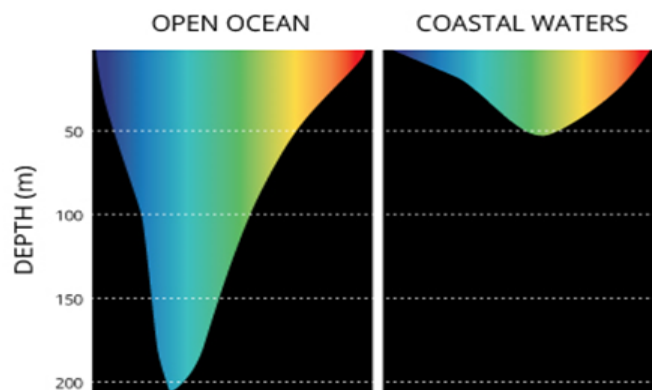


Figure 21 - Comparison of light penetration through open vs coastal waters in visible waveband. Image courtesy: Kyle Carothers, NOAA-OE

The anthropogenic causes above do not mention the impact of atmospheric soot deposition. Atmospheric born pollution on water surfaces has possibly been enhanced with human activity. For example, the Black Carbon (BC) emissions and propagation increased because of coal combustion and fire events (Bond et al. 2013). Some studies use the Atmospheric Optical Depth (AOD) index to describe the effect of atmospheric born pollution on the surface temperatures. For

example, Bogdanoff et al. (2015) finds that dust AOD of 0.1 would correspond to an SST error of 0.5 ° C.

Black Carbon

IPCC experts include the effect of Black Carbon aerosol (BC, or soot) in the computation of radiative forcing. IPCC's Figure 2 from Chapter I showed a non-negligible 0.64 W / m² contribution of the BC on the overall atmospheric forcing. In their detailed study of the role of BC on climate, Bond et al. (2013) explain how the effect of BC on Radiative Forcing (RF) is estimated when it comes to its emissions and deposition on snow only. Figure 22 summarizes the primary considered sources of BC, its absorptive capacity for solar radiation (at least 5 m²g⁻¹ at 550 nm) as well as its influence on the albedo of clouds and the ice / snow cover. Figure 23 maps these effects on surface temperatures for different simulations. Note how high temperature changes due to BC in Figure 23 occurs mostly in the Northern Hemisphere, in a similar manner to the K_d trend mapped in Figure 17.

In their report, the BC contribution to forcing is considered only regarding its aerosol and ice/snow influence. Once deposited in the oceans, would the water-mixed BC contribution to the irradiance absorption be significant? As they explained, BC is removed quickly from the atmosphere and is deposited. It does not however disappear.

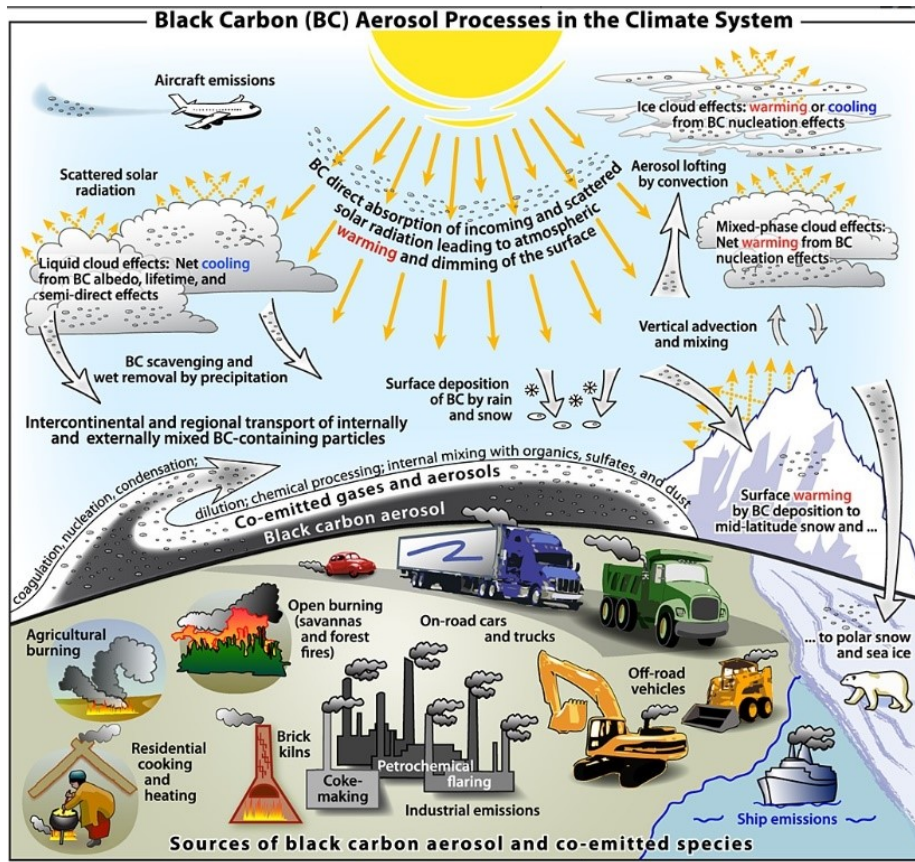


Figure 22 - Schematic overview of BC sources and processes. Shows the community efforts to consider its effect on radiative forcing once in atmosphere and deposited on snow. Does not show the role BC has once deposited into water (Bond et al. 2013).

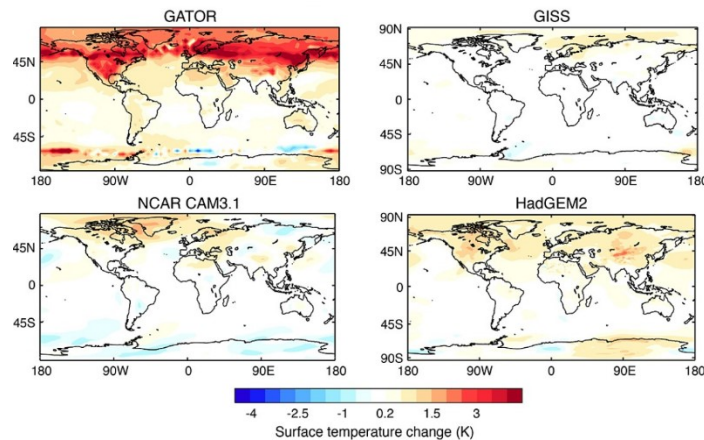


Figure 23 - Differences between different climate models when assessing the Surface Temperature changes due to BC forcing. Note that the forcing occurs mostly in higher latitudes (Bond et al. 2013).

The overall BC inventory used by Bond et al. (2013) and the IPCC to estimate its forcing is uncertain. In Dong et al. (2019), they used an updated and multisource inventory of atmospheric BC to estimate its direct forcing. When compared to IPCC's, modeled BC forcing is 30% increased globally. More astonishingly, the BC updated inventory is 3 times greater than previous estimations in the Arctic (60-90°N) and its direct forcing for this region is 2 time greater, especially over Eurasia. This not so surprising result is of primary importance for the interpretation of our results: A noticeable portion of our K_d trend in Figure 17 is located precisely at this region. Also, we find that these results correlate very well to those of Chang and Dickey (2004), who mentioned a 30% heating increase in the Arctic top 10 m due to the changed optical properties. The correlation will have to be evaluated in a future study, but the comparison between the geographic distribution of BC and our K_d trend is compelling.

However, like in Levitus et al. (2005), a decrease of incoming solar irradiance reaching the surface due to higher aerosol absorption could be expected. The hypothesis states that the altered color of the water will increase its heating rate closer to the surface and its temperature. Greater soot deposition in arctic regions could potentially color its water. On the other hand, the concentration of BC in the above atmosphere could offset this forcing to air-sea interface by attenuating part of the Irradiance on its pathway. Sometimes, the semi-translucent or opaque atmospheric condition around an SST remote sensing measurement will exclude it from the dataset, despite the atmospheric-correction algorithms to treat individual non-clear-sky water pixels (Sathyendranath et al. 2019). This filter may enhance a dataset that systematically excludes the occurrences of strong depositions. This type of error source against SST retrieval is described as non-trivial contamination of the dataset by Bogdanoff et al. (2015).

Radiant Heating Rates (RHR)

Correlation

The effect of different meteorological factors on the sea surface temperature has been investigated. Their mutual (bilateral) influences were tested. The table 6 shows the correlation coefficients between all 5 variables. Similar to the resulting correlation maps in Zhang et al. (2019), our results are mostly mild, ranging from -0.42 to 0.38. Theirs are between -0.5 and 0.5. They also are motivated to conduct a further regional analysis. However, unlike their gridded analysis, a global correlation of the trends' amplitude and sign was conducted. This methodology is very restrictive regarding the interpretation. A moderate dependency of SST trend on K_d trend is identified. It's important to specify that this dependency does not indicate the causation. For example, the similar coastal tendency of SST and K_d could be attributed to the simple increased presence of cooling systems of industries, which plays a role in the heating of coastal SST. Their relatively dependency could be coincidental.

Offsets

The methodology is allegedly insufficient to detect any reliable relationship between the temperature of the water and its color. The literature pointed toward an existing relationship, but the interconnection to other drivers cannot be overlooked, and hence the necessity to use adequate OAGCMs in a future study.

One needs to be aware of the offset effect which hampers the radiative forcing of each isolated phenomenon. As mentioned in the approach, the amount of heat being accumulated near the surface is potentially removed right away by attenuating factors acting to bring back equilibrium. The earth is a connected place. Like the hurricane denied the needed energy to subsequent storms to sustain themselves, the winds fed by evaporation increased by a warmer upper layer induces a deeper mixing, self-regulating the temperature swings, smothering any drivers' direct influence. Also, the continuous transport of water masses hinders any detection of SST rise, that would be otherwise enhanced under stillness scenarios. At least half the SST

warming anomalies are associated with oscillations of a climate Mode of Variability²⁷ (Palmer et al. 2009). Kiehl and Trenberth (1997) also remind that the heat being accumulated are sometimes masked and could be even more important if their response to other external forcing remained unaltered. In their study, they therefore mention the role of the low sunspot activity period, atmospheric aerosol and stratospheric vapor, and ENSO on their OHC trends results. The detection of a relationship is affected.

Relationship through timeseries

The bilateral relationship may however be detected from different approaches. The local scale analysis by time series analysis from 1997 to 2016 of Groom et al. (2019) suggests in Figure 24 A) that chlorophyll-a concentration and the ENSO mode of variability evolve conjointly. Their ENSO index and Chl-a data were taken from NOAA and OC-CCI websites respectively (Von Schuckmann et al., 2016) as cited in Groom et al. (2019). An analogous relationship could be uncovered, considering that their monthly ENSO Index is directly related to our SST and their chlorophyll to our K_d . The OC-CCI dataset for this study and our thesis are virtually the same, and the limits associated with its use will be detailed later.

²⁷ A Mode of Variability is a climate pattern with oscillatory behavior. El Niño–Southern Oscillation (ENSO) is an example. Periodic variation in winds and sea surface temperatures over the tropical eastern Pacific Ocean, affecting the climate. (*ENSO Wrap-Up Current State of the Pacific and Indian Oceans*, 2020)

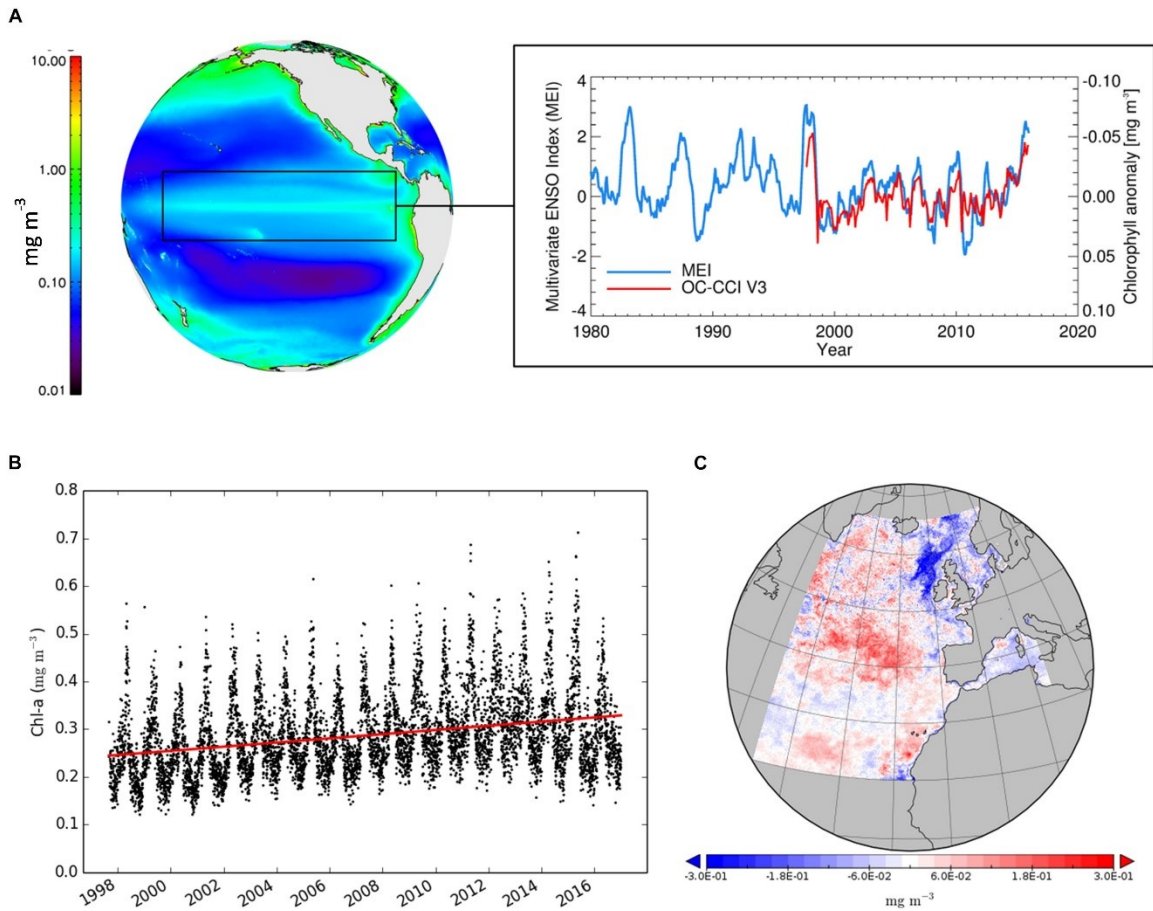


Figure 24 – A) NOAA monthly ENSO Index time series progression is similar to Chl-a B) OC-CCI chlorophyll concentration time series for the same period, indicating a positive trend (Groom et al. 2019).

Empirical K_d has recently been accounted for in a OHC study. As mentioned in the literature review, Mallick et al.(2019) compared in 2015 a « control run » using a constant K_d (23m) in the upper layers of the Bay of Bengal, to an experimental run using a spatially varying K_d . They quantified the differences of temperature it causes (see Figure 25). The result is an upward shift of the MLD by 5 to 20 meters and an improvement of modeled SST and OHC by more than 10 to 15 % (Mallick et al.2019).

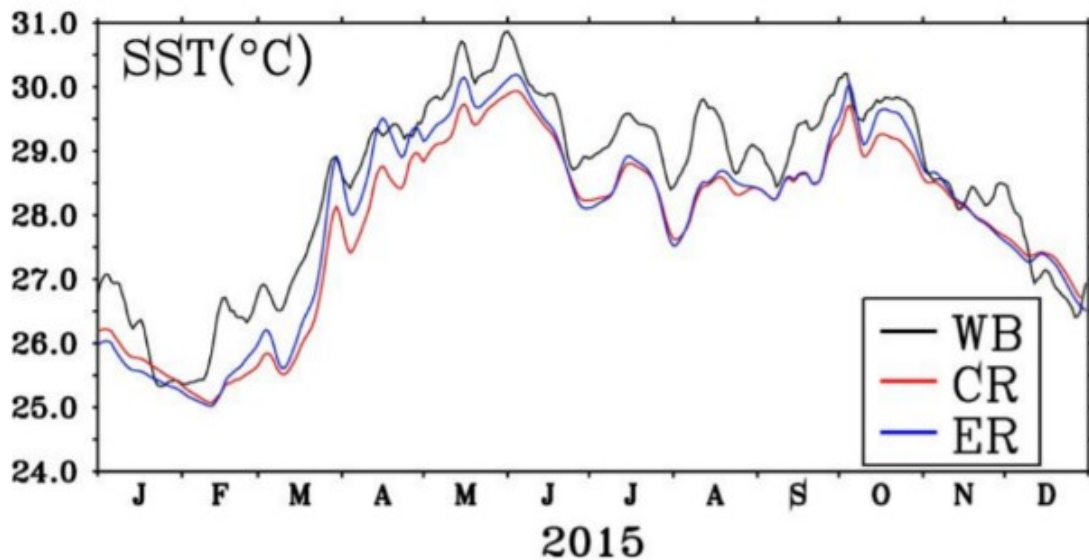


Figure 25 - Comparison of the three simulations runs for SST 2015 timeseries in the Bay of Bengal region (Mallick et al. 2019).

Figure 26 shows the seasonal spatial distributions of differences between a fixed attenuation depth of 23m used in most typical models (control run in this case) and a real measured attenuation depth associated with K_{d490} measurements (Z reciprocal). This image conveys the significant variation of transparency within a year. The differences near the coast, close to -15 m, indicates more turbid waters. The judicious use of an empirical K_d rather than an average (as proposed in Jerlovs' water types) has the potential to produce more accurate temperatures and fluxes simulations and predictions. Their results also suggest that calm winds and high solar insolation has a great influence on measurements. Their high K_{d490} negative differences were reportedly caused by sediment deposition from continental rivers and their tributaries as well as coastal geomorphological processes. Figure 26 highlights a typical gap and indicates the path of progress for regional budget resolution.

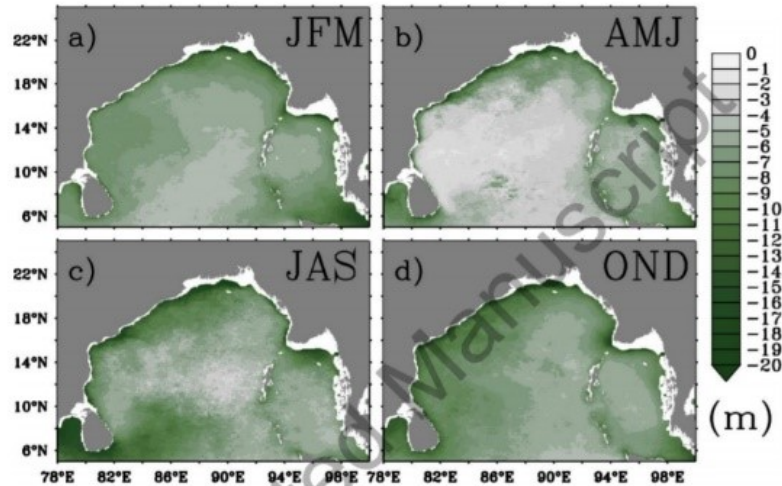


Figure 26 - Difference between K_d490 and the constant value of 23 m, used in the control run (CR), for the year 2015 in the Bay of Bengal region. Negative differences indicate shallower penetration of shortwave radiation in the ER while the penetration is deeper if differences are positive (Mallick et al. 2019).

Much like Groom et al. (2019) and Mallick et al.(2019), He et al. (2017) used SST timeseries to link the climate variations to SDD^{28} (Secchi Disk Depth). In Figure 27, this transparency index, directly proportional to K_d , seems to follow the variations of SST. This time, however, the successive peaks of the two variables allow to guess that SDD leads SST or inversely, as it is unclear if the peaks are opposed or staggered. The overall trends are progressing in the same direction. According to He et al. (2017), the variation in transparency is still poorly understood. They underline that the penetration and absorption of solar irradiance in deeper water may be part of the 2000-2010 known hiatus of Earth's SST. Since they retrieved SDD from the same SEAWIFS dataset used to generate our K_d dataset, the later timeseries before 2015 is like He et al. (2017) SDD timeseries.

²⁸ Rather simple to use in situ instrument. The Secchi Disk is a black and white 20cm diameter disk that is lowered in depth until it is no longer visible. This measure is the SDD and gives the water body transparency.

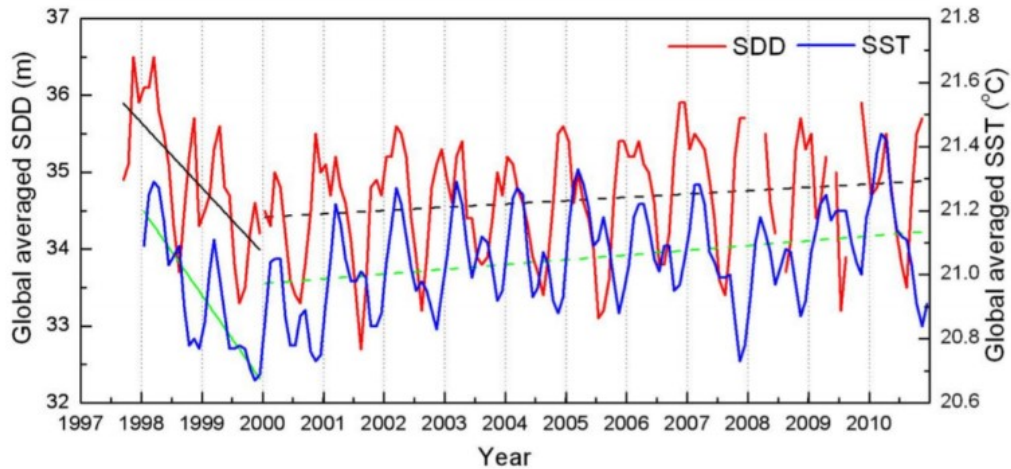


Figure 27 – SDD and SST global averaged time series. Their overall regression is evolving in the same direction (He et al. 2017).

He et al. (2017) mention throughout their interpretation that there is a match between the three panels of Figure 28, except for coastal and polar regions. It would be relevant to verify if the ice melting rate contributes to the cooling offset of the warming in those regions. They explain the sudden drop of SST in Figure 27 between 1997 and 2000 with El Nino event. They argue cooler SST led to higher chlorophyll concentration and vice-versa, hence the matching patterns in Figure 28. They also point that the SDD has strong seasonal variation.

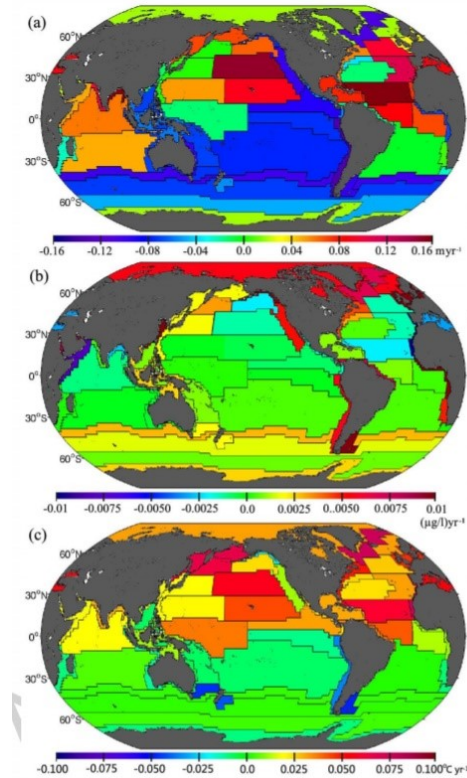


Figure 28 – (a) SDD trend, (b) Chlorophyll trend and (c) SST trend, from 1998 to 2010, by biogeographic province (He et al. 2017) .

RHR Shifts at depth Z_{crit}

As surprisingly shown in Figure 29, for the same period we assessed our trends, their mapped mean SDD is virtually the same as our mapped z critical of Figure 19. To retrieve their SDD values, they used the same K_d dataset as was used here in this thesis (OC-CCI), but with an empirically determined inverse relationship. Like Z_{crit} estimation but through a different path, they retrieved SDD using values of absorptivity, backscattering, and remote sensing reflectance. The use of the exact same dataset based on the same semi-analytic QAA algorithm (Lee 2005) to compute IOP leads to this major fit.

However, SDD and Z_{crit} are not supposed to represent the same physical phenomenon. The subtle distinction resides in the meaning of the value. While SDD is supposed to represent a depth of full attenuation, Z_{crit} is the depth at which the final RHR ceases to be higher than the initial

RHR, and starts to get lower below, as explained with equation (18). It was calculated using the ratio of K_d increment and initial value. It is the simplification of the equality in equation (17). Hence, we suspect their algorithm to retrieve this “theoretical” SDD to be comparable to our ratio. Also, their analysis is chlorophyll oriented and omits considering other inputs affecting K_d and transparency such as pollution, which may explain the slight differences in the scale.

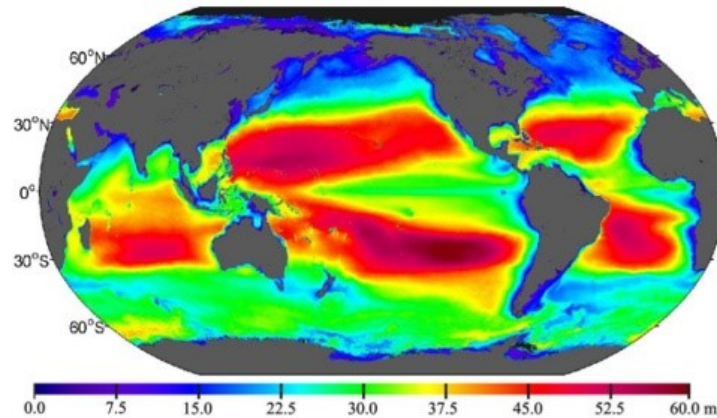


Figure 29 - Distribution of a theoretical SDD annual mean (He et al. 2017). Virtually the same result when compared to our mapped Z_{crit} of Figure 19.

Z_{crit} is the weighted difference between K_d initial and K_d final. As stipulated in methodology, when the shift of RHR curves occurs around the Z critical (shadowed area between RHR curves of Figure 18), it translates to an enhanced energy loss to the atmosphere. Also, it indicates the steepness of the difference between both RHR curves. For example, a shallow (small) Z_{crit} such as seen in polar regions, is the signal of a highly impacted changed solar penetration. It is more impressive to note the contribution of W/m^2 at the poles (higher latitudes) of Z_{crit} , considering the weak incoming radiation which disadvantages higher latitudes’ weight on the forcing in Figure 20. This represents a new information given through Z_{crit} . This critical depth could be recognized and used, such as did He et al. (2017) with their SDD. The forcing at stake here still needs to be introduced into an appropriate OAGCM to calculate its effect on air-sea fluxes, considering the other radiative and turbulent fluxes.

The impact of the use of a difference of attenuation depth (K_d reciprocal) through time was explored in 2016 in the Arctic ocean. Kim et al. (2016) thoroughly linked the ice melting rate with

the CDOM concentration, the mixing, the cloud cover, and associated heating. They modeled an additional CDOM layer in Arctic oceans and observed different heating by penetrating shortwave radiation changes, mixing, and surface heat fluxes in the upper 100 m. They remind how the variable is still NOT included in most GCM despite increasing evidence of its heating influence. Their results in Figure 30 show the increasing shortwave heating and associated temperature difference for the first 10m (a and c), and the withdrawal it causes deeper (b and d). This complete example of a pertinent usage of K_d to retrieve and assess impacts on the RHR fits our approach. In comparison, our intention was to highlight the impact on a global scale and consider the attenuation coefficient change over time. In addition, using Z_{crit} to geographically localize the RHR differences, and integrating over depth, we produced an estimation of the equivalent forcing on the air-sea interactions in W/m^2 .

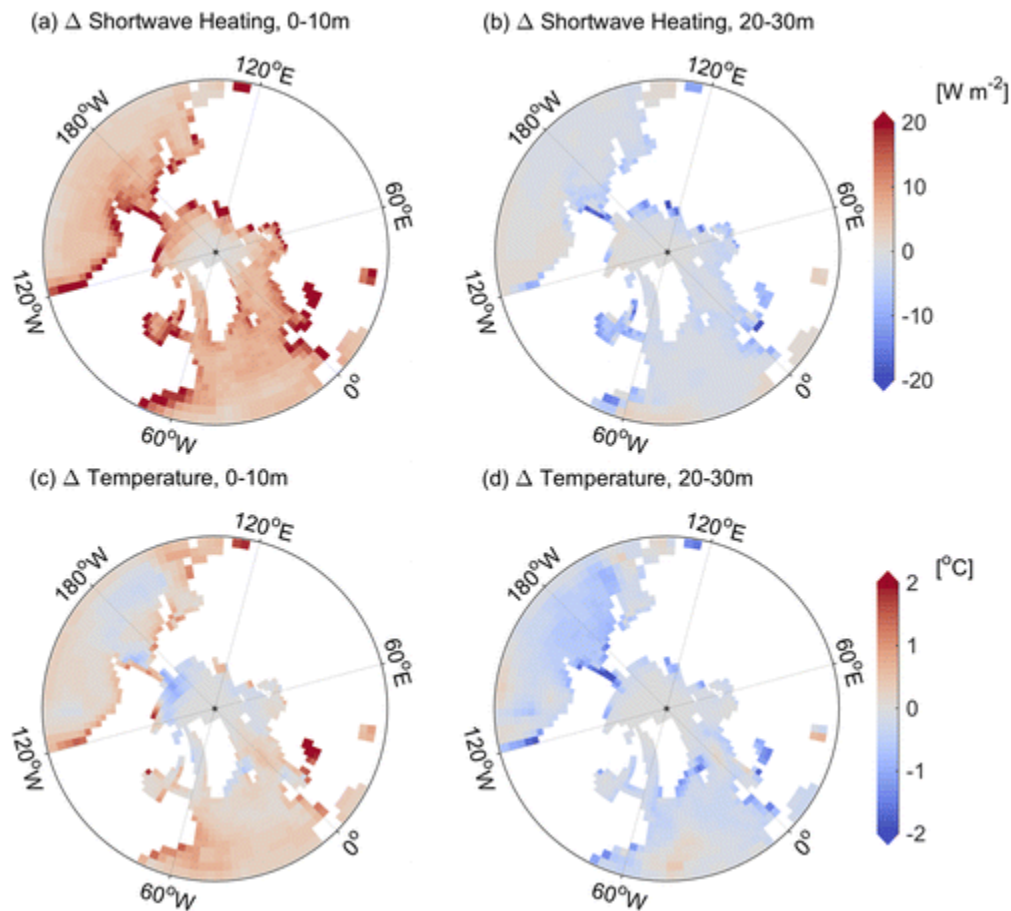


Figure 30 - Difference of RHR and temperature for the inclusion of color detrital matter into model runs a) RHR for z of 0 to 10 m b) RHR for z of 20 to 30 m and c), d) Temperature differences for upper and lower layers (Kim et al. 2016).

Forcing

In the coupled model involving the four key fluxes (SW, LW, LHQ, SHQ), the inclusion or not of a diurnal varying SST has the potential to alter significantly the resulting Q_{net} . Figure 31 shows this difference of Q_{net} , which can be called a Forcing. This Forcing on the atmosphere is then comparable with the GHG 3.1 Wm^{-2} forcing given in IPCC last assessment report (Stocker et al. 2013). Similarly, the estimation of a forcing of 0.33 Wm^{-2} due to K_d increasing trend fits into the order of magnitude such a climatic variable could have.

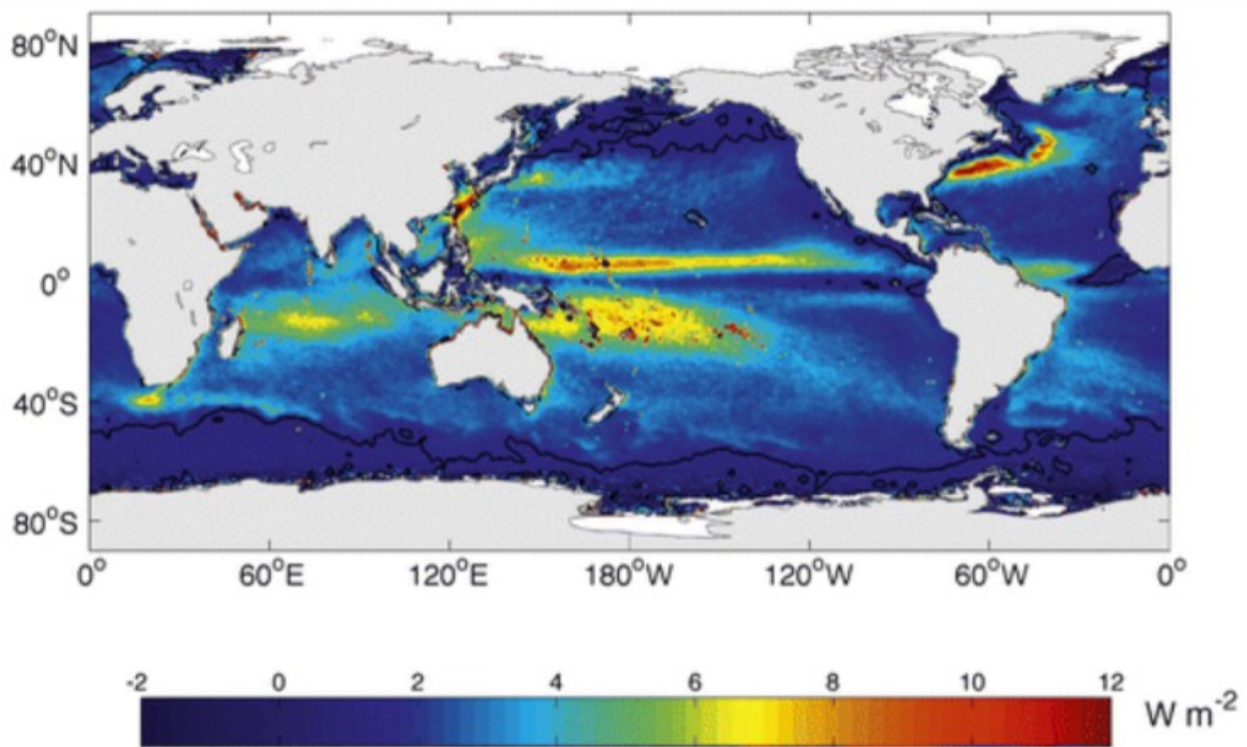


Figure 31 - Net flux difference when considering the SST diurnal signal for 10-yr. Contour line is at 0 Wm^{-2} . "The total global-average difference is 1.21 W m^{-2} . " (Clayson and Bogdanoff 2013)

Like those who sought the forcing induced by a more accurate Diurnal signal inclusion into the models (Figure 31), we established a theoretical forcing caused by the significant changed optical properties (Figure 20).

The main difference between Clayson and Bogdanoff (2013) study and ours is their adequate use of a model computing the feedback of the four main fluxes, including a diurnal signal. Our overall forcing of 5.9 Wm^{-2} for the whole 10-yr period DOES NOT consider any of the 4 other fluxes feedback. Since our result is not weighted in with all four fluxes within the budget, it is not possible to compare it yet with the diurnal forcing value in Figure 31 neither the forcing caused by GHG (Figure 2). The next logical step would be the inclusion of our attenuation signal into a model like what was used in Clayson and Bogdanoff (2013), integrating the radiative shortwave (SW), longwave (LW) and turbulent latent (LHQ), sensible (SHQ) fluxes' feedback to weight in our final forcing and compare it with other drivers. The value will likely be much smaller once weighted in a model. It would be relevant also to isolate the coastal areas and assess the forcing regionally.

Contribution to the Closure Problem

How would the inclusion of a “truer” K_d impact the global and regional distribution of the four main heat budget fluxes? The regional analysis of the heat budget (L'Ecuyer et al. 2015b); (Wild et al. 2017); (Pierce et al. 2006), by assimilating an improved SST layer, could potentially refine the agreement regarding the *closure problem* by weighing in the forcing calculated above. In its regional simulation of anthropogenic GHG forcing on the budget's heat fluxes, Pierce et al. (2006) focussed on the partitioning of the fluxes' variation inside different ocean basins separately. They used data from OAGCMs (Washington et al. 2000), as cited in Pierce (2006), to find the changes in heat flux component relative to preindustrial conditions. Their analysis did not however consider the anthropogenic alteration of SW absorption in water, neither did they include effects of black carbon in the runs of their atmospheric or oceanic simulation. Figure 32 shows the globally averaged distribution of the heat fluxes composing their budget over time. It shows that GHG has contributed to the increase of LW downward, warming the surface. The distinction between upward and downward LW indicates how the warmer ocean has also increased LW upward (LW_{surf} in the graph), which however does not totally compensate for the downward LW increase. This summarizes the concept of GHG forcing as we know it.

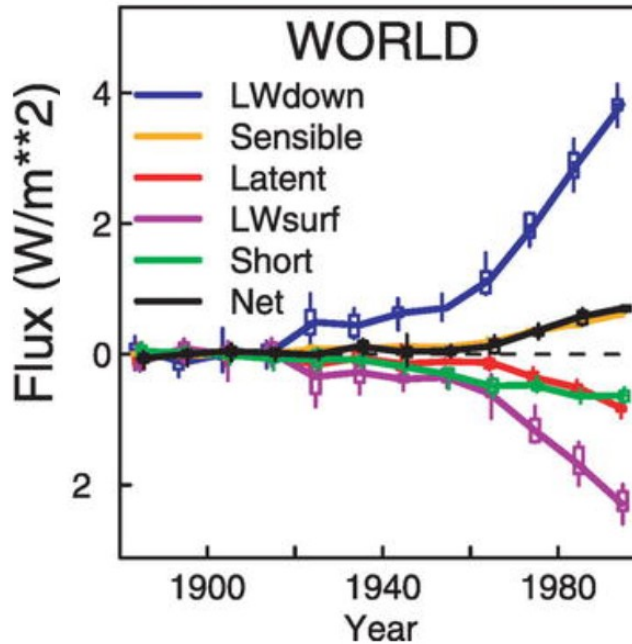


Figure 32 - Evolution of the fluxes composing the Earth heat budget over time (Pierce et al. 2006).

With the supposition that models are using a cold biased SST, it is suggested here that the inclusion of a K_d enhanced SST would contribute to the improvement of the predictions. For example, the inclusion of a warmer SST could reduce the difference between the Upward and Downward LW (net LW). Also, the inclusion of an appropriate K_d sublayer would improve the negative SW trend. Once those essential climatic variables are accounted, the regional analysis can be conducted.

Constraining the closure like did L'Ecuyer et al. (2015b) won't provide direct insight into the causes of bias. It won't scale exactly either because SST is dependent on latent heat of evaporation (Stocker et al. 2013). It is recommended though to improve the accuracy of estimated OHC so the future constrained simulations may rely on their mutual consistency.

In their study, Yu et al. (2007) suggests that the smaller continental landmasses of the Southern Hemisphere convey less cold, dry air masses than their Northern Hemispheric counterparts, hence the weaker wintertime flux intensification. Such an example of the importance of regional analysis encourages recommendation of a latitudinal analysis of our results.

DSST trend and the thesis question

Diurnal SST trends were compared to SST trends and K_d trends. The objective was to confirm the explanatory model of their interrelationship. A targeted climate phenomenon cannot be perfectly separated from all other effects occurring within a climate mode (Stocker et al. 2013). A shallow mixed layer affected by an increased turbidity is expected to get warmer, only if other climatic variations were not involved. Patterns of the wind, upwelling, precipitation, or evaporation may buffer the detection of SST variability caused by pollution. The use of a third climatic variable was sought to improve the odds and reliability for such a detection.

For polluted zones, increased absorption rate of solar radiation near the surface and enhanced stratification during the daytime was expected. Also, due to the emissive nature of its constituents, higher emission rate (heat loss) at the surface during nighttime compared to clear water areas was expected (Bogdanoff et al. 2017). For high winds, SST peaks were expected to be quickly dissipated through convection, thus not detected. In other words, the resulting areas of the map where DSST trend is positive were expected to match approximately the same patterns in the positive trended K_d areas.

Such a match did not occur. As witnessed from Figure 16 and Figure 17 comparison, the overall patterns of their trend do not seem to follow each other. Neither does the calculated correlation coefficient between both variables. Correlation coefficients of 0.07 and 0.04 between DSST and K_d , and DSST and SST respectively are very poor, hindering their interdependence from being recognized.

The fact that most users wish this DW signal to be removed may explain the early stage of quality for the DSST available products. The construction of the SST product typically avoids the inclusion of low wind and clear sky conditions inducing strong DW signal. Zhang et al. (2020) daytime retrievals are “contaminating” the product of the objective analysis. Bernie et al. (2007) acknowledge the DSST as a noise. The parametrization of the mixing caused by wind and waves “improves” the DSST signal, in the sense that it suppresses it (Mellor and Blumberg 2004). The removal of DW is often the main argument for the omission of IR sensors in remote sensing

products (Gentemann and Hilburn 2015); (Clayson and Bogdanoff 2013); (Gentemann et al. 2008). IR sensors measure the temperature of a very thin layer subjected to DW and wind mixing (Sathyendranath 2000). However, in this study, the dataset was purposely selected to monitor the DSST artefact. Further investigation with data producers REMSS on the production scheme are necessary.

Daytime cold bias

Another bias to elucidate regarding the DSST dataset resides in the discrepancy following the 2012 satellite instrument mission shift between the AMSRE and AMSR2. Figure 33 shows the difference (located mainly in the northern oceans) between the two sets of averaged data over their respective period (2002 to 2011 and 2012 to 2016). When assessing the average DSST for the most recent mission dataset AMSR2 (2012 to 2016), non-negligible zones of negative averages emerge. Figure 34 has a negative scale, to put the emphasis on the surprisingly large negative zones in the right panel (associated with averaged values of DSST from AMSR2 satellite mission between 2012 and 2016). As shown in this right panel of Figure 34, colder temperatures for these negative mean DSST during daytime than nighttime. The precedent mission AMSRE is exempt of such anomaly, as shown in the left panel of Figure 34.

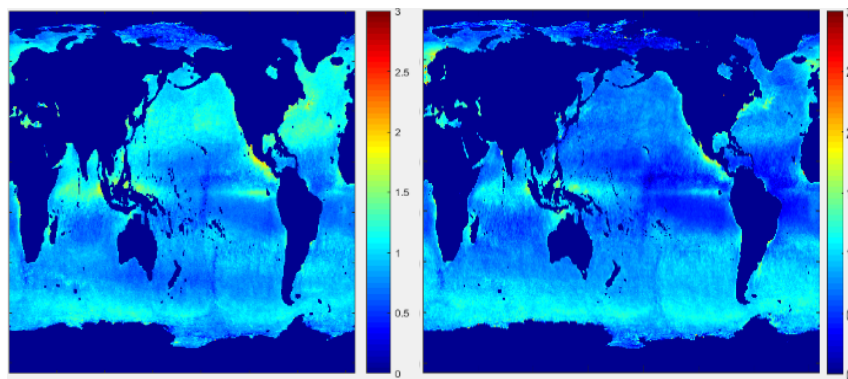


Figure 33 – Difference between DSST average dataset before (left, 2002 to 2011) and after (right, 2012 to 2016) the AMSRE mission shift to AMSR2.

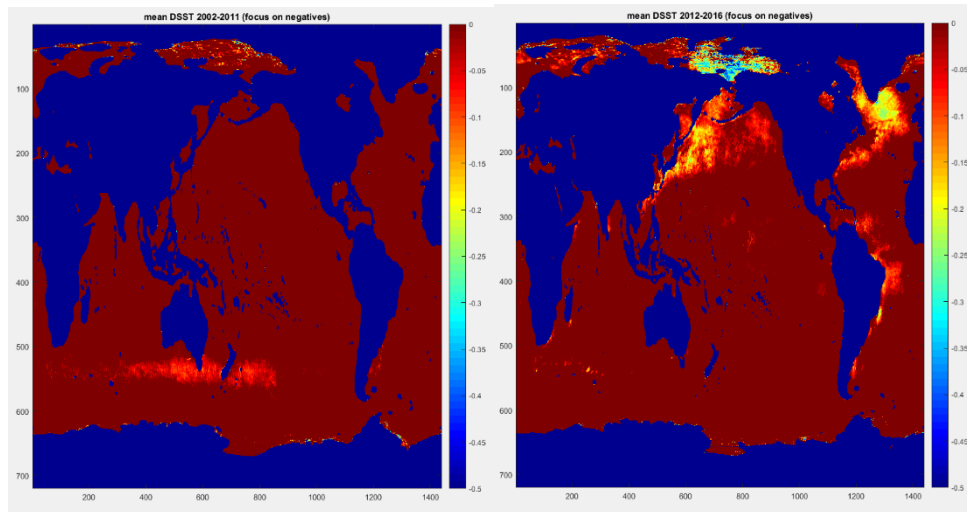


Figure 34 - Comparison on a negative scale only between the two averaged DSST missions AMSRE (2002 to 2011) and AMSR2 (2012 to 2016)

One of the possible explanation given by the producer for such an unexpected behavior of AMSR2 dataset is the daytime bias that is acknowledged cooler than the nighttime bias (Gentemann and Hilburn 2015). Such abrupt inter-annual artifact are difficult to explain by natural events (Raschke et al. 2012). It is recommended again in Zhang et al. (2020) to perform DSST parametrization based on more representative datasets. For that reason, the DSST time coverage in this thesis was limited to the AMSRE operations ranging from 2002 to 2011 inclusively.

Link between DSST, wave height and winds

DSST trend did not validate the interrelationship between SST and K_d . Instead, it revealed the importance of an improved DW sublayer from a different perspective. As pointed by Bogdanoff et al. (2017), the DW is important to air-sea coupling. The analysis of its link with high winds and wave mixing should be explored more. Meucci et al. (2020) sought the relationship between winds and wave heights. Likewise, it is relevant to acknowledge the role of DSST on winds and waves. The comparison of the resulting mapped trends is an indication toward their possible relationship (Figure 35). Areas of DSST enhanced stratification expectedly contribute to feed energy to potential storms, which in turns are linked to higher winds and waves.

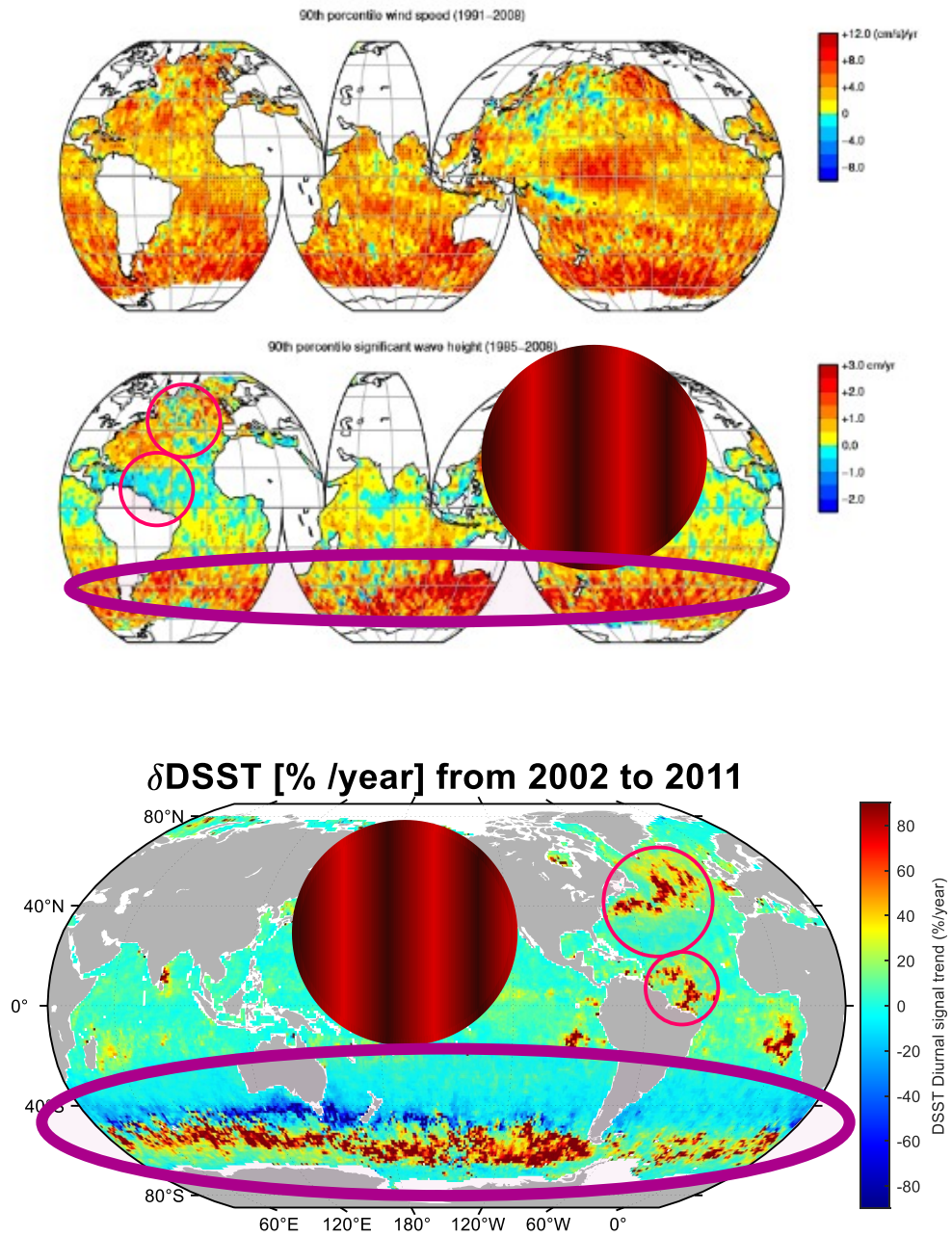


Figure 35 – Upper panel: Mapped trend of 90th percentile wind speed and wave height from 1991 to 2008 (Young et al. 2011a). Lower panel: Mapped resulting trend of 90th percentile DSST from 2002 to 2011.

Finally, to sort out previously mentioned bias, it would be relevant to verify separately the daytime SST trend and the nighttime SST trend and see which one is the cause for the negative averages of AMSR2. On cloud-covered days, the surface is mostly heated from IR back radiation, which is independent of turbidity. Hence, it is worth mentioning that the analysis should eventually consider low-wind and Clear Sky conditions, as was done by Schiller and Godfrey (2005). Lastly, as pointed by Sathyendranath (2000), ocean-color imagery is deemed better than infra-red imagery by many investigators to define the upper layer dynamics.

Limitation and recommendations

The research intended to gauge the global contribution of two main environmental variables (K_d , DSST) on the heat budget, by isolating their influence using seasonal trend detection, and comparing those trends with the SST trend. The above discussed results, however, would not yet be suitable for direct use in future work, as the scope of the analysis did not include the full examination of empirical statistics needed for significance. Instead, the study covered the description and explanation of a new path to be explored regarding sub grid drivers according to the literature. It focused on the establishment of an order of magnitude to detect the relevance of an empirically evidence but did not provide the uncertainties needed to conduct a reliable empirical estimation of the forcing.

The following section presents some usual quality control challenges that were encountered regarding the sampling and treatment of datasets. It is followed by recommendations to minimize their impacts in future work. All authors must work with what is known (limited) and what can be done about it (very limited), and hence the importance to acknowledge the confidence level of inputs and results to provide the best advice.

Data Sampling

To detect climate related trend, the sampling of climate variables would ideally be continuous over several decades for more than 40 years (Groom et al. 2019). However, remote sensing monitoring of climatic variables is rather recent. This restricts the validity of the analyses which are made despite the very short timespan of available data. To some extent, the climatic emergency forbids to wait for the accumulation of data, especially knowing the funding uncertainties reserved for such purpose in the future by space agencies (Antoine et al. 2005). Also, the limited lifetime (typically 10 years) of satellites and instruments greatly limits this essential continuity (Sathyendranath et al. 2019). A mission shift inevitably induces a discontinuity in the dataset which must be compensated for, but still leaves artefacts. This was the case within the K_d dataset. Its 2017 mission shift visibly resulted in a major drop in the mean values as shown in Figure 14. Hence, Figure 14 showed the glaring discontinuity between V3.0 and V4.2, the latter

adding the years 2018, 2019, 2020 to the timeseries of K_d . To avoid embarking on an overly in-depth analysis of the quality of the dataset produced, and after communications with the data producer (esa-oceancolour-cci.org), it was decided to limit the study to the data available before the shift, that is between 1998 and 2016 inclusively. A future study should be prepared to consider this discontinuity. Similarly, as was discussed in the diurnal signal section, the shift of satellite between 2011 and 2012 and the bias it generated forced the choice of a shorter but more reliable timespan for the analysis, thus limiting it to 2002 - 2011 rather than 2002 -2017. These limitations greatly affect the authenticity of the results presented.

The level of accuracy is always a major issue within the climatic research community. IPCC Recall in their latest (2013) 5th assessment that the accuracy associated with SST observations is insufficient for the detection of multidecadal trends in heat flux. Its uncertainty is much larger than the level expected of (0.5 Wm^{-2}). There is a need in agencies for imposing an accuracy standard that is better than 10 W/m^2 , which is a modest research quality, considering the incoming signal varying less than a tenfold above (100 W/m^2) (Godfrey 2006). However, this exigence forces the data producers to adopt conservative sampling. In Figure 4, the omission of large coastal areas in the evaluation of SST trends is an example of this accuracy conservativeness due to low instruments' resolution.

Data Treatment

The way in which the data is arranged by its producer for the users influences the product. For example, the blending of two distinct datasets following a satellite mission shift accounts for the different bias between them (Hammond et al. 2018). This process sweeps away precious information from the often already low-sampled dataset. Likewise, in K_d 's original database OC-CCI, a large portion of non clear sky measurements is removed for quality purpose (Sathyendranath et al. 2019). Because bright coastal water is sometimes misclassified as clouds, they adopted a clear-sky conservative screening strategy, which, in doubtful cases, rejects the sample when suspected under non-clear sky conditions. This strategy avoids some uncertainties but deprives the product from context favoring a strong turbidity in the water. This may be an additional bias contributing to the general turbidity of the oceans' underestimation.

Datasets happen to be approximated by averaged values and assumptions are made to simplify calculations. For instance, optical properties of the water column in OC-CCI's K_d product was a simple average of the top 10 m, taken as representative for the surface layer (Sathyendranath et al. 2019). As was pointed out, the more esoteric the parametrization of the product, the smaller the community able to recognize what the product represents. It can be recalled also that the analysis is of a mono-wavelength (490 nm). Future work would benefit from a full spectrum varying K_d along the depth representing a more realistic RHR. Such a dataset does not yet exist for public users.

Data Parametrization

The parametrization of essential climatic variables such as SST, DSST, K_d and LH is still considered premature for their reasonable insertion into OAGCMs. Raschke et al. (2012) discouraged inter-annual trend monitoring for surface radiation budget application. Others also pointed at the information's poor quality coming from observational platform, which is still insufficient to faithfully reproduce the air-sea interactions. The characterization of near surface layer processes such as the solar radiation extinction still has too many flaws in ancillary data (Bogdanoff et al. 2017).

Mixed layer modeling requires assimilation of multi-satellite data. To examine the climatic variables' evolution for their implication on air-sea interaction phenomenon (Gentemann and Hilburn 2015); (Babanin et al. 2012); (Kim et al. 2018); (Kim and Gnanadesikan 2018), remote sensing techniques must be enhanced to reproduce feedback effects (Soloviev 2013).

Once K_d product is improved, the analysis should then give extra weight to coastal water regions, where their impact is as high as are their uncertainty. Open and coastal oceans should be assessed separately like Levitus et al. (2005), and the comparison of the « large and positive 10.4% coastal trend » with the rest would allow to obtain more robust results. Like described by Sathyendranath et al. (2019), the method for K_d product creation relies on the consultation of its user's community. They establish a series of criteria based on users' requirements to rank available

algorithms for processing Kd. Hence, if the community expresses the urge for a better coastal Kd refinement, producers will adjust their algorithms accordingly.

Methodology

For the trend detection, the Seasonal Mann-Kendall test was selected. However, it is recognized that the original Mann-Kendall test should apply on data that are independent and identical distribution, which is not the case in this study. It is argued in literature whether to perform the analysis by separating months (Jin and Weller 2008) or apply the Seasonal modification (Sathyendranath et al. 2019), which was proposed to relax the restrictive requirement of the conventional Mann Kendall, and account for the serial dependence in the data. In any case, there are benefits to recognize the seasonality in the trends.

As mentioned in the discussion, the methodology surrounding the correlations in Table 6 is agreed to be insufficient for direct use. This type of correlation is applicable for linear dependency, while the dataset in the study is non-linear. Spearman's correlation test, which assesses monotonic relationship between variables, could have been more suitable here. But most importantly, nowhere in the process was mentioned the P-value of the correlation, on which it must be relied upon to interpret adequately the relationship. Instead, the quality of the relationship in the discussion was made regarding intercomparisons with similar literature. Finally, any "good" correlation is not a guarantee of causation. However, that last argument was the precept of the DSST intermediate relationship.

The assumption regarding water properties were liberal. The density ρ ($\sim 1025 \text{ kg m}^{-3}$) and the thermal capacity of water C_p ($\sim 4.17 \text{ kJ(K)}^{-1}\text{kg}^{-1}$) were fixed at these constant values. However, they vary greatly in function of depth, salinity, and location. This variation has the potential to affect the result significantly. It would be important to consider their fluctuation as well in a further study. The community debates around the dominance of the three-dimensional movement regarding the horizontal and vertical heat distribution. Although discussed, this analysis omits to consider the short term (10 year cycles) nature of important oscillations into its calculation.

Mitigations and Applications

Bond et al. (2013) insisted on the reduction of BC emissions. With their strong visible light absorption of at least $5 \text{ m}^2\text{g}^{-1}$ at 550 nm, this strategy represents a potential mitigation that could reduce the forcing in the short term and slow the global warming rate.

For inland and coastal zone managers, the enrichment of natural systems from land use and increased river agricultural and industrial runoff input²⁹ represent a severe environmental problem, including for example the eutrophication³⁰ problem (Morel and Antoine 1994). To improve its management, Sathyendranath (2000) suggested increasing remote sensing monitoring of chlorophyll levels on a regular basis, while Morel and Antoine (1994) developed an improvement to the Jerlov's Water Types model. Groom et al. (2019) highlight the need of funds for K_d from space agencies. Bukata et al. (1995) gives a technique based upon a chemical ratio to distinguish autochthone (water origin) from Allochthone (outside origin) DOM (Dissolved Organic Matter). This could lead to a refined analysis of color sources and its adequate mitigation.

Reach back an equilibrium through cold water flow.

The mixing of water masses taking place in strategic locations could drive an equivalent negative forcing on the climate. The pre-industrialization equilibrium that has been perturbed with various *forcings*, could be re-established. This research was motivated by the question "Does the forcing of pollution on air-sea interface compares to other drivers of the global warming?" The answer opens venues for arguable mitigations of the climate change, distinct from GHG management: A continuous cold-water flow assured with wave-activated pumps potentially reverses the upper layers' stratification documented throughout the whole study, removing its alarming warming effect. The quantities at stake should be estimated in Joules and square meters and be consistent with OHC estimates.

²⁹“Sediment fluxes: Globally, rivers deliver around 20 billion tons of suspended solids to the sea every year.” (Simionato et al., 2003)

³⁰“Eutrophication generally results in increases in algal biomass, to a point where harmful algal blooms result. [...] Chlorophyll-a is a standard indicator for eutrophication.” (Sathyendranath, 2000)

CHAPTER 6 Conclusions

It can be concluded that human activity colours the oceans' surfaces. This added colouration retains the sun's visible radiation closer to the surface. This increased upper layer heating rate contributes to the Earth's surface warming. This research aimed to solidify the documentation classifying K_d and SST as essential climate variable, like was recognised recently by the Global Climate Observing System (Sathyendranath et al. 2019). It contributed to the future improvement of the four main fluxes composing the Earth's heat budget, in the hope of solving the global warming problem. Based on a quantitative and quantitative analysis of global mapped K_d and SST trend, it can be concluded that those two climate variables are relatively linked, with a global trend correlation coefficient of 0.38. The results of mapped K_d trend also indicate that the global attenuation coefficient has increased by about 1% of the initial value of 0.062 m^{-1} . The increase occurred mainly on coastal and polar regions. The global increases of tributary pollutions and black carbon inputs are suspected anthropogenic origins. It was finally estimated that the difference between the 18-year K_d studied could be responsible for an approximated 0.33 W m^{-2} forcing on air-sea fluxes.

While the poor correlations seen in Table 6 limit the connections that can be made between the 5 variables (SST, DSST, K_d , Z_{crit} and F), this approach still indicates that the regional analysis of those connections above 0.29 are relevant. That is the case for the following pairs of variables: Z and SST, Z and K_d and K_d and SST. The first negative connection of -0.42 translates to an upward shift of SST whenever depth z becomes smaller. This new insight on the role of Z_{crit} can lead to a better understanding of the changing radiant heating rates of the upper layers of the oceans and help improve the fluxes in models. The research clearly indicated the role of K_d on the forcing, but has also raised some paths of solution against it.

The management of SW attenuation should be given more importance for future work. Such sublayer must be understood and predicted to be responsibly acted upon. The interest in the global ocean remote sensing and inclusion in models of a better refined K_d sublayers is growing and goes through a quiet revolution (Sathyendranath 2000). More investment into remote sensing programs and quality control is recommended. To address the bias and uncertainties of this study's

inputs, future studies could address the limits by selecting the Pathfinder L4 SST climate data records for SST inputs and perform a homemade parametrization of K_d based on more precise requirements. Finally, the assessment of the inclusion of K_d sublayer into OAGCM is essential to weigh its impact on the fluxes because of the many feedbacks between them. The use of the meteorological intermediate complexity UVIC Earth System Climate model software in Linux environment is the next methodology recommendation. The weighted forcing value is likely to appear smaller in this context. From now on, the consideration of K_d as a driver for the forcing retrieval is uttered, just as other sublayers drivers (DW, wave height, winds, mixing, GHG). This will potentially help to solve the closure problem in reducing the gap between the theoretical and empirical imbalance.

Ideas for future work were explored in the last chapter under the limitations regarding the data sampling, parametrization, and their treatment. Researchers should prepare to choose datasets with better continuity, which also target coastal regions' in-depth full spectrum composition. A future study should consider including the longwave fluxes into the analysis. An awareness should be given on natural and anthropogenic processes involved in the changing attenuation in the poles and coastal regions. To conclude with a question, if mankind were able to involuntary change the climate, would it be able to retrieve back the lost equilibrium, now with a conscious will?

References

- Abraham, J. P., Baringer, M., Bindoff, N. L., Boyer, T., Cheng, L. J., Church, J. A., ... & Willis, J. K. (2013). A review of global ocean temperature observations: Implications for ocean heat content estimates and climate change. *Reviews of Geophysics*, 51(3), 450-483. <https://doi.org/10.1002/rog.20022>.
- Androulidakis, Y., Kourafalou, V., Halliwell, G., Le Hénaff, M., Kang, H., Mehari, M., & Atlas, R. (2016). Hurricane interaction with the upper ocean in the Amazon-Orinoco plume region. *Ocean Dynamics*, 66(12), 1559-1588.
- Antoine, D., Morel, A., Gordon, H. R., Banzon, V. F., & Evans, R. H. (2005). Bridging ocean color observations of the 1980s and 2000s in search of long-term trends. *Journal of Geophysical Research: Oceans*, 110(C6).
- Australian Government Bureau of Meteorology (2020). ENSO Wrap-Up Current State of the Pacific and Indian Oceans. Retrieved March 3, 2020. <http://www.bom.gov.au/climate/enso/>.
- Babanin, A. V., Onorato, M., and Qiao, F. (2012), Surface waves and wave-coupled effects in lower atmosphere and upper ocean, *J. Geophys. Res.*, 117, C00J01, doi:10.1029/2012JC007932.
- Balaguru, K., Chang, P., Saravanan, R., & Jang, C. J. (2012). The barrier layer of the Atlantic warmpool: Formation mechanism and influence on the mean climate. *Tellus A: Dynamic Meteorology and Oceanography*, 64(1), 18162.
- Balmaseda, M. A., Hernandez, F., Storto, A., Palmer, M. D., Alves, O., Shi, L., ... & Gaillard, F. (2015). The ocean reanalyses intercomparison project (ORA-IP). *Journal of Operational Oceanography*, 8(sup1), s80-s97.
- Bergman, T. L., Incropera, F. P., DeWitt, D. P., & Lavine, A. S. (2011). *Fundamentals of heat and mass transfer*. John Wiley & Sons.
- Bernie, D. J., Guilyardi, E., Madec, G., Slingo, J. M., & Woolnough, S. J. (2007). Impact of resolving the diurnal cycle in an ocean-atmosphere GCM. Part 1: A diurnally forced OGCM. *Climate Dynamics*, 29(6), 575-590.
- Bogdanoff, A. S., Westphal, D. L., Campbell, J. R., Cummings, J. A., Hyer, E. J., Reid, J. S., & Clayson, C. A. (2015). Sensitivity of infrared sea surface temperature retrievals to the vertical distribution of airborne dust aerosol. *Remote Sensing of Environment*, 159, 1-13.
- Bogdanoff, A. S. (2017). *Physics of diurnal warm layers: Turbulence, internal waves, and lateral mixing* (Doctoral dissertation, Massachusetts Institute of Technology).
- Bond, T. C., Doherty, S. J., Fahey, D. W., Forster, P. M., Berntsen, T., DeAngelo, B. J., ... & Zender, C. S. (2013). Bounding the role of black carbon in the climate system: A scientific assessment. *Journal of geophysical research: Atmospheres*, 118(11), 5380-5552.
- Brunke, M. A., Wang, Z., Zeng, X., Bosilovich, M., & Shie, C. L. (2011). An assessment of the uncertainties in ocean surface turbulent fluxes in 11 reanalysis, satellite-derived, and combined global datasets. *Journal of Climate*, 24(21), 5469-5493.
- Buizza, R., Brönnimann, S., Haimberger, L., Laloyaux, P., Martin, M. J., Fuentes, M., ... & Ziese, M. (2018). The EU-FP7 ERA-CLIM2 project contribution to advancing science and production of earth system climate reanalyses. *Bulletin of the American Meteorological Society*, 99(5), 1003-1014. <https://doi.org/10.1175/BAMS-D-17-0199.1>.
- Bukata, R. P., Jerome, J. H., Kondratyev, A. S., & Pozdnyakov, D. V. (1995). *Optical properties and remote sensing of inland and coastal waters*. CRC press.

- Butler. (2019). The NOAA Annual greenhouse gas index (AGGI). 2019. <https://www.esrl.noaa.gov/gmd/aggi/aggi.html>.
- Chang, G. C., & Dickey, T. D. (2004). Coastal ocean optical influences on solar transmission and radiant heating rate. *Journal of Geophysical Research: Oceans*, 109(C1).
- Clayson, C. A., & Bogdanoff, A. S. (2013). The effect of diurnal sea surface temperature warming on climatological air–sea fluxes. *Journal of Climate*, 26(8), 2546-2556.
- Collins, W. D., Feldman, D. R., Kuo, C., & Nguyen, N. H. (2018). Large regional shortwave forcing by anthropogenic methane informed by Jovian observations. *Science advances*, 4(9), eaas9593.
- Dong, X., Zhu, Q., Fu, J. S., Huang, K., Tan, J., & Tipton, M. (2019). Evaluating recent updated black carbon emissions and revisiting the direct radiative forcing in Arctic. *Geophysical Research Letters*, 46(6), 3560-3570.
- Feldman. (2020). Level-3 Browser. NASA Earth Data Ocean Color. <https://oceancolor.gsfc.nasa.gov/13/>.
- Foken, T. (2006). 50 years of the Monin–Obukhov similarity theory. *Boundary-Layer Meteorology*, 119(3), 431-447.
- Foken, T. (2008). The energy balance closure problem: an overview. *Ecological Applications*, 18(6), 1351-1367. <https://doi.org/10.1890/06-0922.1>.
- Gentemann, C. L., Donlon, C. J., Stuart-Menteth, A., & Wentz, F. J. (2003). Diurnal signals in satellite sea surface temperature measurements. *Geophysical Research Letters*, 30(3).
- Gentemann, C. L., & Hilburn, K. A. (2015). In situ validation of sea surface temperatures from the GCOM-W 1 AMSR 2 RSS calibrated brightness temperatures. *Journal of Geophysical Research: Oceans*, 120(5), 3567-3585. <https://doi.org/10.1002/2014JC010574>.
- Gentemann, C. L., Minnett, P. J., Le Borgne, P., & Merchant, C. J. (2008). Multi-satellite measurements of large diurnal warming events. *Geophysical Research Letters*, 35(22). <https://doi.org/10.1029/2008GL035730>.
- Gilbert, R. O. (1987). *Statistical Methods for Environmental Pollution Monitoring*. John Wiley & Sons.
- Global Ocean Heat and Salt Content. (2019). NOAA National Centers for Environmental Information. Retrieved July 19, 2019. https://www.nodc.noaa.gov/OC5/3M_HEAT_CONTENT/.
- Godfrey, J. S. (2006). On Reconciling Oceanic and Atmospheric Estimates of Surface Heat Fluxes—and on Validating Greenhouse Models. In *Physical Oceanography* (pp. 67-78). Springer, New York, NY.
- Groom, S., Sathyendranath, S., Ban, Y., Bernard, S., Brewin, R., Brotas, V., ... & Wang, M. (2019). Satellite ocean colour: current status and future perspective. *Frontiers in Marine Science*, 6, 485. <https://doi.org/10.3389/fmars.2019.00485>.
- Hammond, M. L., Beaulieu, C., Henson, S. A., & Sahu, S. K. (2018). Assessing the presence of discontinuities in the ocean color satellite record and their effects on chlorophyll trends and their uncertainties. *Geophysical Research Letters*, 45(15), 7654-7662.
- He, X., Pan, D., Bai, Y., Wang, T., Chen, C. T. A., Zhu, Q., ... & Gong, F. (2017). Recent changes of global ocean transparency observed by SeaWiFS. *Continental Shelf Research*, 143, 159-166.
- Jerlov, N. G. (1976). *Marine optics*. Elsevier.
- Jin, X., & Weller, R. A. (2008). Multidecade global flux datasets from the objectively analyzed air-sea fluxes (oafux) project: Latent and sensible heat fluxes, ocean evaporation, and

- related surface meteorological variables lisan yu. OAFlux Project Tech. Rep. OA-2008-01. 그림, 74.
- Josey, S. A., Kent, E. C., & Taylor, P. K. (1999). New insights into the ocean heat budget closure problem from analysis of the SOC air-sea flux climatology. *Journal of Climate*, 12(9), 2856-2880.
- Josey, S. A., & Smith, S. R. (2006). Guidelines for evaluation of air-sea heat, freshwater and momentum flux datasets. CLIVAR Global Synthesis and Observations Panel (GSOP) Report, 12.
- Kawai, Y., & Wada, A. (2007). Diurnal sea surface temperature variation and its impact on the atmosphere and ocean: A review. *Journal of oceanography*, 63(5), 721-744.
- Kiehl, J. T., & Trenberth, K. E. (1997). Earth's annual global mean energy budget. *Bulletin of the American Meteorological Society*, 78(2), 197-208.
- Kim, G. E., Gnanadesikan, A., & Pradal, M. A. (2016). Increased surface ocean heating by colored detrital matter (CDM) linked to greater northern hemisphere ice formation in the GFDL CM2Mc ESM. *Journal of Climate*, 29(24), 9063-9076.
- Kim, G. E., Gnanadesikan, A., Del Castillo, C. E., & Pradal, M. A. (2018). Upper ocean cooling in a coupled climate model due to light attenuation by yellowing materials. *Geophysical research letters*, 45(12), 6134-6140.
- Kim, H. C., Nadiga, S., Son, S., Mehra, A., Garraffo, Z., Bayler, E., & Behringer, D. (2018). Implications of ocean color in the upper water thermal structure at NINO3.4 region: a sensitivity study for optical algorithms and ocean color variabilities. *GIScience & Remote Sensing*, 55(4), 568-582.
- Kueh, M. T., & Lin, P. L. (2015). Upper ocean response and feedback to spring weather over the Kuroshio in the East China Sea: A coupled atmosphere-ocean model study. *Journal of Geophysical Research: Atmospheres*, 120(19), 10-091. <https://doi.org/10.1002/2015JD023386>.
- L'Ecuyer et al. (2015)a. CLIVAR Consistency between Planetary Energy Balance and Ocean Heat Storage (CONCEPT-HEAT). *World Climate Research Program*.
- L'Ecuyer, T. S., Beaudoin, H. K., Rodell, M., Olson, W., Lin, B., Kato, S., ... & Hilburn, K. (2015). The observed state of the energy budget in the early twenty-first century. *Journal of Climate*, 28(21), 8319-8346.
- Lee, Z. P., Darecki, M., Carder, K. L., Davis, C. O., Stramski, D., & Rhea, W. J. (2005). Diffuse attenuation coefficient of downwelling irradiance: An evaluation of remote sensing methods. *Journal of Geophysical Research: Oceans*, 110(C2).
- Levitus, S., Antonov, J., & Boyer, T. (2005). Warming of the world ocean, 1955–2003. *Geophysical research letters*, 32(2).
- Loeb, N. G., Wielicki, B. A., Doelling, D. R., Smith, G. L., Keyes, D. F., Kato, S., ... & Wong, T. (2009). Toward optimal closure of the Earth's top-of-atmosphere radiation budget. *Journal of Climate*, 22(3), 748-766.
- Mallick, S. K., Agarwal, N., Sharma, R., Prasad, K. V. S. R., & Weller, R. A. (2019). Impact of satellite-derived diffuse attenuation coefficient on upper ocean simulation using high-resolution numerical ocean model: case study for the Bay of Bengal. *Marine Geodesy*, 42(6), 535-557.
- Masson-Delmotte, V., Zhai, P., Pörtner, H. O., Roberts, D., Skea, J., Shukla, P. R., ... & Waterfield, T. (2018). Global warming of 1.5 C. An IPCC Special Report on the impacts of global warming of, 1, 1-9.

- Mellor, G., & Blumberg, A. (2004). Wave breaking and ocean surface layer thermal response. *Journal of physical oceanography*, 34(3), 693-698.
- Meucci, A., Young, I. R., Hemer, M., Kirezci, E., & Ranasinghe, R. (2020). Projected 21st century changes in extreme wind-wave events. *Science Advances*, 6(24), eaaz7295. <https://doi.org/10.1126/sciadv.aaz7295>.
- Mobley, C. D. (1994). *Light and Water: Radiative Transfer in Natural Waters*. Academic Press.
- Morel, A., & Antoine, D. (1994). Heating rate within the upper ocean in relation to its bio-optical state. *Journal of Physical Oceanography*, 24(7), 1652-1665.
- Morim, J., Hemer, M., Wang, X. L., Cartwright, N., Trenham, C., Semedo, A., ... & Andutta, F. (2019). Robustness and uncertainties in global multivariate wind-wave climate projections. *Nature Climate Change*, 9(9), 711-718. <https://doi.org/10.1038/s41558-019-0542-5>.
- Ocean Optic Web Book. Consulted on March 2018
http://www.oceanopticsbook.info/view/absorption/absorption_by_oceanic_constituents.
- Ohlmann, J. C., Siegel, D. A., & Mobley, C. D. (2000). Ocean radiant heating. Part I: Optical influences. *Journal of Physical Oceanography*, 30(8), 1833-1848.
- Ohmura, A. (2014). The development and the present status of energy balance climatology. *Journal of the Meteorological Society of Japan*. Ser. II, 92(4), 245-285.
- Palmer, M. D. (2014). Variations of Oceanic Heat Content. *Global Environmental Change*, 77-83. Springer.
- Palmer, M. D., Good, S. A., Haines, K., Rayner, N. A., & Stott, P. A. (2009). A new perspective on warming of the global oceans. *Geophysical Research Letters*, 36(20). <https://doi.org/10.1029/2009GL039491>.
- Pierce, D. W., Barnett, T. P., AchutaRao, K. M., Gleckler, P. J., Gregory, J. M., & Washington, W. M. (2006). Anthropogenic warming of the oceans: Observations and model results. *Journal of Climate*, 19(10), 1873-1900.
- Rapizo, H., Babanin, A. V., Schulz, E., Hemer, M. A., & Durrant, T. H. (2015). Observation of wind-waves from a moored buoy in the Southern Ocean. *Ocean Dynamics*, 65(9), 1275-1288.
- Raschke, E., Kinne, S., Stackhouse, P. W., & RFA, G. R. F. A. (2012). GEWEX Radiative Flux Assessment (RFA), Volume 1: Assessment, a Project of the World Climate Research Programme Global Energy and Water Cycle Experiment (GEWEX) Radiation Panel." *World Climate Research Program Report*.
- Reynolds, R. W., & Smith, T. M. (1994). Improved global sea surface temperature analyses using optimum interpolation. *Journal of climate*, 7(6), 929-948.
- Reynolds, R. W., Smith, T. M., Liu, C., Chelton, D. B., Casey, K. S., & Schlax, M. G. (2007). Daily high-resolution-blended analyses for sea surface temperature. *Journal of climate*, 20(22), 5473-5496. Reynolds and Smith. 1998. "A High-Resolution Global Sea Surface Temperature Climatology for the 1961-90 Base Period." *Journal of Climate* 11.12 (1998): 3320-3323.
- Sathyendranath, S., Brewin, R. J., Jackson, T., Mélin, F., & Platt, T. (2017). Ocean-colour products for climate-change studies: What are their ideal characteristics?. *Remote Sensing of Environment*, 203, 125-138.
- Sathyendranath, S., Brewin, R. J., Brockmann, C., Brotas, V., Calton, B., Chuprin, A., ... & Platt, T. (2019). An ocean-colour time series for use in climate studies: the experience of the ocean-colour climate change initiative (OC-CCI). *Sensors*, 19(19), 4285.

- Sathyendranath, S. (2000). Remote sensing of ocean colour in coastal, and other optically-complex, waters.
- Schiller, A., & Godfrey, J. S. (2005). A diagnostic model of the diurnal cycle of sea surface temperature for use in coupled ocean-atmosphere models. *Journal of Geophysical Research: Oceans*, 110(C11). <https://doi.org/10.1029/2005JC002975>.
- Shell, K. M., Frouin, R., Nakamoto, S., & Somerville, R. C. J. (2003). Atmospheric response to solar radiation absorbed by phytoplankton. *Journal of Geophysical Research: Atmospheres*, 108(D15).
- Siedler, G., S. M. Griffies, J. Gould, and J. A. Church. 2013. *Ocean Circulation and Climate: A 21st Century Perspective*. Vol. 103. Academic Press.
- Simionato et al. (2003). Chapter 4. International Association of the Physical Sciences of the Oceans. *Final Report of the IUGG Working Group Geosciences: The Future*. <http://citeseerx.ist.psu.edu/viewdoc/download?doi=10.1.1.453.3942&rep=rep1&type=pdf#page=29>.
- Soloviev, A. (2013). *The Near-Surface Layer of the Ocean: Structure, Dynamics and Applications*. Vol. 48. Springer Science & Business Media.
- Stocker et al. (2013). "IPCC, 2013: Climate Change 2013: The Physical Science Basis. Contribution of Working Group I to the Fifth Assessment Report of the Intergovernmental Panel on Climate Change." Cambridge University Press, Cambridge, United Kingdom and New York, NY, USA,. https://www.ipcc.ch/site/assets/uploads/2018/02/WG1AR5_all_final.pdf.
- Strong, A., Chisholm, S., Miller, C., & Cullen, J. (2009). Ocean fertilization: time to move on. *Nature*, 461(7262), 347-348. <https://doi.org/10.1038/461347a>.
- Trenberth, K. E., Fasullo, J. T., & Balmaseda, M. A. (2014). Earth's energy imbalance. *Journal of Climate*, 27(9), 3129-3144.
- U.S. Department of Commerce. (2019). NOAA Budget Estimates Fiscal Year 2019. available on public FTP server. ftp://ftp.library.noaa.gov/noaa_documents.lib/NOAA_budget/NOAA_blue-book/.
- Valdivieso, M., Haines, K., Balmaseda, M., Chang, Y. S., Drevillon, M., Ferry, N., ... & Peterson, K. A. (2017). An assessment of air-sea heat fluxes from ocean and coupled reanalyses. *Climate Dynamics*, 49(3), 983-1008.
- Webster, P. J., Clayson, C. A., & Curry, J. A. (1996). Clouds, radiation, and the diurnal cycle of sea surface temperature in the tropical western Pacific. *Journal of Climate*, 9(8), 1712-1730.
- Weih, R. R., & Bourassa, M. A. (2014). Modeled diurnally varying sea surface temperatures and their influence on surface heat fluxes. *Journal of Geophysical Research: Oceans*, 119(7), 4101-4123. <https://doi.org/10.1002/2013JC009489>.
- Wild, M. (2017). Towards global estimates of the surface energy budget. *Current Climate Change Reports*, 3(1), 87-97.
- Wild, M., Folini, D., Schär, C., Loeb, N., Dutton, E. G., & König-Langlo, G. (2013). The global energy balance from a surface perspective. *Climate dynamics*, 40(11-12), 3107-3134.
- Wills, S. M. (2015). On the observed relationships between variability in sea surface temperatures and the atmospheric circulation in the Northern Hemisphere (Doctoral dissertation, Colorado State University).
- Young et al. (2011a). Supporting Online Material for Global Trends in Wind Speed and Wave Height.

- <http://science.sciencemag.org/content/sci/suppl/2011/03/22/science.1197219.DC1/Young.SOM.pdf>.
- Young, I. R., Zieger, S., & Babanin, A. V. (2011). Global trends in wind speed and wave height. *Science*, 332(6028), 451-455. <https://doi.org/10.1126/science.1197219>.
- Yu, L., & Weller, R. A. (2007). Objectively analyzed air–sea heat fluxes for the global ice-free oceans (1981–2005). *Bulletin of the American Meteorological Society*, 88(4), 527-540.
- Yu, L., Haines, K., Bourassa, M., Cronin, M., Gulev, S., Josey, S., ... & Roemmich, D. (2013). Workshop Report Towards achieving global closure of ocean heat and freshwater budgets: Recommendations for advancing research in air-sea fluxes through collaborative activities.
- Zhang, H., Beggs, H., Ignatov, A., & Babanin, A. V. (2020). Nighttime cool skin effect observed from Infrared SST Autonomous Radiometer (ISAR) and depth temperatures. *Journal of Atmospheric and Oceanic Technology*, 37(1), 33-46.
- Zhang, H., Babanin, A. V., Liu, Q., & Ignatov, A. (2019). Cool skin signals observed from Advanced Along-Track Scanning Radiometer (AATSR) and in situ SST measurements. *Remote Sensing of Environment*, 226, 38-50
- Zhang, H., Beggs, H., Majewski, L., Wang, X. H., & Kiss, A. (2016). Investigating sea surface temperature diurnal variation over the Tropical Warm Pool using MTSAT-1R data. *Remote Sensing of Environment*, 183, 1-12.